Title
High resolution anatomic spectroscopic and diffusion magnetic resonance imaging of the brain

Author
Xu, Duan

Publication Date
2005

Peer reviewed|Thesis/dissertation

High resolution anatomic, spectroscopic, and diffusion magnetic resonance imaging of the brain

by

Duan Xu

DISSERTATION

Submitted in partial satisfaction of the requirements for the degree of

DOCTOR OF PHILOSOPHY

in

Bioengineering

in the

GRADUATE DIVISIONS

of the

UNIVERSITY OF CALIFORNIA SAN FRANCISCO

and

UNIVERSITY OF CALIFORNIA BERKELEY

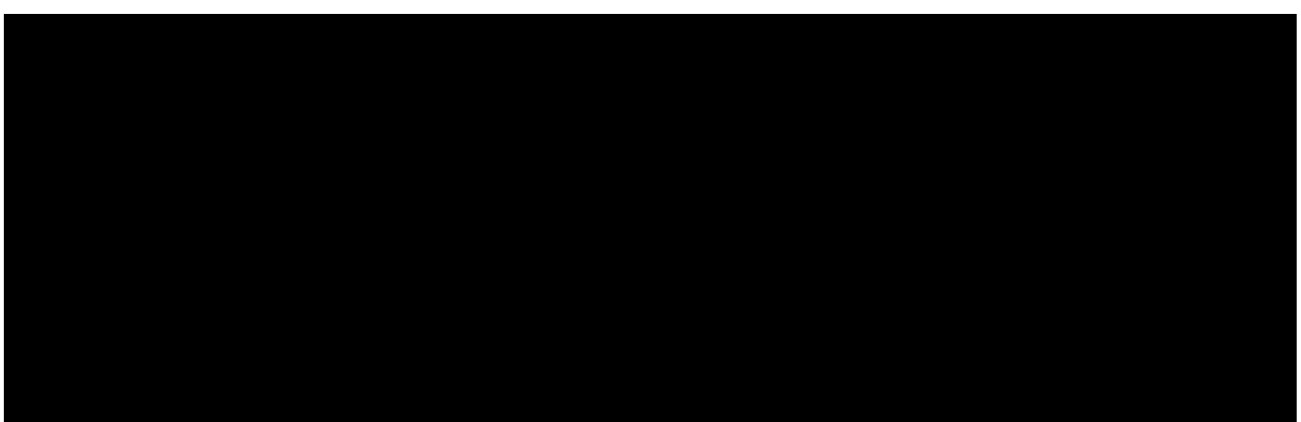

Date

University Librarian

Degree Conferred: .....

This work is dedicated to my parents and brother
for their continuing support and love.

Acknowledgements

I would like to thank various people for the support and encouragement that I have received in the past several years. My graduate work would not have been this smooth and enjoyable without their inputs.

First of all, I have to thank my thesis advisor, Dr. Daniel Vigneron, who has continued to guide and support my research and development of my career. In the beginning, with only a few postdoctoral fellows and graduate students, Dr. Vigneron took a tremendous amount of time to help me start and formulate a research plan that has provided me with the best possible training in magnetic resonance imaging. This training included a wide range of topics from understanding basic principles to building hardware and software that directly controlling the acquisition of the MR images. Without his guidance, I cannot imagine overcoming all the difficulties that have faced me in my graduate work.

Next I would like to thank several other faculty members who also provided me with advice and made my graduate study very enjoyable. Thanks to Dr. Sharmila Majumdar for academic guidance in choosing coursework. Thanks to Dr. Sarah Nelson for allowing me participate in the development of our graduate group and encouraging the student organized seminar series. Thanks to Dr. John Kurhanewicz for chairing my qualifying committee and providing feedback on the progress of sequence developments. Last but not least, I am grateful for the continued guidance in neuroradiology from Dr. A James Barkovich and Dr. Pratik Mukherjee.

I also would like to thank my fellow students and colleagues, Chuck, Tim, Julio, Joe, Xiaojuan, Mike, Annette, Joonmi, Jeff, Janine, Esin, and many others, who have provided constant company and often heated debates in research and life topics. I would especially like to thank Albert Chen and Eric Han for enduring the endless hours of scanning, debugging new code, and never ending upgrades. It's always better when there is someone else there when the building is pretty much empty and the sun has gone down hours ago. I also would like to thank our technologist, Niles Bruce, who has always been there for the enormous amounts of data collection.

Abstract

MRI has increasingly becoming essential in radiological diagnosis due to its robustness in yielding a variety of contrasts inferring different anatomy and functions of the organs. MR techniques have improved dramatically due to advances in electronic components, and computing power and methods. The continuing goal in MR has been and will still be to improve signal-to-noise (SNR) and to reduce imaging time and image artifacts. As a method that has an almost infinite combination of acquisition parameters and techniques that offer a balance of contrast, SNR, time, and artifacts, it is important to study and analyze them to yield the best diagnostics for treatment planning.

In this dissertation work, the goal was to achieve higher quality (spatial and spectral resolution, less distortion, faster imaging times) MR images through improvements in hardware and software, specifically in terms of RF coil and scanner sequence development. The RF coils development focused on the building and usage of phased array coils while the sequence development was to improve and minimize distortions in the diffusion imaging. Another component of this thesis has been the investigation of high resolution MR spectroscopic imaging using phased arrays and clinical applications in neonates. It is important not only to develop these tools but to utilize them as soon as they became available. Each of the technical descriptions is followed by feasibility studies on phantoms and volunteers as proof of concept. Then, the techniques are applied to patient studies to, not only demonstrate proof-of-concept, but also to investigate the potential research and clinical value provided by these advancements. The various methods researched in this dissertation offer a wide range of analyses in order to provide

an accurate snapshot of the patient condition. This translational research can be quickly applied to patient management to improve diagnosis and treatment planning as demonstrated by the initial patient studies.

Dissertation Committee Chair

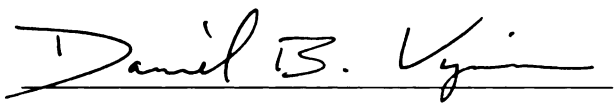

Dr. Daniel B. Vigneron

Table of Contents

List of Tables

List of Figures

1 Goal

Magnetic Resonance Imaging (MRI) is a noninvasive imaging technique for in vivo diagnoses of human diseases for the past several decades. With principles developed in the late 1940's [1, 2] and experiments performed in the following decades [3-5], MRI has increasingly becoming essential in radiological diagnosis due to its robustness in yielding a variety of contrasts inferring different anatomy and functions of the organs.

Magnetic resonance imaging techniques have improved dramatically due to advances in electronic components, and computing power and methods. The continuing goal in MR has been and will still be to improve signal-to-noise (SNR) and to reduce imaging time and image artifacts. As a method that has an almost infinite combination of acquisition parameters and techniques that offer a balance of contrast, SNR, time, and artifacts, it is important to study and analyze them to yield the best diagnostics for treatment planning.

The most fundamental improvement that can be made is with the hardware specifically receive coils, because many of the electronics component cannot be modified modularly. The geometry and interactions between the coils and the subject will dictate the most dominate factor in imaging—SNR. As long as the image has ample SNR, accurate assessments of the imaged object can be done. With the advances in analog to digital converter (ADC) together with faster and more powerful computers, the scanners are able to receive multiple channels of data and process them. The utilization of multiple coils are increasing becoming important in improving SNR due to the simple fact that noise is random and the signal is not; therefore, the signal will improve with additional coils and

the noise will not. In this work, the exploration of combining high SNR phased array coils with various advanced imaging techniques offered unprecedented high resolution studies of the adult and neonatal brain.

The other significant factor in MR imaging is the artifacts that are produced. Artifacts can arise from a variety of factors such as motion, k-space trajectory, magnetic susceptibility and etc. Many of these artifacts dominate in different types of acquisition, thus making the correct choice for the imaging sequence is essential in providing the best diagnosis. Changes in pulse sequences (scanner acquisition software) will affect the manifestation of the artifacts, and offer advantages and disadvantages. Another goal of this thesis project was to implement and evaluate pulse sequences to improve MR diffusion studies by reducing artifacts.

Lastly, with increasing complexity and amount of data, data analysis is often a bottle-neck in understanding and providing the correct treatment planning for patients. Automated processing techniques are critical in offering high throughput data analysis. This allows consistent and time efficient analysis of the data. The data collected in MR spectroscopy scans are difficult to analysis due to the fact that over 1000 spectra are generated per scan and multiple metabolite information coexist in each spectrum. Previously, techniques have been introduced to quantify the amount of the metabolites [6]. In this work, the analysis was extended to utilize the quantified metabolite information based on the regions of interest (ROI) in an automated manner.

In this thesis work, the goal was to achieve higher quality (spatial and spectral resolution, less distortion, faster imaging times) MR images through improvements in hardware and software, specifically in terms of RF coil and scanner sequence development. The RF coils development focused on the building and usage of phased array coils while the sequence development was to improve and minimize distortions in the diffusion imaging. Another component of this thesis has been the investigation of high resolution MR spectroscopic imaging using phased arrays and clinical applications in neonates. It is important not only to develop these tools but to utilize them as soon as they became available. In this dissertation, each of the technical descriptions is followed by feasibility studies on phantoms and volunteers as proof of concept. Then, the techniques are applied to patient studies to, not only demonstrate proof-of-concept, but also to investigate the potential research and clinical value provided by these advancements. The various methods researched in this dissertation offer a wide range of analyses in order to provide an accurate snapshot of the patient condition. This translational research can be quickly applied to patient management to improve diagnosis and treatment planning as demonstrated by the initial patient studies.

2 Magnetic Resonance Principles

In this chapter, the basic physical principles of magnetic resonance imaging are briefly described. Concepts of nuclear spin, perturbations in the field to generate signal, various techniques to generate contrast, and signal-to-noise (SNR) are introduced to create the foundation for the discussion of more advanced research topic in this dissertation.

2.1 Nuclear Spin

MRI uses the properties of the atom in its chemical and magnetic environment to offer information of the increasingly larger components such as molecules, tissues, and organs. The nuclear species with multiple of ½ nuclear spin, which means nuclei with unpaired protons, can be imaged when placed in a larger static magnetic field B. These nuclei have a net spin and mostly aligned in the direction of the magnetic field. The nuclei precession frequency is given by $\omega=\gamma B$.

Nuclei	Net Spin	γ (MHz/T)	Natural Abundance
^{1}H	1/2	42.58	99.985
^{13}C	1/2	10.71	1.10
^{19}F	1/2	40.08	100
^{23}Na	3/2	11.27	100
^{31}P	1/2	17.25	100

Table 2.1 Nuclei of interest in magnetic resonance imaging.

Most of the nuclear spins are aligned with the field in a lower energy states; in comparison, some of the spins exist naturally in the higher energy states, opposing the field. The separation of the energy states is quantized, given by the equation $E=h\omega$. For this exact reason, the excitation energy required for changing the spin system has to be an integral multiple of this constant. [7]

2.2 Image Contrast

Out of all the imaging modalities, the single largest advantage of magnetic resonance is the ability of providing various image contrast as a result of different imaging parameters. Two of the most frequently utilized parameters are time to echo (TE) and time of repetition (TR). These two parameters affect the image acquisition by allowing various amounts of the signal change that are measured.

The signal changes in MR after excitation or perturbation of the system are described by the Bloch Equation and affected by two time constants, T1 and T2, which are inherent to the tissue properties. $\frac{dM_{x,y}}{dt} = \frac{M_{x,y}}{T_2}$ describes the change in magnetization in the transverse plane, which can be directly measured by receive coils, and $\frac{dM_z}{dt} = \frac{(M_0 - M_z)}{T_1}$ describes the longitudinal magnetization, which measurement can be taken in carefully designed experiments. [8] T2 relaxation is also called spin-spin or transverse relaxation; it is the time for the coherent magnetization to decay to 37% of the initial magnetization after a 90° pulse as the energy of the system is exchanged through individual spin to spin interactions. T1 relaxation, or spin-lattice/longitudinal relaxation, is the time for the magnetization to grow to 63% of the total magnetization after the 90 pulse. In T1 interactions, the energy is exchanged from the spins to the surrounding lattice or other molecules. The decaying of magnetization in T2 and growth of magnetization in T1 are demonstrated in Figure 2.1.

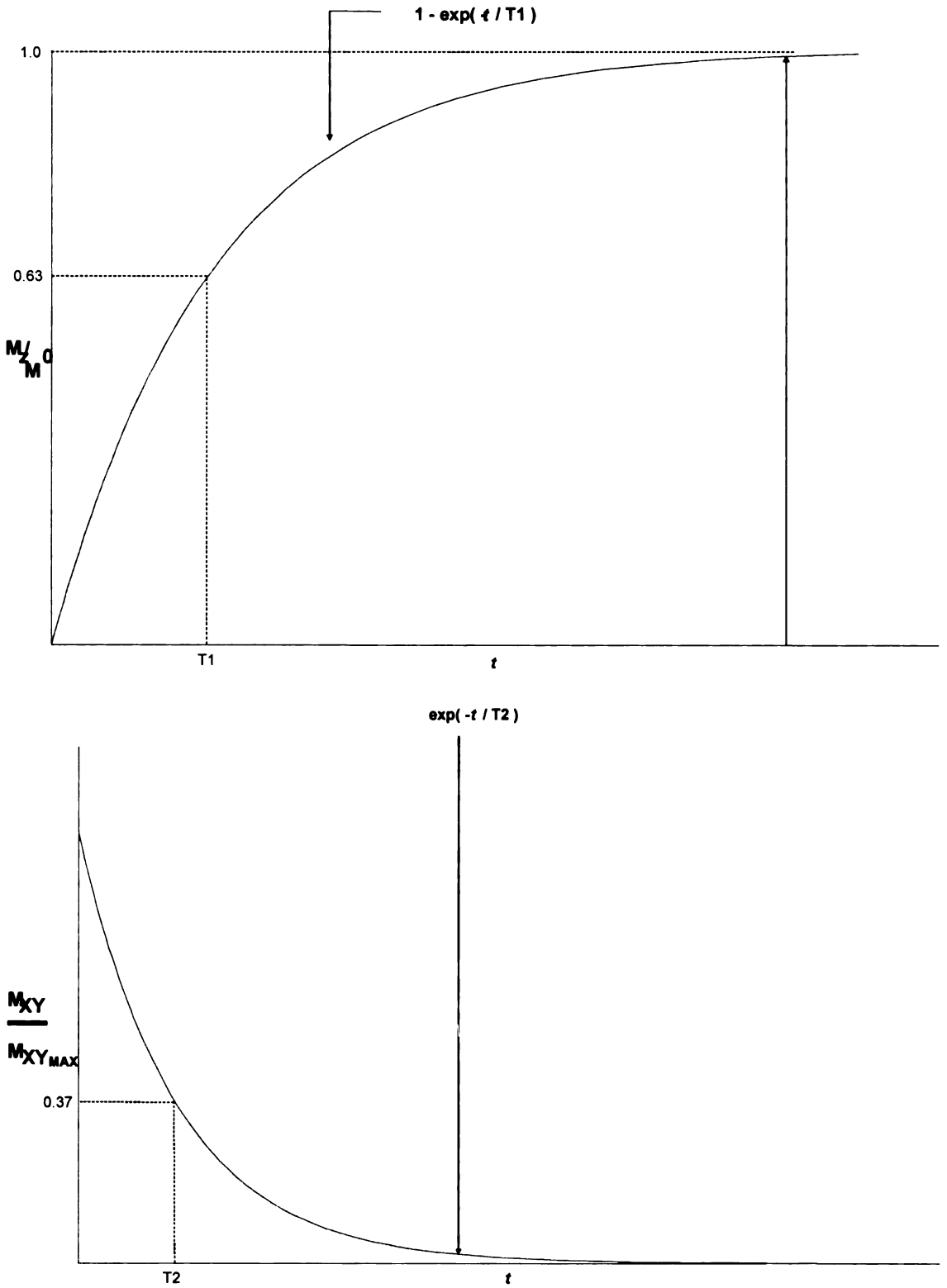

Figure 2.1. Magnetization recovery (T1) and decay (T2) curves.

The image contrast is also determined by the acquisition scheme, dependent on the echo placements in k-space. Since the center of k-space dominates the image intensity, the center echo will determine whether the image is T1 or T2 weighted. This property can be explained by the Fourier expansion series $f(x) = \frac{1}{2}a_0 + \sum_{n=1}^{\infty} a_n \cos(nx) + \sum_{n=1}^{\infty} b_n \sin(nx)$, in which the $\frac{1}{2}a_0$ term is the average intensity of the image. In most cases, the center of k-space gets filled first to provide the most SNR before the natural spin dephasing occurs. To demonstrate T1 and T2 weighting, please see the following images.

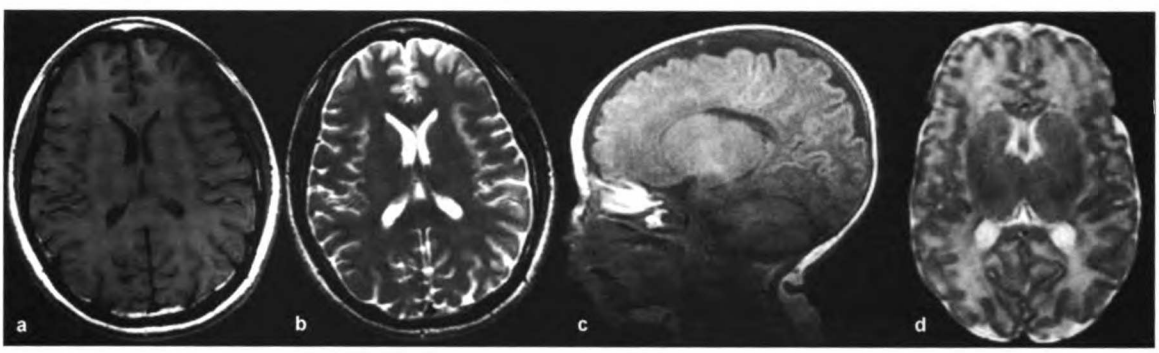

Figure 2.2. T1 and T2 comparison between adults and neonates.
T1 (a, c) and T2 (b, d) images of adult 29 years old (a, b) and neonate 40 weeks old (c, d) demonstrate the differences in image contrast with respect to age. The neonate brain is noticeable with less defined structures and sulcation patterns.

The differences in image intensities are the direct result of tissues having different T1 and T2 values. At TE, the separation between the T2 curves of the tissues determines the T2 contrast differences. Similarly, the T1 differences are obtained when TR is shorter than the time for complete longitudinal relaxation giving various saturation levels. A T1 weighted adult brain image would have dark ventricles, gray colored gray matter, and white colored white matter. A T2 weighted adult brain image would have bright ventricles and the gray and white matter contrast are reversed compared to the T1. In the

spin echo experiment described below, the image contrast can be adjusted using this simplified equation $s = \rho(1 - e^{\frac{TR}{T1}})e^{\frac{TE}{T2}}$ [9], in which ρ describes the proton density and the other 2 components are dictated by TR and TE; therefore, various contrasts can be generated to highlight the contributions from proton density, T1 or T2.

2.3 Signal to Noise

In MR, there is no resolution in the traditional sense where it is determine by the ability of the system to resolve two objects separated by some distance; the resolution is the image resolution, simply the field of view (FOV) divided by the image matrix size. Therefore, as long as there are enough SNR to analysis the structures, images will be acquired at that resolution. $SNR \propto \Delta x \Delta y \Delta z (\sqrt{total\ readout\ time}) K_{coil} f(\rho, T_1, T_2)$ [9]. As demonstrated in the equation, the signal will be dependent on the voxel size ($\Delta x \Delta y \Delta z$), the acquisition time, coil reception, and the read out signal strength depending on the pulse sequence. The trade-offs between the factors would yield different SNR values depending on the desired balance of resolution and time.

2.4 Spin Echo

Since the discovery of spin echo by Hahn in 1950s, it has played an important role in MRI. [2] It's critical in various imaging and spectroscopy methods because it allows for acquisition of the signal at much longer time after the initial excitation pulse. After the initial excitation pulse, the coherent magnetization dephases quickly due to imhomogeneities of the field. But by using the spin echo method, these field effects can be minimized or eliminated.

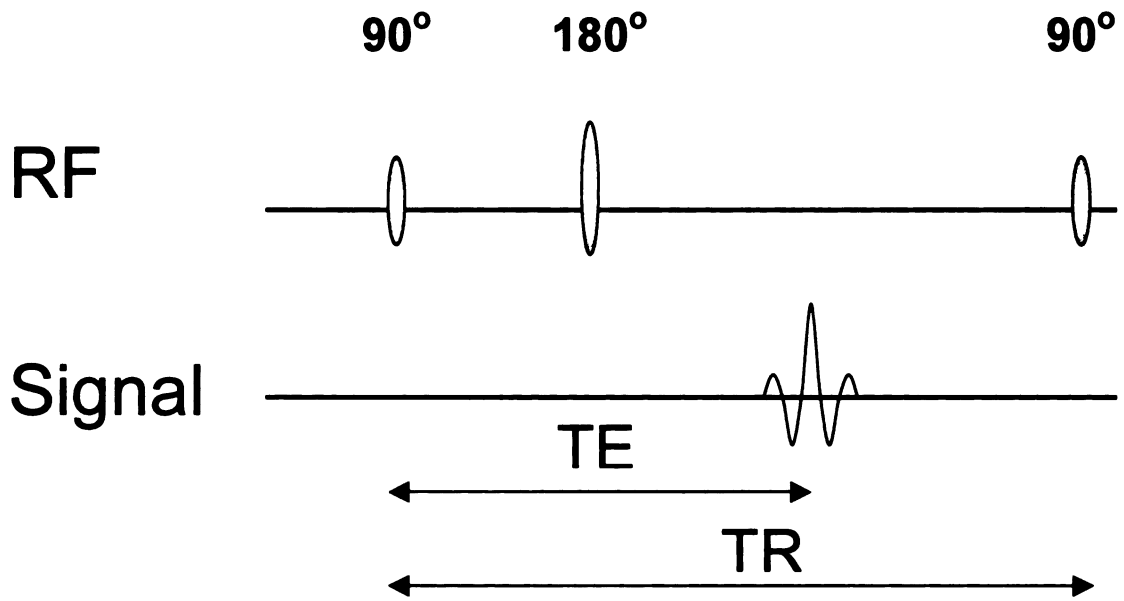

Figure 2.3. Spin Echo Pulse Diagram.
Spin echo schematic showing echo generation at TE after 90 and 180 RF pulse. TR is also demonstrated when the experiment repeats to fill k-space.

Following the 90° pulse, the net magnetization is flipped into the transverse plane, enabling the signal to be picked by the receive coils. Once in the transverse plane, the coherent magnetization will start to dephase due to the different magnetic and chemical environments of the spins. After some time τ or TE/2, an 180° RF pulse is applied in either the y or the x axis. TE stands for time to echo, as in this experiment, an echo is achieved at the same time τ or TE/2 after the application of the 180° pulse. See Figure 2.3 for visual demonstration of the spin movements. TR as expressed in Figure 2.3 is the time of repetition, which is time before the next excitation to fill the k-space lines for Fourier reconstruction of the object being imaged.

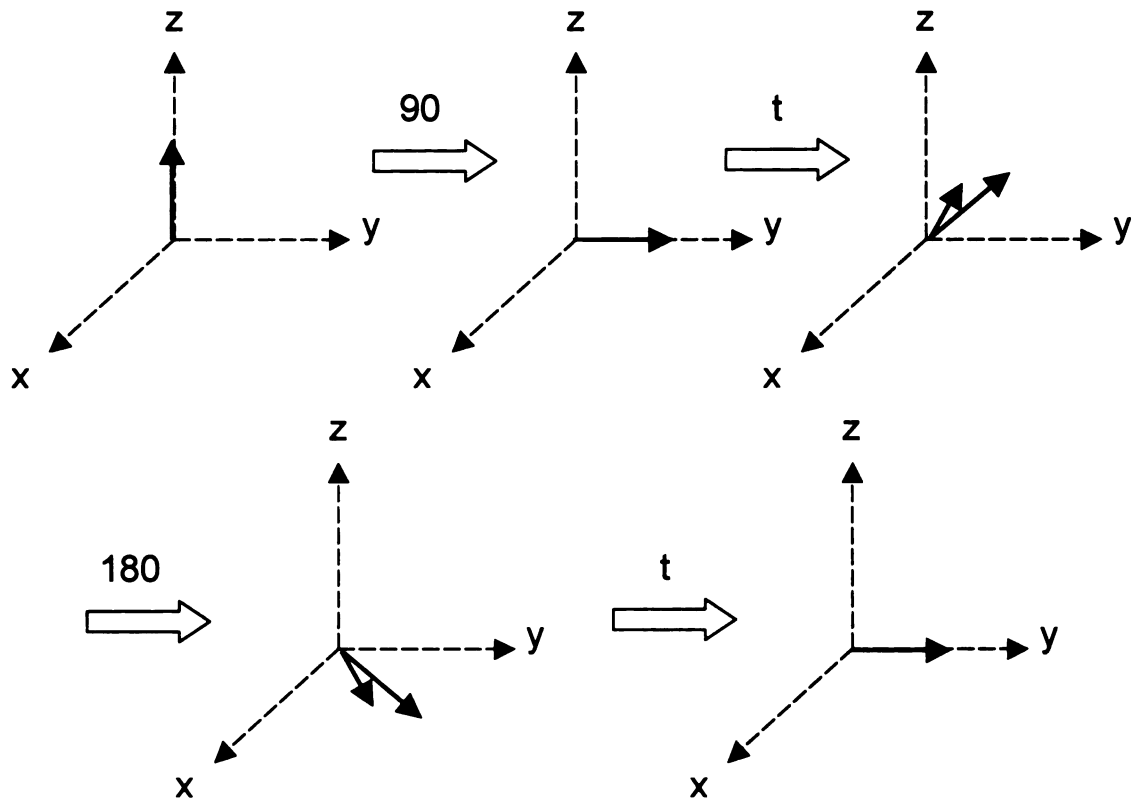

Figure 2.4. Magnetization changes for the spin echo experiment. Dephasing occurs after the 90 pulse has played at T2* where inhomogeneity in the system accelerates the process. After some t, a 180 pulse is played to rotate the spins around either y or z axis. An echo will form at another time t after the 180 pulse as the spins will experience the opposite effects of dephasing due to inhomogeneity and become coherent again. The echo acquired would be true T2 weighted.

The spin echo method allows for the refocusing of the spins with minimal affects from magnetic susceptibility and other inhomogeneous factors for the simple assumption that the spins will experience the exact opposite field effects after the 180° pulse. It is used in the diffusion preparation component and spectroscopy acquisitions, which will be discussed in this work.

3 RF Coil

Radio frequency (RF) coils are one of the most important aspects in MR imaging as they are responsible for receiving the desired signal. In this section, various types of coils are introduced, which will be referred to in the subsequent chapters as different imaging techniques would benefit differently from using specialized coils.

3.1 Background Theory

In magnetic resonance imaging, the acquisitions of images are generated from the perturbations of the magnetic field and measuring the response or the change. From simple electromagnetics, a current is only induced in a loop of wire (receive coil) when there is a change of magnetic field across the surface of that loop (flux), therefore, dictating that all receive coils in MR have to be perpendicular to that of the main field. This physical phenomenon restricts the placements of the coils and affects the acquired image properties.

Furthermore, the strength of the magnetic field experienced by the coil falls off as the square of the distance which can be described piece-wise by the Biot-Savart Law, $\vec{dB} = \frac{\mu_0 I \vec{dL} x \hat{\vec{r}}}{4\pi r^2}$, which describes the magnetic field experienced some distance away from a piece of straight wire. [10] This is commonly referred to as coil profile.

Due to the quantized property of MR excitations, all coils are tuned to the resonance frequency of the nuclear specie that is being measured. The coils are standard RLC

circuits with the frequency directly proportional to the inductance and the capacitance, $\varpi \propto \frac{1}{\sqrt{LC}}$.

3.2 Coil types

In MR imaging, the measured signal depends heavily on the type of the reception coil. SNR, coil profile, uniformity, and depth of penetration are generally the biggest concerns. The geometry and position relatively to the subject determine the best suited application of those coils. They will be briefly explained here as the main focus of this thesis work is to utilize the SNR gain of the specialized coils for research.

3.2.1 Surface Coil

In the early days of MR, localization using gradients was difficult to achieve. Using a simple loop of wire, signals are acquired from one small region, achieving the crudest form of localization. Even as the MR systems developed advanced electronics to allow accurate spatial localization through the use of gradients, surface coils remained a powerful tool to image small localized region with relatively high SNR close to the coil. However, the coil profile is visible on the resultant image, which requires intensity correction. At the same time, the depth of penetration of surface coils is poor as the intensity will drop as the square of the distance away from the coil. But in certain

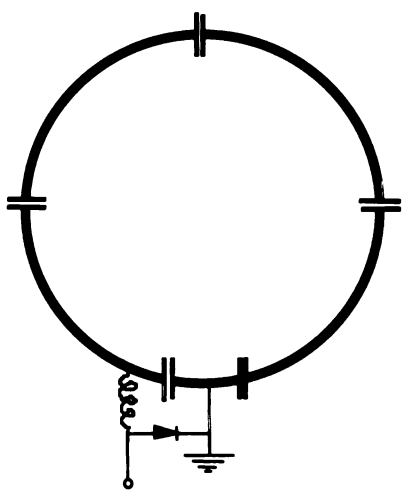

Figure 3.1. Schematic of a single loop surface coil.

imaging application such as imaging of cerebral cortex, several centimeters of penetration is more than enough.

Most of the surface coils are receive-only coils and the excitation is provided by the more homogeneous and larger body coil. Thus, the intensity variations are only result of the coil profile and not affected by non-uniform excitation. All of the receive only coils have a so-called "trap circuit" to detune the coil during excitation, so that the coil will not receive the energy and affect the signal during reception. The trap circuit, as demonstrated in the figure, is another RLC circuit with a diode, which during the excitation, a positive voltage received from the scanner will split the resonance frequency of the coil to much higher and lower frequencies that are completely outside of the frequencies that we are interested in.

3.2.2 Quadrature Head Coil

The most widely used coil in a standard clinical setting is the quadrature head coil, or the birdcage coil, for brain imaging. Birdcage coils consist of two circular end rings with rungs connecting them, which provide relatively uniform transmit and reception. [11] The uniformity in coil profile can be seen in the figure below, the simulation of an improved head coil. In quadrature detection, two sets of signals or modes are acquired simultaneously. When receiving, the signals from the separate coils are combined with a 90° phase offset. In other words, the summation of the signal is done by a time delay. This simple addition of signals yields a square root of 2 gain in SNR while reducing the transmit power by a factor 2 and only require one receiver channel, allowing faster and

simpler reconstruction. [12, 13] It's capability in uniform transmit limits the excitation RF to a small portion of the body, therefore, reducing the total power needed.

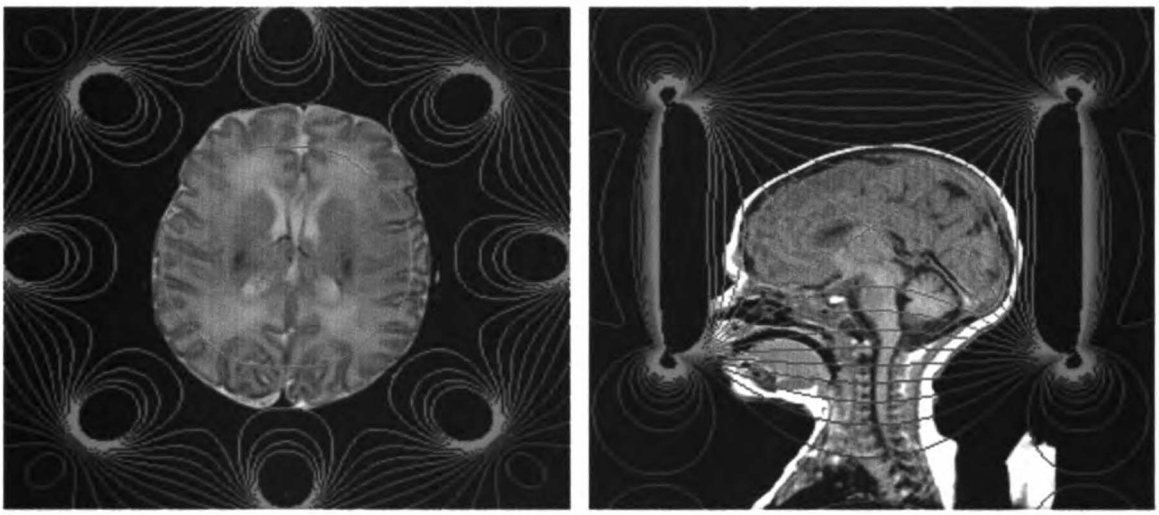

Figure 3.2. Magnetic field simulation for birdcage coil.
A simulation of the magnetic field for the prototype birdcage resonator designed at UCSF for neonatal incubator with high SNR and patient comfort.

3.2.3 Phased Arrays

In the never ending search for higher SNR, phased arrays are becoming an essential tool. Phased arrays are simple arrays of surface coil in various geometries to improve the sensitivity of the coil. [14] Due to the noise distribution, it is expected that the real signal would sum while the noise will have an expected mean value of zero. This construction allows for increased SNR and larger coverage area.

In this dissertation, small diameter, three-circular-element phased array was constructed to obtain ultra-high resolution images and spectroscopy data, shown in Figure 3.3. The three-element array was chosen due to its geometry, which enables completely inductive decoupling.

In recent developments, phased arrays are used in conjunction with various acquisition methods to allow faster and higher quality image acquisitions, so-called parallel imaging. SENSE and SMASH utilizes the spatial location of the physical coils to allow less data acquisition, but mathematically regain the information using the different signals from the individual coils of the phased array.[15, 16] This thesis work does not include any specific investigation of parallel imaging techniques, but some of the techniques developed as part of this dissertation research such as the single-shot fast spin-echo (SSFSE) diffusion sequenced discussed later will benefit greatly from the parallel imaging methods.

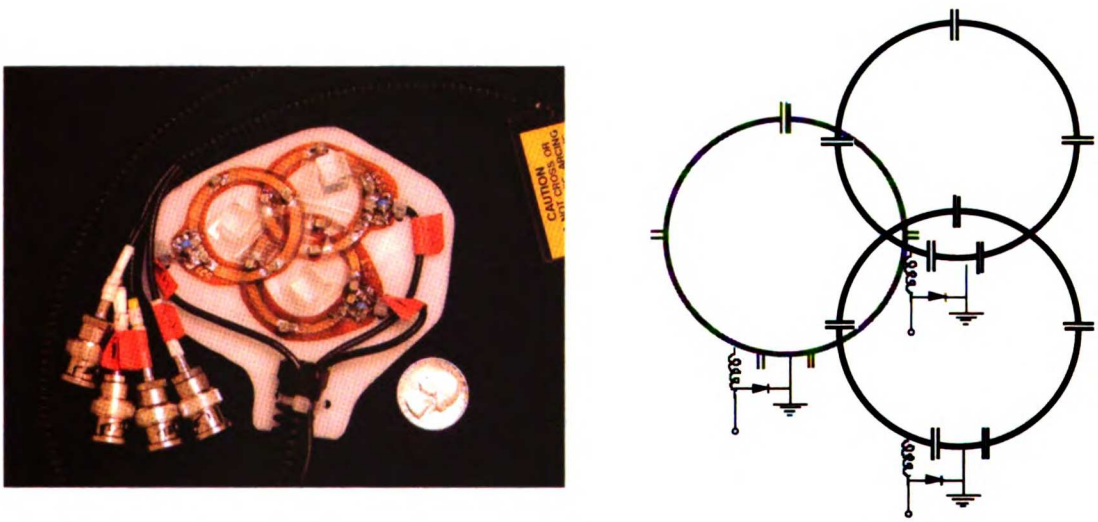

Figure 3.3. Three element surface phased array.
3-loop phased array coil with 3-cm diameter individual coils arranged in triangular shape for minimal inductive coupling.

The advantage of parallel imaging technique is that through reduced acquisition of k-space lines, a trade-off of SNR, speed, magnetic susceptibility artifact, and coverage area is enabled. For SSFSE diffusion studies, the gain in speed is critical as it has minimal amount of artifacts and in great need of improving total scan time due to the lengthy 180° pulse train in the acquisition readout. For example, in SENSE, the 180 echo train can be

halved to provide better SNR due to less T2 decay, therefore, yielding images with sharper edges. Additionally, parallel imaging would allow more slices to be acquired in the same amount of time, which is critical to the clinical uses of SSFSE, which requires much more time than the ultra-fast EPI scans. However, the trade-off effects remain to be studied and will not be discussed in this work. The following figure demonstrates the benefits of SENSE in improving EPI scans, which are at the current moment, are also being actively investigated.

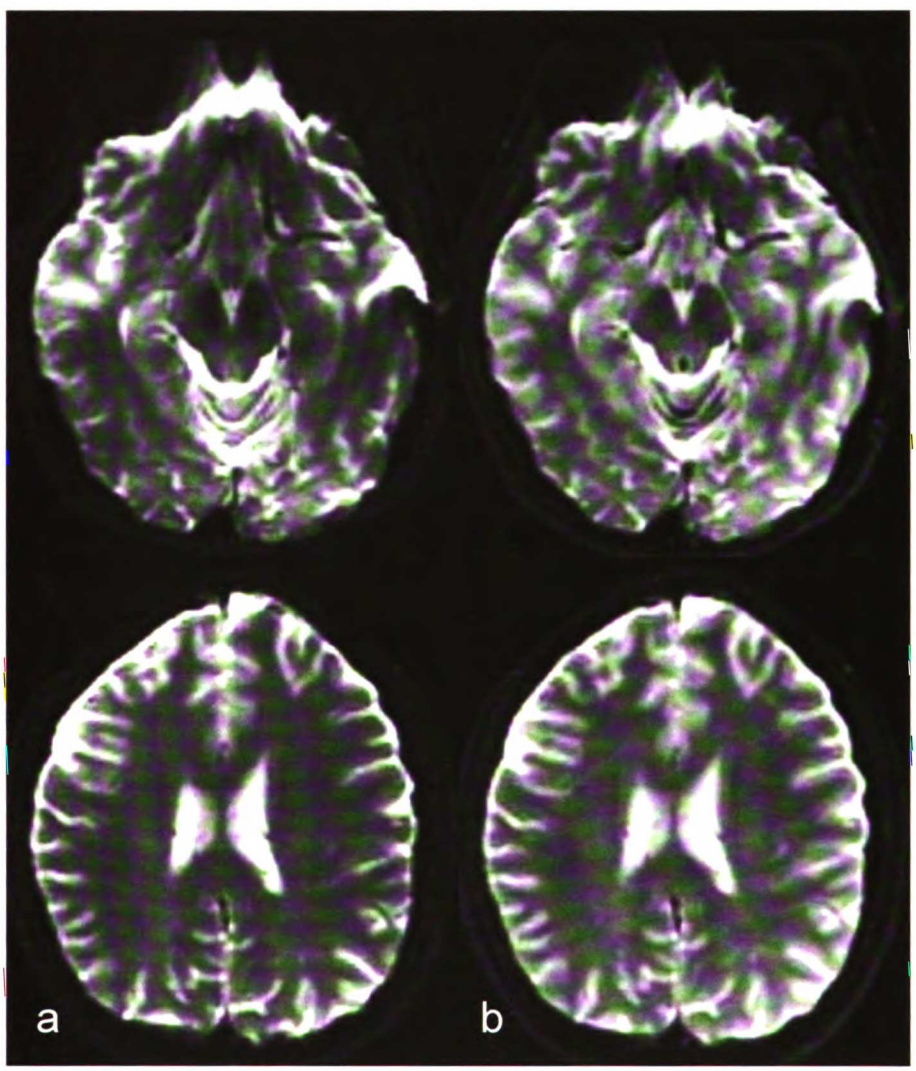

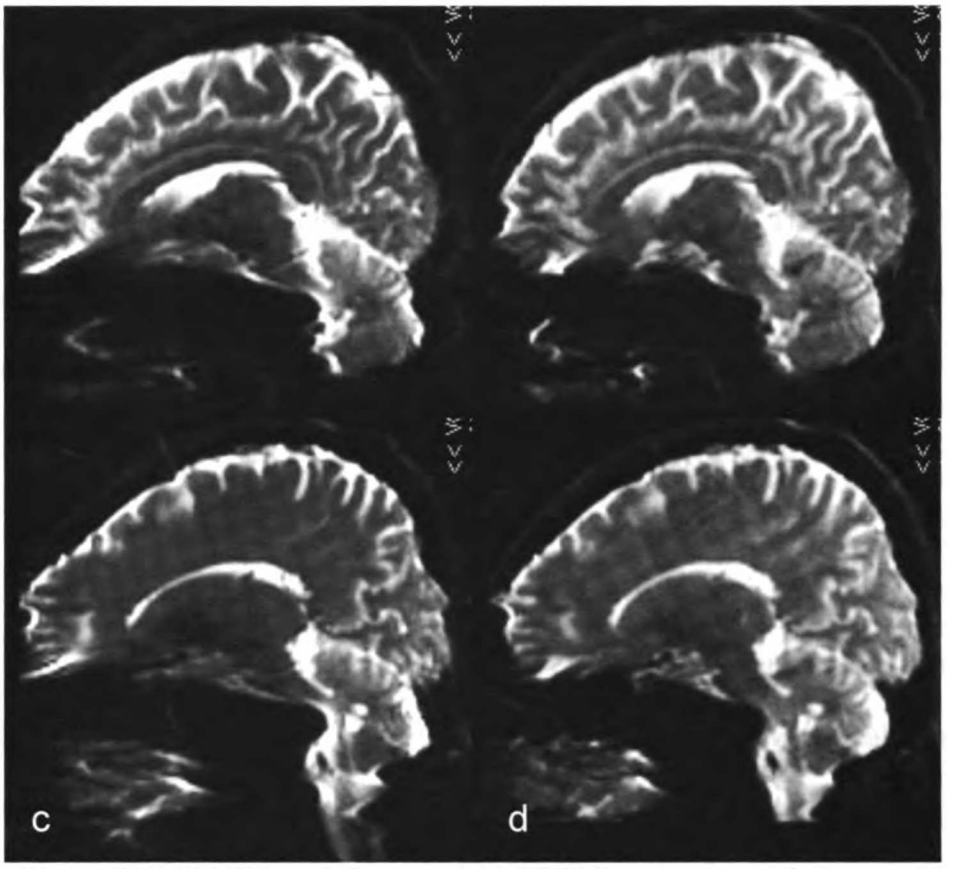

Figure 3.4. SENSE and Conventional EPI image comparison. SENSE (b, d) and conventional (a, c) EPI images of the adult brain. Magnetic susceptibility mismatch in the nasal cavity creates elongation and compression anteriorly and posteriorly.

3.3 Summary

In this dissertation work, a variety of RF coils were employed in order to achieve the desired results. Homogeneous RF excitation and reception offered by the quadrature coils continues to dominate clinical studies, in which results are quickly processed and analyzed. The new developed phased arrays were used to obtain accurate or additional information which weren't possible with conventional coils. This proved to be nontrivial and requires continued progress in terms of using the correct combination of hardware, acquisition and processing software.

4 Diffusion

Diffusion MRI is increasingly gaining diagnostic value in the assessment of patients when traditional anatomic scans offer limited information. The water diffusion parameters infer the micro-structural changes that can be detected before the gross anatomic changes. Early detection can be critical in improving successful treatment of the condition. In this section, the physical principles and parameters are discussed, followed up the introduction of a newly improved technique with its advantages and disadvantages compared to more traditional methods. Thorough feasibility tests were conducted in phantoms and volunteers before the application in clinical cases. The newly developed technique will be used in conjunction with existing radiological methods to further enhance the accurate assessment of the injury.

4.1 Introduction to Free Water Diffusion

The diffusion parameter measured in MR is the random motion of water molecules due to thermal motion, in other words, Brownian motion. Any particle with mass and in an environment with some temperature T will have a mean velocity of $\sqrt{\frac{8kT}{\pi m}}$ following the Maxwell-Boltzmann distribution. The phenomenon was first observed by Jan Ingenhousz in 1785 and rediscovered by Brown in 1828. In 1905, Einstein used kinetic theory to derive the diffusion constant, which is proportional to the root mean square of the diffusion distance. [17]

In MR, phases are accumulated and reversed using gradients. Those spins did not experience diffusion, will not have a resultant phase difference; in contrast, those spins which diffused out of the position will have a measurable phase difference.

4.1.1 Highlighting Diffusion using Gradients

The application of gradients around the 180° pulse will cause different phase accumulation for spins experiencing diffusion. The diffusion preparation is done by slice selective 90° and 180° degree pulses with diffusion gradients before and after the 180 refocus pulse. After the spins are rotated into the transverse plane by the 90 pulse, it's coherent. With the application of the gradient in one specific direction, the spins are "pushed" out of phase. When the 180 pulse refocuses the spins, the spins affected by diffusion will not come back into the coherent state. The image intensity loss is directly proportional to the size of the diffusion gradients. The shape of the diffusion gradients determines the functional form of the b value. This is discussed in depth by Stejskal and Tanner in 1968 [18].

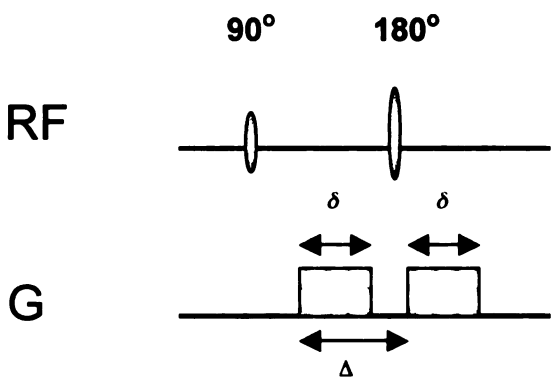

Figure 4.1. Highlighting diffusion using gradients with a spin-echo sequence.

For rectangular shaped gradients, $b = \gamma^2 G^2 \delta^2 (\Delta - \frac{\delta}{3})$. For sinusoidal gradients, $b = \frac{4}{\pi^2} \gamma^2 G^2 \delta^2 (\Delta - \frac{\delta}{4})$. For trapezoidal gradients, $b = \gamma^2 G^2 \left[\delta^2 (\Delta - \frac{\delta}{3}) + \frac{\varepsilon^3}{30} - \frac{\delta \varepsilon^2}{6} \right]$, in which ε is the rise time of the ramp.[19]

The diffusion measurement in MRI is determined by using gradients along specific directions, given by the equation, $S = S_0 \exp(-bD)$. b is the gradient factor and D is the apparent diffusion coefficient. The reason that it is called apparent diffusion coefficient is due to the fact that in MRI, the measured affect is not only as a result of the random free water diffusion, also small amount of perfusion and flow effects. When diffusion gradients are applied, the image signal intensity will be decreased as explained below. The b values is determined by the gradient configuration and the diffusion coefficient D can be computed.

4.1.2 Restricted Diffusion

In physiological studies, the diffusion parameter directly infers tissue information due to the fact that free water diffusion only occurs in relatively small areas. Most of the tissues have membrane structures, which water cannot diffuse freely across. [20] This restriction allows the inference of the status of these membrane structures. For example, neuronal axons, shielded by myelin, will have very restricted water diffusion across the cross-section of the axon; however, diffusion is much less restricted along the axon. This anisotropic property of the axons is useful in identifying white matter pathways and in the assessment of diseases that compromise the integrity of axons. [21]

4.2 Technique Development—SSFSE vs. EPI Diffusion

4.2.1 Image Acquisition Strategies

The robustness of MRI comes from in part of the acquisition schemes available allowing different k-space trajectories to be performed to change the properties of the final image outcome. Gains in one area will lead to degradation of quality in another area. For example, time can be traded for better SNR and contrast can be traded for better overall image intensity. Hence, the acquisition method is critical in obtaining the optimal image.

Traditionally, the diffusion images have been acquired using the EPI method, which allowed extremely fast acquisition times and good SNR. However, the EPI method suffers from spatial distortions due to magnetic inhomogeneity such as magnetic susceptibility. The oscillating gradient refocusing train in EPI is sensitive to the local field inhomogeneities. Very often, areas with essential diagnostic values are left untouched due to the fact that values are skewed by those distortions. The following section deals with one alternative method of using single-shot fast spin echo (SSFSE) in minimizing distortion, in which the local field effects are compensated by the refocusing 180^{o} RF pulse train.

4.2.2 Pulse Diagram

Diffusion measurement using the SSFSE method is acquired with the pulse sequence shown in the following figure.

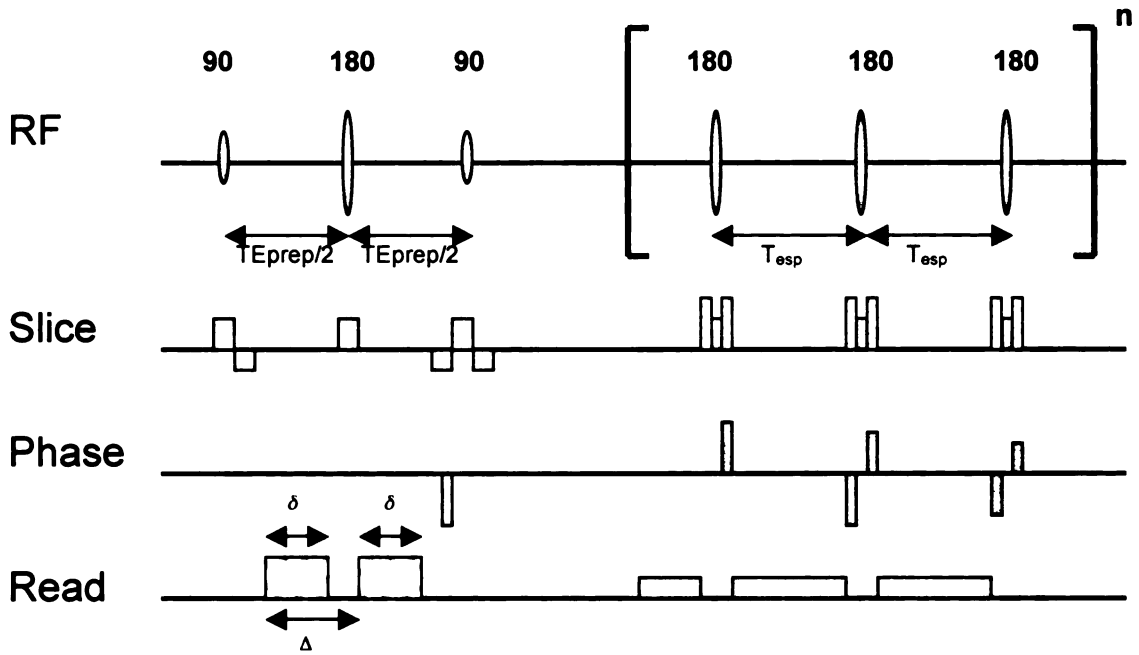

Figure 4.2. SSFSE pulse diagram.
SSFSE pulse diagram with diffusion highlighting preparation pulses followed by a train of 180 RF pulses. Tesp is the time spacing for the train of refocusing pulses.

The acquisition sequence is a basic single shot fast-spin echo method with a diffusion preparation described above with a few modifications. The first 90x-180y are the same as the standard diffusion preparation pulses. An extra 90y is added obtain a CPMG phase condition to eliminate possible stimulated echoes in the echo train. This pulse is also slice selective. In order to maintain the phase of the spins, the phases are pre- and post-compensated as demonstrated on the Slice gradient line. Another gradient in the y direction is also added to make sure that the spins on one axis will be maintained for the imaging train, which also means that half of the spins are lost, resulting in less SNR. But this is necessary to maintain the phase condition to yield images without any ghosts from stimulated echoes. The strength of this addition y gradient is not as important as the duration, which should correspond to one cycle of the phase encode gradients.

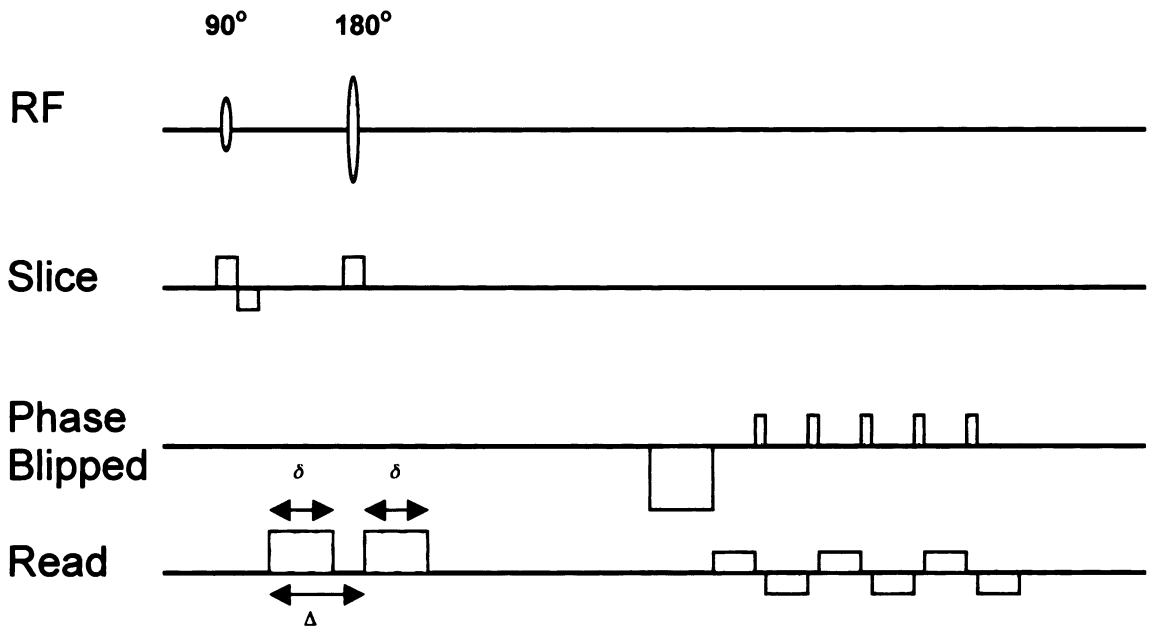

Figure 4.3. EPI pulse diagram.
EPI pulse diagram with diffusion highlighting preparation pulses followed by a train of gradient lobes for echo generation.

4.2.3 Other Acquisition Methods

There are also other approaches in minimizing the air-tissue interface distortion such as the "propeller" method [22, 23] and parallel imaging methods [24, 25]. Both provide significant reduction of artifacts, but at different trade-offs.

The propeller method uses multiple-shot of fast spin echo acquisition scheme, in which several lines of k-space is acquired during one TR and followed by an angular rotation of the acquisition, resulting in blade appearing sections. [22] The advantage is that the center of k-space is oversampled, therefore, providing excellent image intensity. At the same time, this scheme is robust against motion as the image acquisition is self-navigated as the blades always contain the center of k-space. This method compared to SSFSE is

more time consuming and also introduces additional artifacts from filling the k-space in a circular fashion.

Parallel imaging methods such as SENSE and SMASH have been recently developed and included on commercial scanners [26-28]. They dramatically reduce artifacts when used with EPI in diffusion studies. However, at this moment, clinical studies are being conducted to study the effects of small computation artifacts introduced during the image reconstruction. It is worthwhile to note that these parallel imaging methods are also compatible with the SSFSE acquisition, in which the echo spacing can be reduced to offer sharper images. With reduced echo spacing, therefore, the shortened echo train, the T2 blurring effect in the SSFSE will be lessened, which will result in images with sharper edge definition.

4.2.4 Quantitative Analysis of SSFSE vs EPI Diffusion Distortions

Abstract

Brain tumor 3T clinical diffusion studies using EPI acquisitions demonstrate dramatic distortions on the resultant images due to magnetic susceptibility artifacts and alternating gradient switching. These susceptibility artifacts are especially pronounced in tumor masses and adversely affect the ability to provide accurate DTI parameter maps. SSFSE-DTI studies at 1.5T have demonstrated minimally distorted images and accurate diffusion parameter measurements [29]. In this study, analysis of the deformation parameters in non-rigid registrations and brain shape characteristics demonstrated significantly larger distortions in EPI-DTI than SSFSE-DTI in brain tumor patients at 3T while the ADC values were comparable in non-distorted regions. Analyses were also performed to

investigate the use of SSFSE-DTI in obtaining diffusion parameter values, in the tumor regions near the resection cavity. In the T2 hyperintense regions, the ADC was significantly higher than for normal brain tissue as indicated in previous studies.

Introduction

Newly diagnosed primary brain tumor patients are numbered in the thousands each year. Due to the difficulties in early diagnosis, treatment, and follow-ups, the survival rate of tumor patients is still low. Through the use of more advanced MR techniques, additional information can be obtained and utilized in the treatment planning. Routine clinical diffusion studies typically use echo planar imaging (EPI) acquisitions, in which alternate gradient switching and magnetic susceptibility mismatches at air-tissue interfaces and in brain tumor masses cause noticeable distortions on the resultant images. These image artifacts are more pronounced at 3T and adversely affect the ability to provide accurate DTI analyses of those regions. Many important regions that are sites for residual tumor and possible recurrence cannot be directly monitored by diffusion using EPI due to large spatial distortions. Recently, investigations of the use of single-shot fast spin-echo (SSFSE) methods have demonstrated minimal distorted images, which also provide accurate diffusion parameter measurements [29]. However, due to the complexity of the artifacts, it is necessary to quantify the distortions and apply the analysis to evaluate the techniques.

Methods

Six volunteers and nine brain tumor patients were scanned using a GE 3T MR scanner. The volunteer scans included a standard FSE T2 image for standard minimally distorted

image for comparison, an EPI diffusion and SSFSE diffusion. The images were acquired at same resolution of 256x128 with a square FOV of 22cm.

The brain tumor patients were scanned as a part of the established clinical/research protocol. The protocol includes: a pre-contrast 3D SPGR, axial T2 FLAIR, diffusions, perfusion during contrast injection, and post-contrast 3D SPGR and axial T1. The EPI and SSFSE diffusion images were aligned and compared to the T1 SPGR images. The brain images were extracted using threshold and morphological operations.

Apparent diffusion coefficient (ADC) values were compared using the paired t-test in non-distorted regions between the EPI and SSFSE based acquisition. The ADC values were computed in the T2 hyperintense region of the tumor patients.

Non-rigid registrations between the image sets were calculated. The images were registered to the anatomical image by optimizing the positions of a regular grid of B-spline control points [30]. The optimal deformation was determined by maximizing the normalized mutual information using a gradient ascent search method. The transformation was inverted and the deformation vectors mapped onto the anatomical image. A histogram analysis of the magnitude of the deformation vectors was then performed.

Another quantitative analysis of the image distortions involving curvature of the brain contour was also investigated. The pixels along the edge of the brain were fitted to create

a Bezier spline. Angles were computed from the normals at each of the points, followed by the computation of the derivatives, giving a measurement of the curvature of the edge. Then histograms of the absolute values of the curvature (bins from 0-359°) were computed and compared using the χ^2 test statistic, a simple and effective measure of histogram similarity [31].

Results

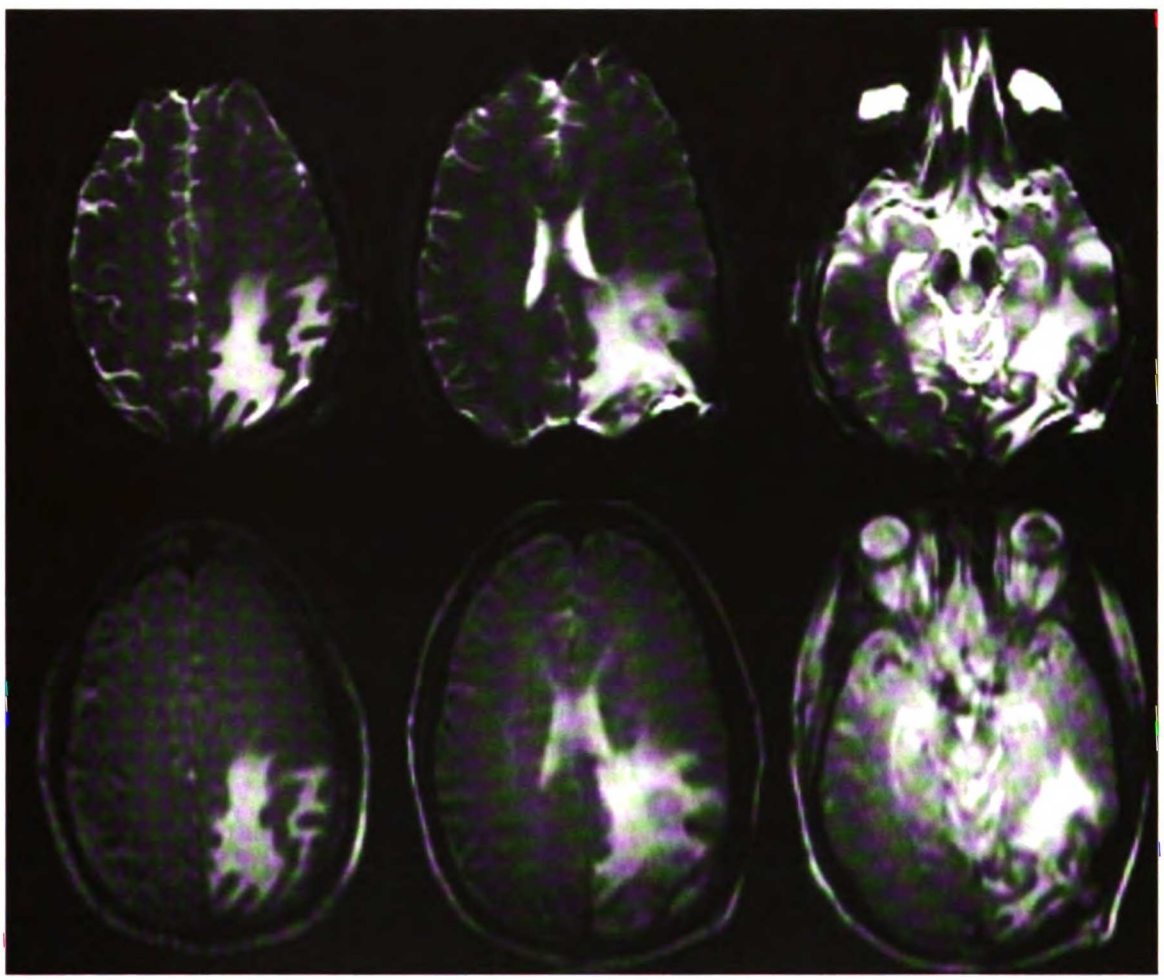

Figure 4.4. DTI- SSFSE and EPI images of brain tumor.
The upper row images are acquired using EPI and lower row images are acquired using SSFSE based method. The EPI images demonstrate the magnetic susceptibility artifacts near the nasal cavity and tumor mass while the SSFSE based DTI acquisition showed minimal distortion.

As shown in the Figure 4.4, magnetic susceptibility artifacts cause noticeable distortions anteriorly and in tumor masses in the EPI based images.

Histograms of the distortion vector magnitudes for the slice displayed in Figure 4.5 are shown in Figure 4.6. For this slice, the mean displacement was 1.58 times greater in the EPI than the SSFSE images. The 95th percentile of the EPI distortion magnitudes was 7.87 mm, compared with 3.33 mm in the SSFSE. This reflects the increased number of voxels with large spatial shifts in the EPI images relative to the SSFSE images.

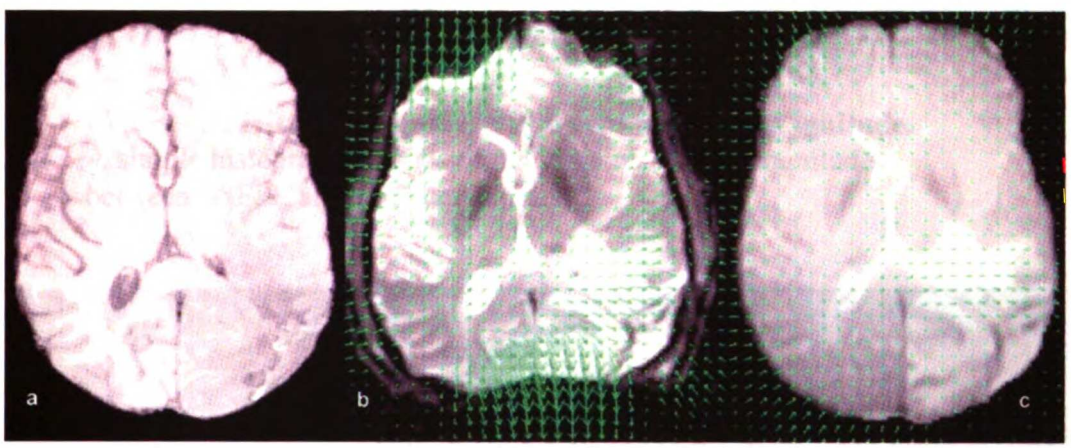

Figure 4.5. Magnitude of warping vectors for EPI and SSFSE.
Magnitude of warping needed to align EPI (b) and SSFSE (c) based diffusion acquisitions with FSE (a). EPI shows large anterior and posterior distortions, whereas SSFSE images are minimally distorted.

As the curvature analysis has demonstrated in Figure 4.5, the shape of the SSFSE-DTI brain is more similar to that of the SPGR than the EPI acquired brain. The sharp changes in the edges of the brain produced a good indication of the distortions. Although this method is highly dependent on the mask of the image sets, even with the simple method of thresholding and morphological operations, the results still lead to a quantitative

indication that the EPI is distorted more than the SSFSE diffusion images. For this slice, the χ^2 comparison for the SSFSE is 0.28 and EPI is 0.37.

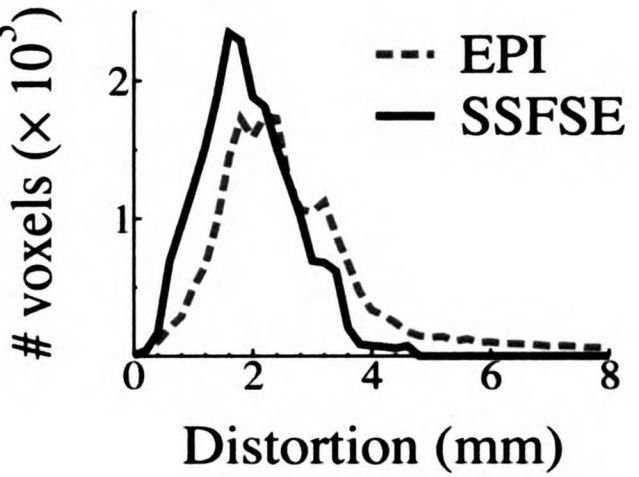

Figure 4.6. Histogram analysis of warping vector magnitude.
A simple histogram analysis of the warping vector magnitude between SSFSE and EPI acquisitions.

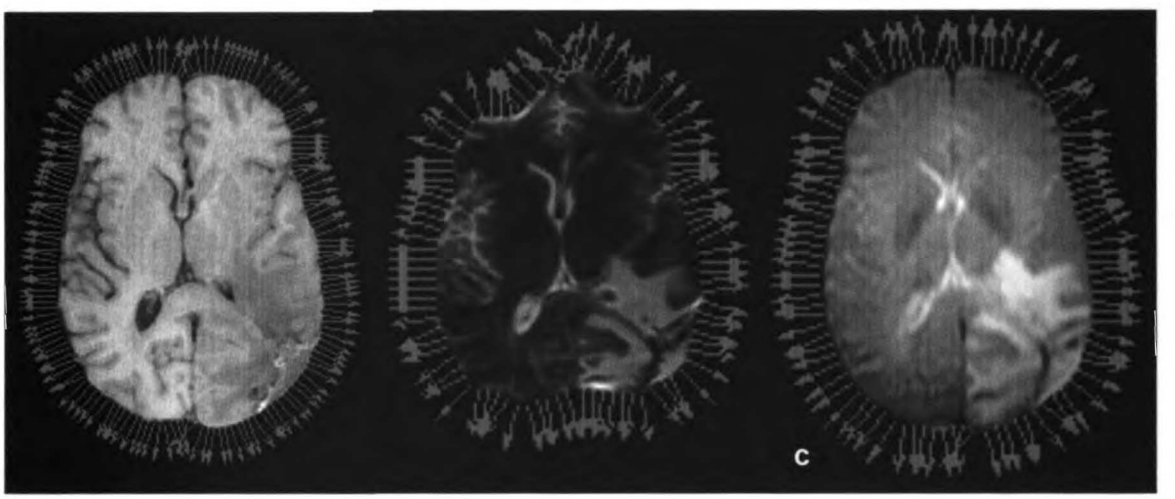

Figure 4.7. Curvature analysis of FSE, EPI, SSFSE acquisitions.
The vectors are normals to the B-spline of the edge of the brain. FSE (a), EPI (b), and SSFSE (c) images of a patient with brain tumor. The magnetic susceptibility distortions caused sharp changes in the contours of the edge. The additional susceptibility around the tumor contributes to the curvature changes.

Discussion

EPI-DTI of brain tumor patients with resection cavities demonstrated large distorted areas on the images. Clinically the assessments of resection rims are critical in evaluating the progression of tumor and were much better depicted by SSFSE-DTI. The SSFSE showed minimal distortion; therefore, the measured diffusion values measured are more correctly aligned with the anatomy while providing statistically similar apparent diffusion coefficient values in the non-distorted regions compared to EPI ($P>0.05$).

In this section, the SSFSE based DTI method was demonstrated quantitatively to have less artifact than the EPI based acquisition while maintaining similar diffusion parameter measurements.

4.3 *In Vivo* Feasibility Study

Introduction

Diffusion weighted magnetic resonance imaging (DWI) has been increasingly useful in clinical diagnoses of conditions in which conventional imaging methods yield inconclusive results. DWI often provides a different image contrast resulting from water diffusion changes, which very often precedes morphologic changes on conventional anatomic MRI [32-35]. In diffusion studies, the average eigenvalue of the diffusion tensor ($\overline{D}$) and the relative anisotropy (RA) maps are two main analyses. $\overline{D}$ measures the spatially-averaged mobility of free water, whereas anisotropy maps provide information about the directionality of water diffusion. For example, water diffusion is hindered across the diameter of the axon due to the lipid bilayer of the axonal membrane and the multiple lipid bilayers of the myelin sheath; water diffuses more freely along the

long axis of the axon. This anisotropic motion results in a higher RA value and can reveal the direction of axonal fascicles. Furthermore, the diffusion studies are no longer limited to the brain as more and more acquisition methods and post-processing techniques are available to image other regions of the body such as the spinal cord and vertebral discs [36, 37]. The vast majority of diffusion MR studies have used single shot echo-planar imaging (EPI) based acquisitions that are rapid and routinely available on clinical MR systems. However, EPI utilizes gradient rephasing, which result in spatial distortions from magnetic susceptibility effects, especially near air interfaces [32-35]. Recent studies have demonstrated the feasibility of using radio-frequency or RF-refocused single shot fast spin-echo based diffusion MR acquisitions which provide images without significant degree of spatial distortions that affect EPI-based diffusion imaging [38-40]. The purpose of this study was to implement a DTI single shot fast spin echo (SSFSE) sequence at both 1.5T and 3.0T and to investigate diffusion tensor imaging of the brain and cervical spinal cord using both conventional head coils and high sensitivity phased-array coils. Our hypothesis was that the use of SSFSE would enable better co-registration with high-resolution anatomical and spectroscopic images and thus facilitate the investigation of various developmental and degenerative disorders. Also, we sought to evaluate applications of this sequence at 3.0T, where the distortions from magnetic susceptibility inherent in EPI are much larger than at 1.5T.

Methods

A tensor SSFSE sequence was written for both 1.5T and 3.0T Signa EchoSpeed systems (GE Medical System, Milwaukee, WI), with the acquisition of six gradient directions ([1 0 1], [-1 0 1], [0 1 1], [0 1 -1], [1 1 0], [-1 1 0]) enabling the calculation of the diffusion

tensor and its eigenvalues, λ_1, λ_1, λ_3. In order to utilize the gradients efficiently, instead of the circular gradient construction of the matrix, a tetrahedral shape was employed, in which two diffusion gradient directions are active at one time. The gradient values were normalized by $\sqrt{2}$, therefore, the relative image intensities of the acquired images are scaled similarly, enabling easier post-processing.

The six acquisitions will yield a matrix of $\begin{bmatrix} D_{xx} & D_{xy} & D_{xz} \\ D_{yx} & D_{yy} & D_{yz} \\ D_{zx} & D_{zy} & D_{zz} \end{bmatrix}$, which is diagonally symmetrical, allowing the completion of the tensor with less measurements. It is significant due to the limited time of scan in clinical settings. The diagonalization of the matrix yields the eigenvalues, $\begin{bmatrix} \lambda_1 & & \\ & \lambda_2 & \\ & & \lambda_2 \end{bmatrix}$, which are used to describe the diffusion.

Rotationally invariant mean diffusion ($\overline{D}$), relative anisotropy (RA), and fractional anisotropy (FA) maps can be calculated from the eigenvalues of the tensor construction, using the following equations described by Basser et al: $\overline{D} = \frac{\lambda_1 + \lambda_2 + \lambda_3}{3}$, $RA = \frac{\sqrt{Var(\lambda)}}{Mean(\lambda)}$, $FA = \frac{1}{\sqrt{2}} \frac{\sqrt{(\lambda_1 - \lambda_2)^2 + (\lambda_2 - \lambda_3)^2 + (\lambda_1 - \lambda_3)^2}}{\sqrt{\lambda_1^2 + \lambda_2^2 + \lambda_3^2}}$ [41]. In this study, only $\overline{D}$ and RA were studied.

Phantom Studies:

A spherical water phantom was used to compare the DTI-SSFSE sequence to the DTI-EPI based tensor sequence at 1.5T using a standard clinical head coil. The imaging parameters are FOV of 24cm, section thickness of 5mm at 5mm intervals, 256x128

FreqxPhase with 1.0 Phase FOV, and the b-value of 1000 s/mm^2. The $\overline{D}$ and RA maps were calculated using in-house, custom-written Fortran and C software. The quantitative region-of-interest values from the phantom were obtained from a program written in Interactive Data Language (IDL).

At 3.0T, SNR values were obtained in volunteer studies from head coils and phased array coils using spin-echo images and gradient-echo images, acquired using a FOV of 24 cm, thickness of 5 mm, encoding matrix of 256x160, Phase FOV of 1, and 1 NEX.

Adult Brain Studies:

The volunteers were aged 22-52 years with no history of any serious illnesses and gave informed consent following a protocol approved by the committee on human research at our institution. Each subject was screened for safety reasons and to exclude the presence of metal objects.

Studies were performed on both 1.5T and 3.0T MR scanners. Subject scans were acquired with a FOV of 24cm, thickness of 5mm, 256x128 FreqxPhase with 0.6 Phase FOV. Then the images were re-sampled using a tri-linear interpolation algorithm to a FOV of 24cm with 256x256 in post-processing.

In the brain study, a total of 10 healthy volunteers were imaged using both the DTI-SSFSE and DTI-EPI sequences with a standard clinical head coil. For diffusion, b value was 1000 s/mm^2 for adult studies. Due to longer time of repetition (TR) in the SSFSE,

SNR is lower than for the EPI images acquired within the same amount of time. Multiple numbers of excitation (NEX) were employed to obtain higher SNR through signal averaging for both sequences. The acquisition time was 4 minutes for a 4 NEX acquisition with 8 slices for DTI-SSFSE and the same parameters were used in the DTI-EPI acquisition. Regions of interest (ROIs) in the brain were selected in the basal ganglia, thalamus, and posterior limb of the internal capsule. Attempts were made to obtain similar regions in each volunteer, although the exact same slice locations were not available for every exam. Statistics were performed utilizing a standard t-test.

For the 3.0T brain imaging study, a total of 5 volunteers were imaged using the head coil, and 2 of the 5 volunteers were also imaged with a 4-element Pediatric Bitemporal Array made by Nova Medical Inc. (Wakefield, MA, USA). The phased array set was placed on opposite sides of the head and positioned to cover the regions of interest. The DTI-EPI and DTI-SSFSE comparison was performed with the volume head coil with a FOV of 22 cm, thickness of 3 mm, a 192x128 matrix, NEX=2, and Phase FOV of 1. The phased array diffusion images were acquired with FOVs of 16-20 cm, thickness of 3 mm, 128x128 FreqxPhase, and Phase FOV of 1.

Neonatal Brain Studies:

The neonatal patients were recruited as a part of an ongoing research protocol. Parental consent was obtained in all cases following a protocol approved by the committee on human research at our institution. Neonatal patients were scanned only at 1.5T in the sagittal plane using the same DTI-SSFSE with a FOV of 22 cm, acquisition matrix of

256x128, and a b value of 600 s/mm^2 to correlate with the EPI tensor diffusion in our standard research protocol. The MR coil in this study was a prototype neonatal head coil designed to be used with a neonatal MR compatible incubator [42]. Then, the data were evaluated similarly to the adult studies.

Adult Spine Studies:

In the cervical spine study, 5 volunteers were imaged at 1.5T with similar imaging parameters as the adult brain studies using a custom-built neck coil. The neck coil was two serial rectangular, receive-only phased array coils, which conformed to the shape of the neck; therefore, giving the advantage of the close proximity to the subject, offering much higher SNR and better coverage than the standard clinical head coil [43]. The phased array coil has a total of 4 channels. Following standard practice for phased arrays, the signal, used to form the image, was derived by summing the squares of the signals from each channel. Other signal aggregations are possible, but the sum of squares provides the simplest and quickest way to effectively quantify the signal for image formation.

For the cervical spine, ROIs were manually drawn in the intervertebral disc and the spinal cord to obtain the $\overline{D}$ and RA values. All of the ROIs were defined on the $\overline{D}$ map from the DTI-SSFSE and the same ROIs were applied to the RA maps obtained from DTI-SSFSE and the $\overline{D}$ and RA maps from EPI.

Results

Phantom Images

The water phantom data showed no significant differences between the computed values of $\overline{D}$ and RA between the DTI-SSFSE and DTI-EPI acquisition methods. However, the distortions caused by magnetic susceptibility artifact from the air bubble in the water phantom can be clearly seen in Figure 4.4c using the EPI method, as compared to the spin-echo method acquired T2 weighted image (Fig. 4.8a) and the DTI-SSFSE diffusion image (Fig. 4.8b). At 1.5T, the phantom from the EPI images showed a 16% shortening from the edge of the water bubble to the opposite end of the phantom, whereas SSFSE showed no noticeable distortions. At 3.0T, the image distortion in the EPI acquisition increased to 20%; in comparison, the SSFSE still showed <1% distortion.

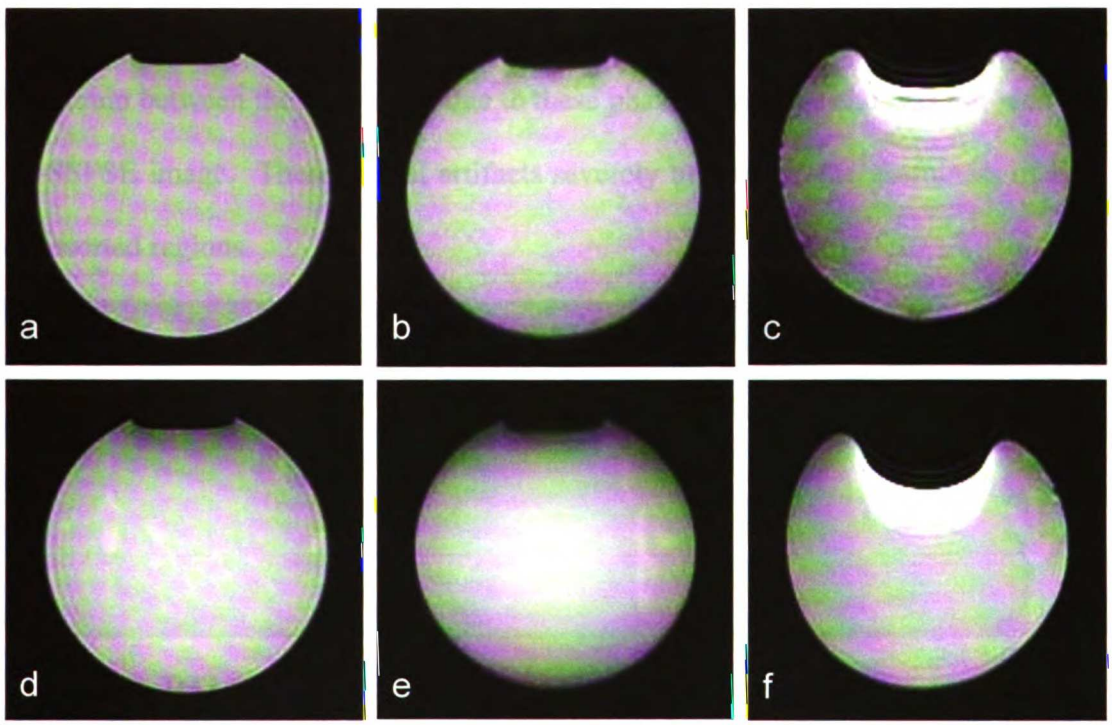

Figure 4.8. Distortion comparison using different sequences in phantom. T2-weighted axial imageswere acquired with a standard spin-echo sequence (a,d), the DTI-SSFSE sequence with b=0 s/mm2(b, e), and the DTI-EPI sequence(c,f). with b=0 s/mm2. The images were acquired at 3.0T from a 10cm circular phantom with an air bubble using standard head coils with the top row (a,b,c) images acquired at 1.5T and the bottom row (d, e, f) at 3T.

Adult Brain Images

The minimal distortion of the DTI-SSFSE compared to the DTI-EPI was demonstrated again in the human adult volunteer at 1.5T (Figure 4.9) and at 3.0T (Figure 4.10). The axial brain image from the EPI (Figure 4.9b) was distorted both anteriorly and posteriorly, compared to the image obtained by DTI-SSFSE (Figure 4.9a). The distortions were the direct result of phase errors in the EPI sequence, as it does not refocus all the magnetization dephasing caused by inhomogeneities. The phase errors translate into spatial errors in the final image. The shapes of the eyeballs demonstrate the severity of the distortion from the air-tissue interface from the nasal cavity; instead of spherical eyeballs, the EPI showed oblique, elliptical eyeballs. Similarly, the protrusion of the brain between the eyeballs is due to these phase distortions and was not seen in the DTI-SSFSE image. These spatial artifacts severely undermine the usefulness of EPI in the distorted regions.

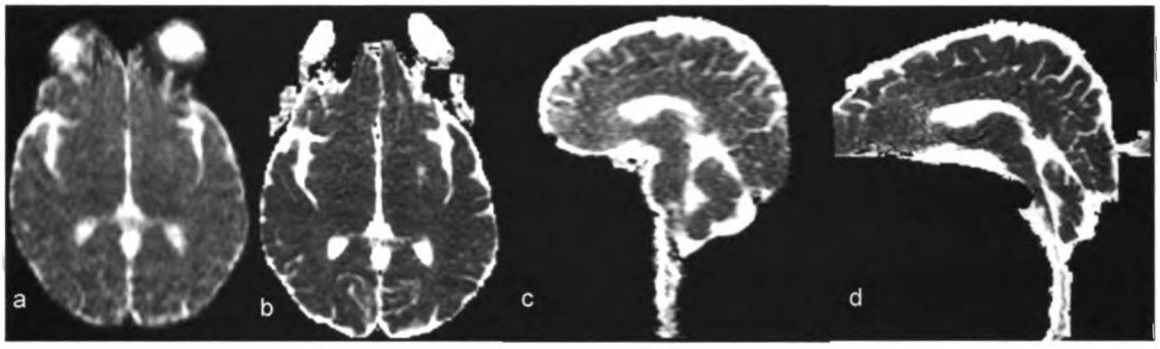

Figure 4.9. DTI-SSFSE and DTI-EPI image comparison at 1.5T.
Axial and sagittal images acquired by DTI-SSFSE (a,c) and DTI-EPI methods (b,d) at 1.5T. The EPI images are sustantially distorted due to magnetic susceptibility differences caused by air-tissue interfaces.

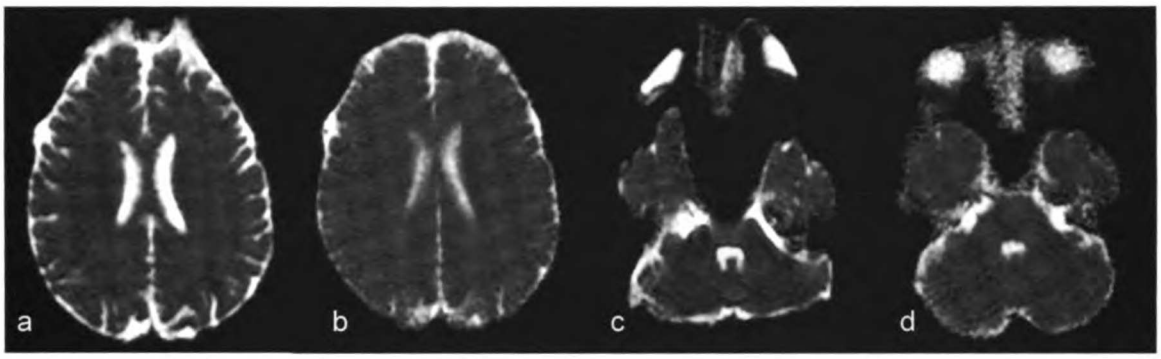

Figure 4.10. DTI-SSFSE and DTI-EPI image comparison at 3.0T.
Magnetic susceptibility effects caused substantial distortions in DTI-EPI maps (a, c) but not in the corresponding DTI-SSFSE (b, d) images shown for two axial slices at 3.0T.

The sagittal section of the brain from the EPI demonstrates similar distortions from the paranasal sinuses interface anteriorly at frontal lobe and posteriorly at the brain stem. The more pronounced phase error induced shape changes are clearly seen in Figure 4.9d. In the example shown, the brain in Figure 4.9d is approximately 20% longer in anterior-posterior direction than the minimally distorted brain of Figure 4.9c, a DTI-SSFSE image. The lateral contour of the cerebellum has a round shape as demonstrated in Figure 4.10d, but on the EPI image (Figure 4.10c) it appears misshapen behind the distorted temporal lobes and the petrous bones, and surrounded by the bright signal of the cerebral spinal fluid (CSF). The distortion is not limited to the cerebellum with the ventricles and the spinal cord also displaying irregular shapes (Figure 4.9d). The posterior horn of the lateral ventricle is slightly elongated in the superior-inferior direction and shortened in the anterior-posterior direction. The spinal cord is seen as abnormally curved on the DTI-EPI image (Figure 4.9d), while it is almost straight anatomically, as better seen on the DTI-SSFE image (Figure 4.9c).

In addition to the magnetic susceptibility-induced image distortions, the EPI image Figure 4.9d also demonstrated an aliasing problem for that acquisition. The field-of-view (FOV) should have been large enough and correctly positioned to cover the entire brain. However, due to the spatial distortions, the brain image was enlarged in the phase direction, which can be seen by the phase-wrapped frontal lobe tissue in the posterior of the brain. This creates even more issues in post-processing and image analysis if not corrected.

$\overline{D}$ ($x10^{-3}$ mm^2/s)			
	Basal Ganglia P>0.73	Thalamus P>0.63	Posterior Limb of Internal Capsule P>0.66
DTI-SSFSE	0.747±0.060	0.724±0.052	0.731±0.066
EPI-DTI	0.750±0.067	0.730±0.084	0.725±0.076
Relative Anisotropy			
	Basal Ganglia P>0.73	Thalamus P>0.84	Posterior Limb of Internal Capsule P>0.58
DTI-SSFSE	0.243±0.080	0.298±0.111	0.434±0.126
EPI-DTI	0.249±0.113	0.302±0.122	0.447±0.092

Table 4.1. $\overline{D}$ and RA comparison between SSFSE-DTI and EPI-DTI for brain ROIs.

Table 4.1 shows that there is no statistically significant difference between the computed values of $\overline{D}$ and RA from the DTI-SSFSE and the DTI-EPI sequences in non-distorted regions.

In the 3.0T head coil comparisons, Figure 4.10 demonstrates no discernable distortions for DTI-SSFSE and, although the DTI-EPI demonstrated higher SNR, the distortions were dramatic and would limit accurate measurements of DTI parameters in many regions. The relatively large distortions from the paranasal sinuses in the traditional EPI severely limit quantitative measurements. The SNR gains from using the phased array

were measured at approximately 4-6 times that of the 3T head coil over cortical regions and up to 8 times at the surface depending on the individual. This gain permitted high resolution $\overline{D}$ and anisotropy maps in which the white matter tracts are clearly delineated (Figure 4.11, Figure 4.12c,d). Furthermore, Figure 4.12 demonstrates the SSFSE-DTI's capability to utilize eigenvalue analysis to show directionality of the fiber tracks with color overlays utilizing similar techniques reported by Pajevic and Pierpaoli [44].

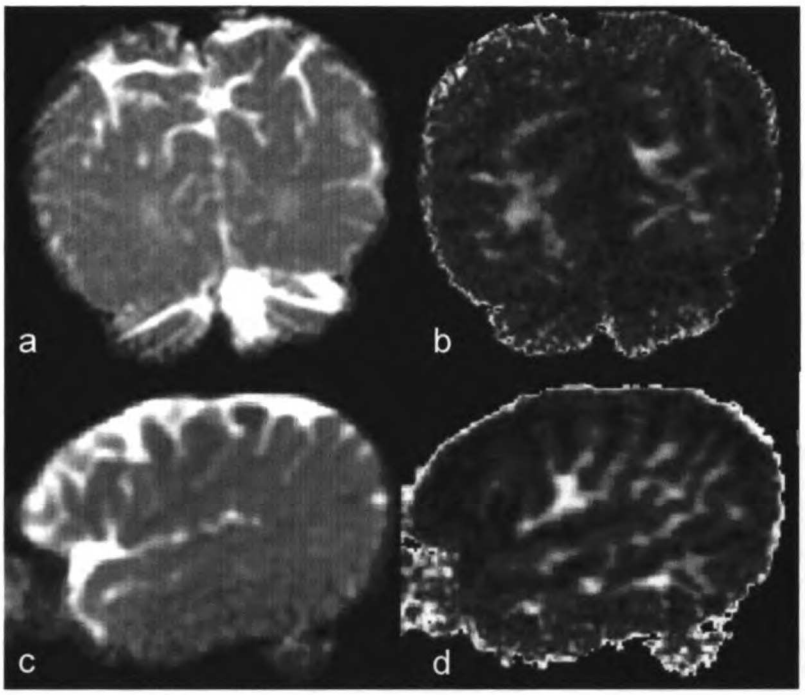

Figure 4.11. DTI-SSFSE diffusion parameter maps acquired at 3.0T.
DTI-SSFSE $\overline{D}$ (a,c) and relative anisotropy (b, d) maps of the occipital lobe (a,b, coronal) and sagittal images of the frontal and parietal lobes acquired using phased-array coils at 3T. Note the clear depiction of subcortical white matter tracts in the anisotropy maps.

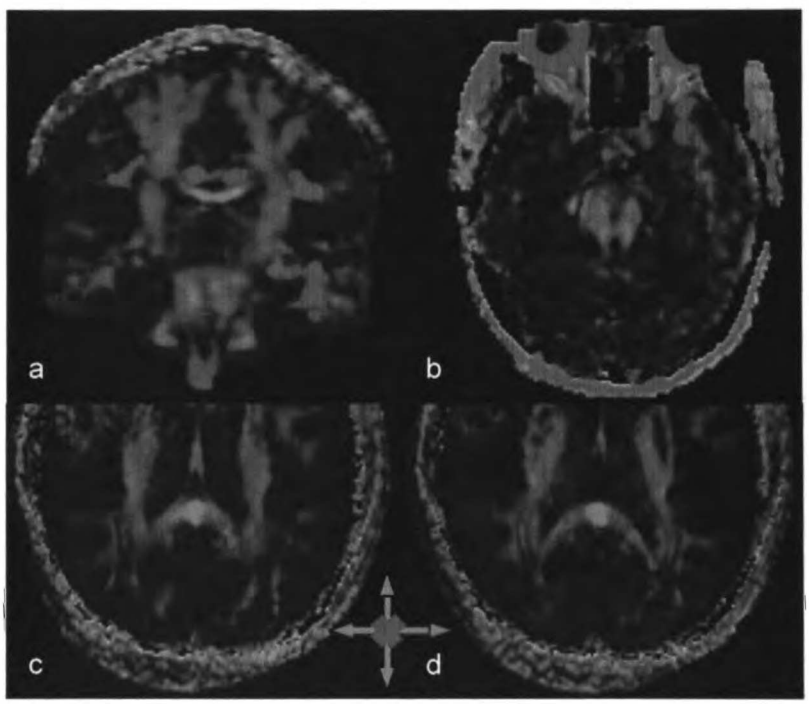

Figure 4.12. Color coded anisotropy maps.
Color eigenvector/RA maps were calculated from sagittal (a) and axial (b) DTI-SSFSE images acquired at 1.5Tusing a standard head coil in 6 minutes. Phased-array 3T maps (c,d) acquired in 7 minutes at 3T demonstrate improved depiction of white matter tracts. Red denotes R/L, Green denotes A/P, and Blue denotes S/I directions.

Neonatal Brain Images

These studies demonstrated the ability of DTI-SSFSE to obtain diffusion data from the cerebellum and brain stem in a 28 week old neonatal patient with a cerebellar hemorrhage (Figure 4.13). The study is performed as a part of an established protocol, which includes T1, T2, spectroscopy, EPI diffusion, in the clinical assessment of premature babies.

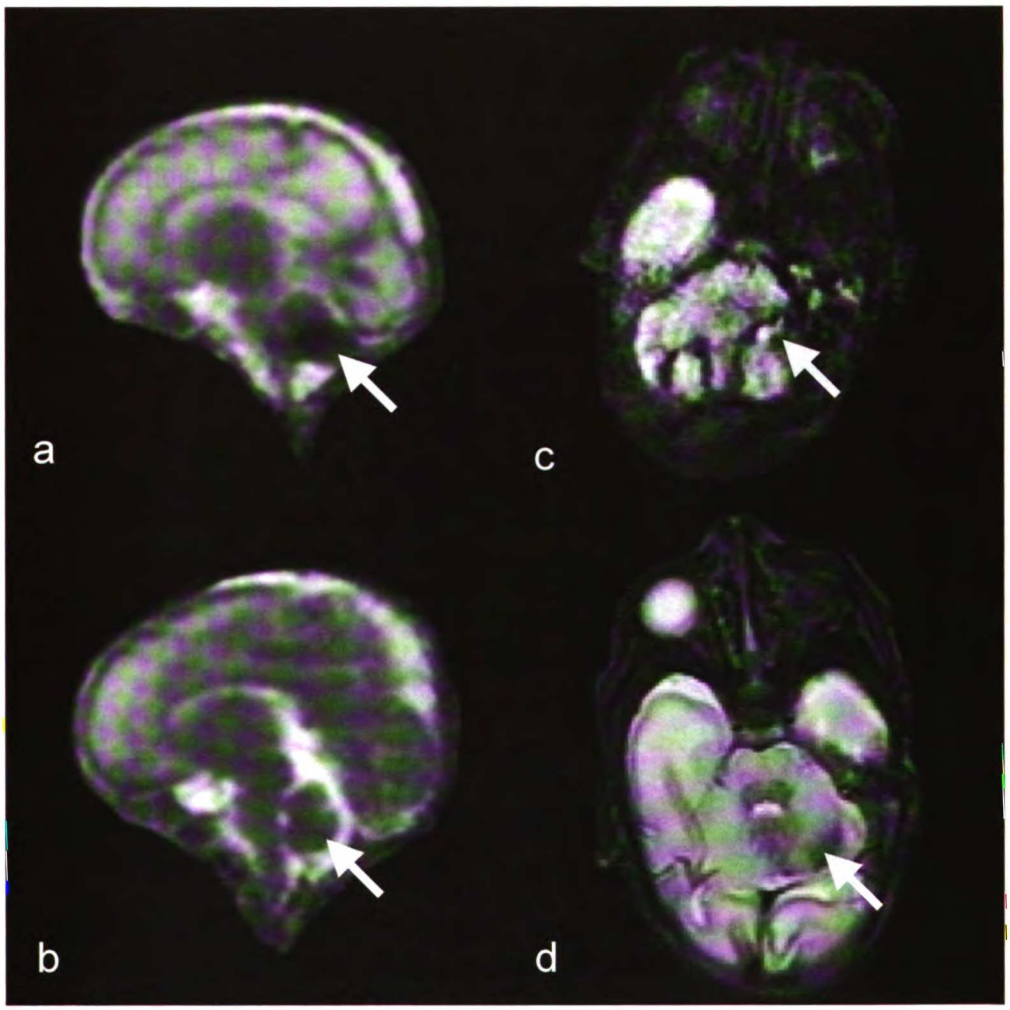

Figure 4.13. Clinical case study of neonate using DTI-SSFSE
A clinical case of premature infant with cerebellar hemorrhage utilizing $\overline{D}$ (images a, b) and T2 (images c, d) at 1.5T. Images a and c were obtained approximately 3 weeks before the follow-up exam, images b and d. Note lack of spatial distortions in the ADC images even in the region of the hemorrhage.

This patient study showed negligible spatial distortions and reduced $\overline{D}$ in the lesion. Upon follow-up imaging, a reduction in size of the hemorrhaging region, and at the same time, the increase in $\overline{D}$ and return to normal values was observed. The diffusion study in the initial exam (Figure 6a) shows a $\overline{D}$ value of approximately 1.05 $x10^{-3}$ mm^2/s, where as in the follow-up exam 2 weeks later (Figure 6b), the $\overline{D}$ value increased to 1.80 $x10^{-3}$ mm^2/s. The $\overline{D}$ at the time of follow-up exam is almost normal compared to the surrounding normal tissue which has a $\overline{D}$ value of 1.95 $x10^{-3}$ mm^2/s.

Adult Cervical Spine Images

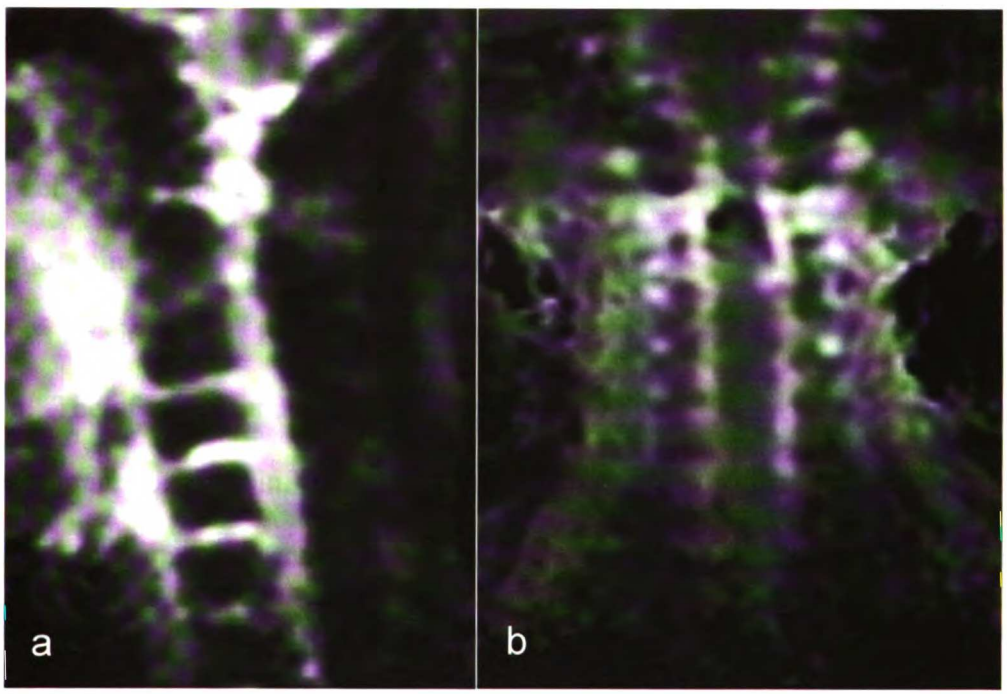

Figure 4.14. DTI-SSFSE images of the cervical spine.
Sagittal and oblique coronal cervical spine and disc $\overline{D}$ maps acquired using DTI-SSFSE method at 1.5T.

SSFSE-DTI images (Figure 4.14) clearly depict the cervical intervertebral discs (Fig. 4.14a) and the cervical spinal cord (Fig. 14b). The sensitivity of the coil restricted the length of the cord that can be visualized. The average $\overline{D}$ value in the spinal cord was

0.95 (x10^{-3} mm^2/s) with a standard deviation of .055 while the RA value was 0.31 with a standard deviation of 0.077. As for the discs, the $\overline{D}$ is 1.03 (x10^{-3} mm^2/s) with standard deviation of 0.16 and RA of 0.19 with standard deviation of 0.06. The values are summarized in Table 4.2.

	$\overline{D}$ (x10^{-3} mm^2/s)	Relative Anisotropy
Spinal Cord	0.954±0.116	0.314±0.154
Intervertebal Disc	1.035±0.329	0.194±0.126

Table 4.2. $\overline{D}$ and RA values from DTI-SSFSE for spinal cord and intervertebral disc.

Discussion

Water diffusion MR is becoming an imaging technique of increasing diagnostic importance [45-48]. Although single shot EPI diffusion imaging of the cerebral hemispheres has become a routine tool in clinical practice, diffusion imaging of the brain stem and spinal cord has lagged behind, owing to the marked distortion of these structures on single shot EPI sequences caused by the surrounding skull base and spinal column. Therefore, accurate diffusion quantitation has been clinically feasible primarily for the supratentorial brain, but not the brainstem or spinal cord. To deal with these problems, numerous alternative techniques have been explored including various navigated echo sequences [49, 50] and line scan diffusion sequences [51]. However, the acquisition and post-processing of navigated sequences often require complex algorithms, are difficult to use, and are not yet available in the clinical setting, while others such as line scan diffusion are too time consuming to be a part of routine clinical scans. The DTI-SSFSE, a single-shot method, is a compromise between the SNR efficiency and relative immunity to motion of the EPI sequence and the immunity to susceptibility artifacts provided by the slower line scan and segmented techniques.

The SSFSE images showed little distortion overall, did not require a fast receiver, and could be easily obtained with phased-array coils at both 1.5T and 3.0T. Due to the processing procedure of the diffusion images, the intensity weightings do not need to be manually corrected as the values will be divided by the T2-weighted b=0 image which also has the same weighting.

The DTI studies of the brain were conducted to prove the robustness of the sequence and the accuracy of the DTI computation. By moving to a spin-echo based acquisition sequence, the phase error problems prominent in EPI sequences can be addressed by the RF rephasing in spin echo sequences. Even though the SSFSE images had less SNR due to the longer echo train length compared to the EPI acquisition, the means and standard deviations of the measured values of $\overline{D}$ and RA were not significantly different. This verified the accuracy of the $\overline{D}$ and RA values determined using the DTI-SSFSE sequence. The $\overline{D}$ of the SSFSE even showed a smaller standard deviation than that of the EPI, which is presumably due to less spatial distortion and signal loss due to magnetic susceptibility effects. It is well established that diffusion anisotropy measurements are biased towards larger values by noise as described by Bastin et al. [52] and Mukherjee et al. [53] , so the fact that the RA means of the DTI-EPI and DTI-SSFSE sequences did not differ indicates that the SNR of the SSFSE acquisitions was sufficient for accurate anisotropy measurements.

Prior studies have already noted the lower SNR in the SSFSE images compared to single shot EPI due to preparation pulses in SSFSE to maintain echo trajectory and the inherent T2 decay during the long echo train [54]. In this study, we addressed the low SNR problem by using custom-made phased array coils for brain and spine studies, yielding higher resolution and/or faster acquisition times. It already has been demonstrated that this coil is capable of achieving up to an 8-fold SNR increase over the standard clinical quadrature head coil and a 4-fold gain over the region of interest [55]. The additional benefit of the phased array coils is that they require only the standard receiver available on all clinical MR scanners, whereas EPI-based DTI sequences typically require higher bandwidth receivers. Recently, developments in SSFSE sequence design promise further improvement of the SNR [38] . Coupled with the phased array coil, higher image quality and faster imaging times are expected.

The sagittal neonatal images provided in this study demonstrate the ability to assess regions where the traditional EPI sequence fails due to the high magnetic susceptibility problems. The brain stem region and cerebellum are undistorted in the DTI-SSFSE images and could provide information important for patient management. In the case shown in Figure 6, the bleeding in the cerebellum was clearly indicated by the diffusion data, but without spatial distortions. A second scan demonstrated the subsequent resorption of blood as indicated on the $\overline{D}$ map of the same patient 2 weeks later. The diffusion data has a distinct advantage over the traditional T1 and T2 images because it correlates directly with free water unlike the traditional images which are compounded by other factors. The decrease of $\overline{D}$ at the site of hemorrhage as shown by the DTI-SSFSE

images provides an assessment of tissue changes. The new prototype neonatal head coil [42] offers higher SNR than conventional head coil, therefore, enabling the use of DTI-SSFSE in this investigation.

A major difficulty in applying diffusion MR imaging to the cervical spine is the magnetic susceptibility distortions from tissue interfaces. The DTI-SSFSE sequence provides an advantage over the traditional EPI-DTI imaging in terms of reduced spatial distortion and compatibility with phased array coils. Prior studies have imaged the cervical region using relatively complex EPI acquisition sequences to minimize the artifacts. Those imaging sequences required a relatively long time, some exceeding 30 minutes to obtain just 4 slices and needed further offline processing for motion correction [56]. In comparison, the DTI-SSFSE imaging sequence was able to acquire 7 slices in 35 seconds for 1 excitation, and no motion correction was needed. The short imaging time also enables signal averaging to gain even higher SNR. In this study 4 excitations were typically used.

DTI-SSFSE showed clear benefits in diffusion imaging not only in the brain but also for the cervical spine with more accurate registration to high-resolution anatomical images. The $\overline{D}$ value reported for the spinal cord is the average $\overline{D}$ in the voxel. The value of approximately 1.0 x 10^{-3} mm^2/s is similar to $\overline{D}$ values reported by various other techniques [57-59] . In those studies, ADC values were reported separately along the anterior-posterior (AP) and superior-inferior (SI) directions to characterize diffusivity across and along the long axis of the cord, respectively. For comparison purposes, the $\overline{D}$

values from this investigation were compared to the average SI and twice the AP ADC values from the other studies. For the $\overline{D}$ of the intervertebral discs, the high variability is presumably caused by partial volume effects as the discs are relatively small as compared to the DTI resolution. Increased sensitivity and finer spatial resolution would be important to more accurately measure diffusion parameters in the vertebral discs. Disc diffusion parameters may be helpful in evaluating with conditions such as disc degeneration [59].

Future Directions

Besides enabling image co-registration, DTI-SSFSE may enable more accurate tractography of axonal tracts within the pons, medulla, cerebellum, and spinal cord. Tractography using DTI methods is becoming an important tool for evaluating the axonal pathways that are entering and leaving the cerebrum. For this study, although all scans acquired using the DTI-SSFSE sequence were capable of being used for tractography, the acquisition was not optimized for this purpose. These preliminary results are promising. However, additional development in acquisition and post-processing are required to determine whether these tracts can be demonstrated as they were by earlier line scan methods [60].

4.4 Clinical Premature Neonatal Brainstem and Cerebellum Study

Abstract

In this study, we investigated the use of a single-shot fast spin-echo (SSFSE) based sequence to perform diffusion tensor imaging with minimal distortions in brainstem

region of premature neonates, for the first time. Traditionally, MR diffusion tensor images have been acquired by echo-planar imaging (EPI) methods, in which large distortions result from magnetic susceptibility effects especially near air-tissue interfaces. These distortions hinder the accurate quantitation of diffusion parameters in the anterior and inferior portions of the brain and lower brain structures such as the brainstem. Due to RF rephasing in the transverse plane in the fast spin-echo method, the distortion in SSFSE is usually minimal. The goal of this study was to apply SSFSE diffusion MRI to quantify diffusivity in the preterm brainstem and to assess maturational changes for these values in premature infants with no evidence of brain injury over the range of 27-40 weeks estimated gestational age. The various regions of the brainstem showed significantly different maturation. Those patients with white matter injuries did not show significant diffusion differences in the brainstem regions in the population studied.

Introduction

Diffusion weighted magnetic resonance imaging (DWI) has been increasingly useful in clinical diagnoses of accurate conditions in which conventional imaging methods yield inconclusive results. DWI provides the clinicians with a different image contrast resulting from water diffusion changes, which sometimes precedes morphologic changes on conventional anatomic MRI [61, 62]. More recently, diffusion tensor imaging (DTI) has become widely used to provide additional information regarding the specific component of water diffusion in the orthogonal directions [46, 63]. Together with currently developing Magnetic Resonance Spectroscopy (MRS) methods, more information regarding the tissue in question can sometimes be revealed before drastic

anatomical changes. In diffusion studies, the rotationally averaged apparent diffusion coefficient (Dav) and the fractional anisotropy (FA) maps are two main analyses. The Dav parameter measures the mobility of free water, whereas the RA map is an inferred measurement about the organization of tissue. For example, water diffusion is restricted across the diameter of the axon due to the lipid bilayer of myelin sheath whereas along the axon, the water can more freely diffuse. Therefore this results in a higher value for the FA values and reveals the direction and approximate thickness of the white matter tracts.

Traditionally, MR diffusion tensor images have been acquired by echo-planar imaging (EPI) methods, in which large distortions result from magnetic susceptibility effects especially near air-tissue interfaces. The distortions are noticeable, especially in anterior and inferior portions of the brain and lower brain structures such as the brainstem. In this study, we investigated the use of a single-shot fast spin-echo (SSFSE) based sequence to perform diffusion tensor imaging with minimal distortions in brainstem region of premature neonates. Due to RF rephasing in the transverse plane in the fast spin-echo method, the distortion in SSFSE is minimal. This allows for the acquisition of diffusion parameters from brainstem regions in premature neonates which have not previously been reported.

The purpose of this study was to investigate diffusion tensor imaging of the brainstem using a single shot fast spin echo (SSFSE) sequence at 1.5T in order to provide normative diffusion values in premature infants.

Methods

20 premature newborns were studied at 27-40 weeks of gestational age on a 1.5T Signa EchoSpeed System (GE Medical System, Milwaukee, WI) using an specialized MR compatible isolette and neonatal head coil [42]. Eight patients had serial exams two weeks following the initial one; therefore a total of 28 exams were done. A series of standard MR scans were performed for clinical assessment of the neonatal patient. They include 1) T1 weighted sagittal spin-echo images with TR/TE of 500/11, 4mm thickness, 1 excitation, 192x256 encoding matrix; 2) T2 weighted axial dual echo, spin-echo with TR of 3sec, TE of 60 and 120ms, 192x256 encoding matrix, 4mm thickness; 3) 3D coronal SPGR with TR/TE of 36ms/9ms, theta of 35°, 1.5mm thickness, and one excitation.

Two clinical pediatric neuroradiologists independently read the MR images of each patient and classified them by the following criterion established at UCSF previously [64]. Areas of T1 hyperintensity and T2 hypointensity were interpreted as foci of hemorrhage and were not included in the study. Newborns were classified as "normal" if there were no periventricular white matter abnormalities, "minimal WMI" if there were three or fewer areas of T1 signal abnormally measuring less than 2 mm, or "moderate WMI" if there were more than three areas of T1 signal abnormality or these areas measured more than 2 mm but less than 5% of the hemisphere. In order to determine the severity of the abnormalities, there areas were scored as normal 0, hyperintensity on T2

weighted images only as 1, or hyperintensity on T2 weighted images and hyperintensity on T1 weighted images as 2.

A tensor SSFSE sequence described previously was used to acquire minimally distorted diffusion tensor images in the brainstem and the cerebellum regions. The neonatal patients were acquired with a FOV of 18cm, thickness of 5mm, 128x128 FreqxPhase with 1 Phase FOV. For 9 slices and 4 NEX, the total imaging time is approximately 6 minutes. Then the images were re-sampled using a tri-linear interpolation algorithm to a FOV of 24cm with 256x256 in post-processing if adjustments were needed. The diffusion b value was 600 s/mm^2. An Dav- and a RA- map were generated from the eigenvalues of the tensor construction, where the values are defined as the following:

$$Dav = \frac{\lambda_1 + \lambda_2 + \lambda_3}{3} \text{ and } FA = \frac{1}{\sqrt{2}} \frac{\sqrt{(\lambda_1 - \lambda_2)^2 + (\lambda_2 - \lambda_3)^2 + (\lambda_1 - \lambda_3)^2}}{\sqrt{\lambda_1^2 + \lambda_2^2 + \lambda_3^2}} \text{ [41].}$$

For analysis, tens regions of interest (ROI) were drawn bilaterally using custom software in the following regions: peduncles, superior colliculi, inferior colliculi, hippocampus, ventral and dorsal pons, deep cerebellum, cerebellar cortex, ventral and dorsal medulla shown in Figure 4.15. The hippocampus ROI was used for comparison purposes with the standard clinical EPI based diffusion acquisition. This region was chosen because it has minimal spatial distortion.

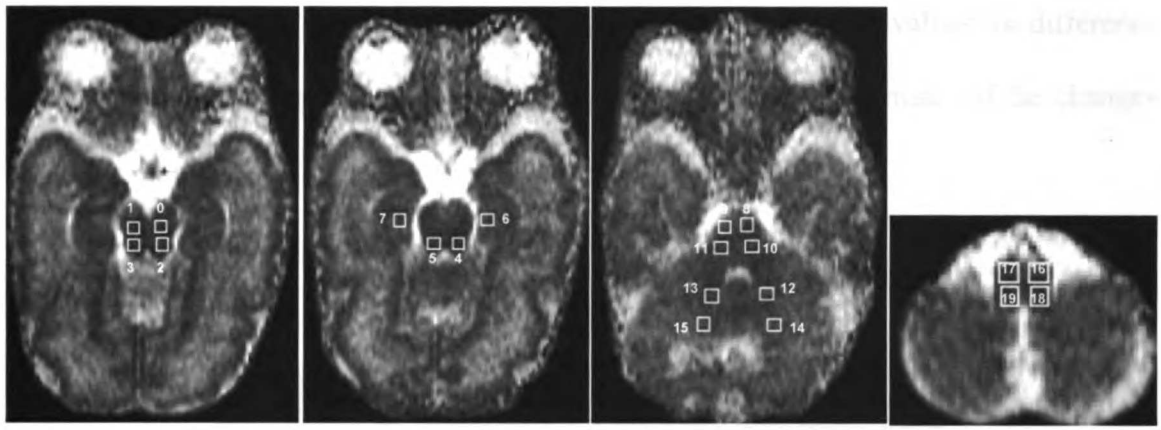

0,1 – cerebral peduncles
2,3 – superior colliculi
4,5 – inferior colliculi
6,7 – hippocampus
8,9 – ventral pons
10,11 – dorsal pons
12,13 – deep cerebellum
14,15 – cerebellar cortex
16,17 – ventral medulla
18,19 – dorsal medulla

Figure 4.15. ROI placement for analysis.

Statistical Methods

Mixed random-effects models were employed to assess the differences of the diffusion parameter between left and right sides of regions, between the ten different regions, and between the PVL scores. The statistical analyses were performed with control for the fixed effect of age at scan. The identification of patients was used as the random effect to control for multiple measurements from the same child.

In the mixed effects model analyses, statistical significant differences between different structures of interests were examined. If there was a significant difference between structures, the least squares estimates of the means were used as well as their pair-wise differences between structures. P-values for pair-wise differences were corrected for multiple comparisons using Tukey-Kramer adjustment.

Determination of whether there were significant changes in the diffusion parameter of interest between two scans was performed. This analysis was restricted within each

region. The medians of changes per week and the corresponding p-values for difference from zero based on sign rank test for each region as the robust estimates of the changes were presented.

Results

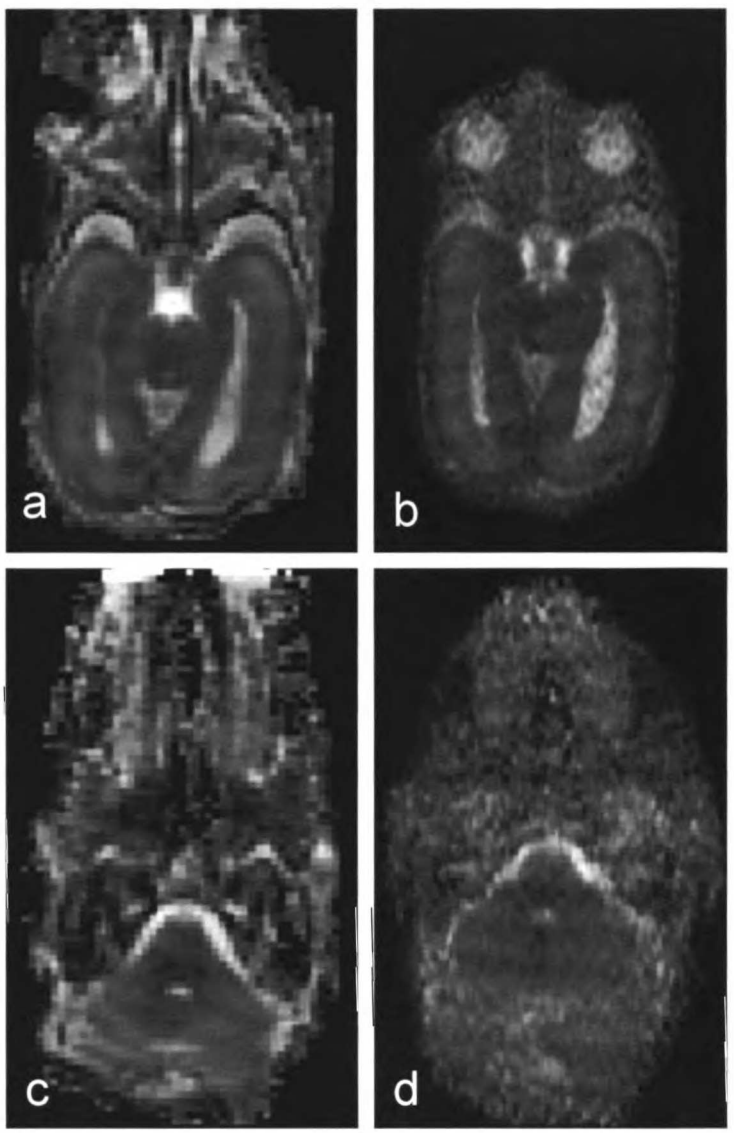

Figure 4.16. Diffusion maps of neonate acquired using EPI and SSFSE. Dav images obtained using EPI (a,c) and SSFSE (b,d) based diffusion method from a 30 week gestational age neonate. The cerebellum is severely distorted in the EPI acquisition whereas the SSFSE is lower in SNR but minimally distorted.

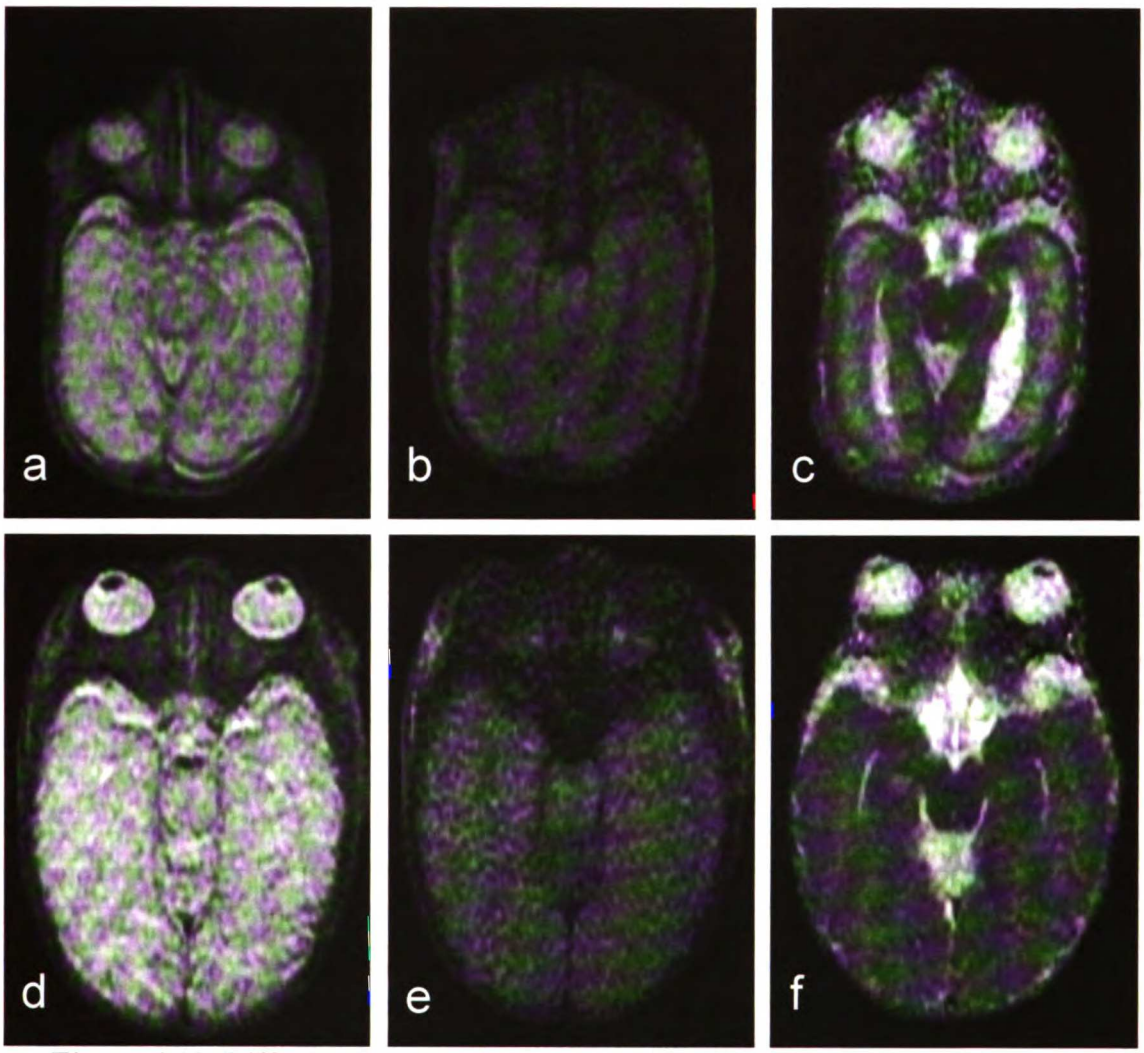

Figure 4.17. Diffusion images of neonates with various age.
(a, b, c) are images acquired from 30 week gestational age neonate; (d, e, f) are images obtained from a 40 week old neonate. (a, d) are b=0, (b, e) are b=600, (c, f) are Dav images.

The neonatal brain matures at a rapid rate, in which a few days of age make a substantial difference in shape, structure, and water diffusion parameters. Figure 4.17 demonstrates age related changes in the brain as it matures.

There was no statistically significant difference between the left and right of the regions based upon the mixed random-effects models ($p=0.90$). Therefore, the left and right values were summed to increase power for the rest of the statistical analyses.

Most regions were found to be significantly different from each other. The least squares means of Dav, the standard errors, the corresponding p-values for all regions were shown in the second row of Table 4.3. The table also lists the p values for pair-wise comparisons between different regions.

1	2	3	4	5	6	7	8	9	10
1186* 16.9**	1118 16.9	1127 16.7	1340 16.7	1298 16.7	1132 16.7	1259 16.7	1357 16.7	1350 17.7	1211 17.4
p-value	2	3	4	5	6	7	8	9	10
peduncles(1)	0.018	0.07	<.0001	<.0001	0.13	0.008	<.0001	<.0001	0.97
sup. coll.(2)		1	<.0001	<.0001	1	<.0001	<.0001	<.0001	0.0002
inf. coll.(3)			<.0001	<.0001	1	<.0001	<.0001	<.0001	0.001
hippo(4)				0.50	<.0001	0.001	1	1	<.0001
v. pons(5)					<.0001	0.56	0.07	0.23	0.0006
d. pons(6)						<.0001	<.0001	<.0001	0.003
deep cereb(7)							<.0001	0.0003	0.32
c cortex(8)								1	<.0001
v. med(9)									<.0001
d. med(10)									

Table 4.3. Statistical comparison of Dav between the various ROI's.
Dav, least squares means*, standard errors** and p-values of differences between structures demonstrating the differences in rate of maturation.

Dav did not correlate significantly with the age of the patients at the time of scan for most of the regions although it did indicate a trend of decrease with increasing age of the subject. Based upon the 13 serial exams, no significant change of the parameter with time for all regions was found.

Multiple comparisons based on mixed model show no significant differences between patients in the four PVL score groups (p=0.064). The least squares means and the standard errors are respectively 1244 and 17.8 (score=0), 1212 and 15.4 (score=1), 1211 and 21.4 (score=2), and 1278 and 31.9 (score=3).

The various regions were grouped into 3 groups except the peduncles and deep cerebellum regions, with dorsal pons, dorsal medulla, superior colliculli, inferior colliculi in the dorsal group; cerebral peduncles, ventral pons, and vental medulla in the ventral group; hippocampus and cerebellar cortex in the gray matter group. The three groups are found to be significantly different from each other as shown in Table 4.4. Furthermore, as a group, they varied significantly with patients' age at the time of scan ($P<0.0001$). Also, as expected they did not vary significantly with time in the available serial exams except the gray matter group; the p values are 0.41, 0.61, and 0.029 for dorsal, ventral, and gray matter group respectively.

Group		Least Squares Mean (Standard error)
Dorsal (1)		1145 (12.5)
Ventral (2)		1276 (13.4)
Gray Matter (3)		1348 (14.5)
p-value of difference between groups	1-2	<.0001
	1-3	<.0001
	2-3	<.0001

Table 4.4. Statistical analysis of Dav of regions by groups.
Least Squares Means, standard errors and p-values of differences between groups demonstrating the neurons in the sensory and motor mature at different rates.

The hippocampus Dav values obtained from the SSFSE and EPI based diffusion tensor sequences were statistically similar with a p-value of 0.61 using the paired student t-test. The FA values from the SSFSE method were not analyzed due to insufficient signal-to-noise ration (SNR).

Discussion

Water diffusion MRI is becoming an imaging technique of increasing diagnostic importance [45-48]. Although single-shot EPI diffusion imaging of the cerebral

hemispheres has become a routine tool in clinical practice, diffusion imaging of the brain stem and spinal cord has lagged behind, owing to the marked distortion of these structures on single shot EPI sequences caused by the surrounding skull base and spinal column. Many studies of the cerebrum utilizes registration and warping methods such as AIR [65]. However, due to the properties of Fourier imaging, the true values cannot be reconstructed without the changing the acquisition technique. Therefore, accurate diffusion quantitation has been clinically feasible primarily for the supratentorial brain, but not the brainstem or spinal cord. There are some case studies of brainstem regions using line scan diffusion, however these studies have been time consuming and have limited spatial coverage. [66] This study offers minimally distorted measures of the Dav for the various brainstem regions of neonates. By establishing a set of normative brainstem diffusion values for the neonates may prove useful in clinical diagnosis and treatment planning of these premature neonates.

By using the SSFSE method for diffusion acquisition, the SNR of the images are dramatically decreased due to the echo train length and T2 decay. However, with the aide of the neonatal birdcage head coil and the incubator, the SNR is still approximately similar to that of neonatal scans done with an adult head coil [42]. Therefore, the combination of the technique and customized coil allowed accurate quantitative measure of Dav in the brainstem and cerebellar regions to be obtained at the resolution demonstrating differences between the various regions.

As expected, most of the regions of the brainstem have different rate of maturation as shown by Table 1. When the regions were separated into three groups (dorsal, ventral, and gray matter), the groups also showed significantly different diffusivity values as demonstrated by Table 4.3. This analysis also demonstrated that the dorsal sensory pathway showed diffusivity changes earlier than for motor pathway (ventral neurons), which agrees with known maturation rates. [67]

Previous physiological and MRI studies have demonstrated the decrease of diffusion values of brain tissue over the course of neuronal development. [67, 68] Although Dav for individual regions did not show significant decrease over the age range of the subjects, it did demonstrate a negative trend. It is suspected that either the diffusion parameter of the ROIs did not vary dramatically at the ages near birth, or the number of subjects was insufficient in yielding a determinant result. Furthermore, due to the size of structures of interest, ROI placement was difficult as a few pixels with drastically change the analysis. This can be seen as the data points of the measurement varied a great deal even with subjects who had serial scans. Continued data collection will be conducted to determine changes of Dav with age with higher statistical power.

It is interesting to note that in the cerebellum, the deep cerebellum developed earlier than the cortical regions of the cerebellum [69], which similar occurs in the cerebrum where the basal ganglia matures early and have lower diffusion values compared to other areas. This confirms the fact that deep grey nuclei mature earlier than the rest of the structures.

The eight serial exams did not demonstrate significant diffusivity changes which maybe due to various factors. Due to the small size of the regions of interest, very slight differences in ROI locations would yield different values. With increasing number of patient scans, we believe at some time of the future, the serial exams could yield further information. Also, the tissue organization changes may not happen over the short duration between the serial exams, which was approximately two weeks apart.

4.5 Summary

In this chapter, a new diffusion tensor MRI technique based on the SSFSE acquisition method was introduced. The sequence was designed, tested on phantoms and volunteers, and finally on patients. It was demonstrated to have less artifact compared to the more traditional EPI diffusion method while providing similar diffusion parameter measurements in the regions of interest. Although some SNR and time were traded to remain minimally distorted, in clinical diagnosis, it is more important to obtain an accurate assessment of the patient condition. It is foreseeable that the SSFSE-DTI will be increasingly utilized in more clinical studies of regions where magnetic susceptibility artifact is the limiting factor.

5 Spectroscopy

The prior section introduced diffusion to detect micro-structure changes, MR spectroscopy, on the other hand, is capable of detecting metabolic changes of the cells. Usually, the onset of disease will cause the metabolism to change in cells before the full blown changes in structure are detectable. In the following section, MR spectroscopy is briefly explained through the physics, the metabolites of interest, and new techniques in improving the acquisition of spectroscopic data.

5.1 Chemical Shift

MR Spectroscopic imaging uses the property of chemical shift to detect biologically important compounds in vivo. In all molecules, atoms are surrounded by electron clouds, which are not evenly distributed due to the stronger or weaker attraction of the nuclear specie. For example, in the oxygen-hydrogen bonds of the water, the electron cloud is closer to the oxygen than the hydrogen due to fact that oxygen has a higher electronegativity. The electron cloud will interact with the external magnetic field, therefore, shielding the nucleus from the external field. This causes a change in the local magnetic environment, in which the nuclei experiences a slight different magnetic field $B = B_o(1-\sigma)$, where σ is the chemical shielding. As noted before, the resonant frequency of the nucleus is determined by the magnetic field that it is experiencing; therefore, the frequency of the specie is given by $\omega = \gamma B_o(1-\sigma)$. Due to the fact that Larmor frequency of the nucleus changes based upon the strength of the external field, the more commonly used term for chemical shift is referenced and expressed in parts per million (ppm) units away from the reference frequency, given by $\delta = (\omega - \omega_{ref})/\omega_{ref}$.

[70] This difference in frequency allows the measurement of various metabolites in the tissue to infer about the condition of that tissue.

5.2 Brain Metabolites

There are numerous metabolites that can be studied by proton MRSI in vivo, however, due to the limited field strength of the clinical scanners and physical properties of the metabolites, a limited number of metabolites have enough concentration, therefore enough SNR to be acquired and studied at the desired TE. They have been extensively studied and the primary compounds are briefly described below. [71-74] This dissertation has concentrated efforts in studying the brain, therefore, metabolites of interest in the brain are solely represented.

5.2.1 Choline Compounds

Choline has nine equivalent methyl protons visible at 3.2ppm. It has several metabolic functions, which include precursor for phosphatidylcholine, phospholipids sphingomyelin, and acetylcholine synthesis and a methyl group donator. Phosphatidylcholine and sphingomyelin are structural components for cell membranes. These phospholipids are also precursors for intracellular messengers such as ceramide and diacylglycerol. The proliferation of choline can be related to growth of cells or the breakdown of cell membranes. An example is that in cancer patients, the choline peak is abnormally high compared to other metabolite peaks. But it is interesting to note that in neonates, a high level of choline can be seen in the MRSI exam due to the fact that their brains are still rapidly maturing and the cells are dividing and growing, which have similar effects as the cancer cells. [75]

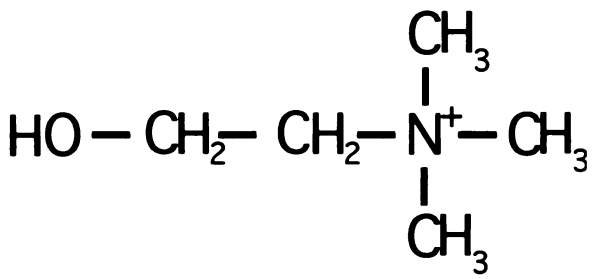

5.2.2 Creatine Compounds

Creatine is a non-protein amino acid synthesized in the kidney, liver and pancreas. Creatine and phosphocreatine (PCr) compounds play an important role in the energy pathway of the cells [76]. The phosphorylation and de-phosphorylation of these compounds occurs when energy is being stored or used through the conversion of ADP to ATP or vice versa. The energy is stored or released by the formation or break-up of high energy phosphate bonds. The most observed peak is at 3.02ppm of the CH3 group due to the fact that the separation between the peaks is smaller than the in vivo linewidth. With good water suppression and higher field strength, the CH2 group can be seen at 3.94ppm.

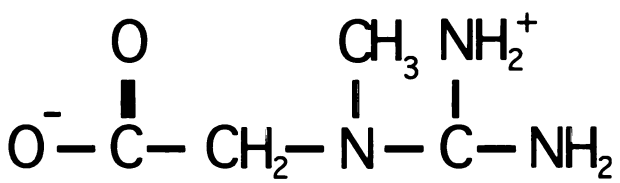

5.2.3 N-Acetyl Aspartate

NAA, while its function remains poorly defined, it is an indicator for the status of neurons. It is observed at 2.02ppm. While its true functions remains illusive, several recent studies did find NAA being transported intercompartmentally in molecular water pumps in neurons and oligodendrocytes [77] and supplying acetyl groups for myelin lipd synthesis [78]. In cancer patients, NAA levels dramatically reduce; together with the

increase of choline level, studies have shown they can be used to detect cancer even before morphological changes. Again, it is worth to note that in neonates, NAA levels are low due to both the immaturity and low density of neuronal cells. Therefore, in analyzing brain spectra, one needs to be careful to note the age of the subject in order to determine whether NAA levels are in the normal range.

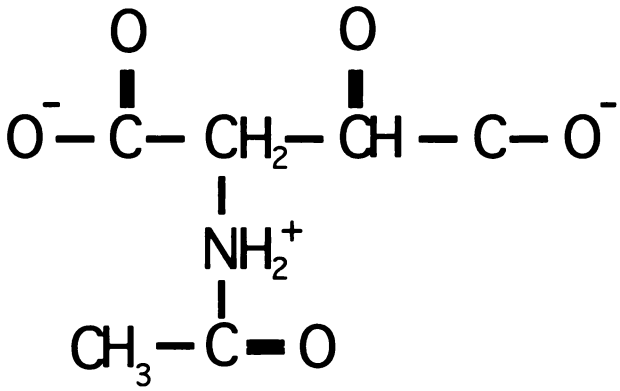

5.2.4 Lactate and Lipid

Lactate is a product of anaerobic respiration, which can be a result of rapidly growing cells outstripping the oxygen supply (cancer patients or neonates), mitochondrial dysfunction, or other conditions that reduced level oxygen was supplied to the brain (trauma patients) [79]. It is present at 1.33ppm as an inverted doublet at long TE of 140ms.

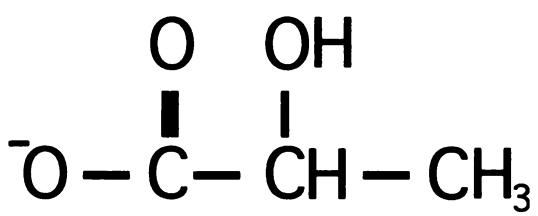

Normally, the brain does not have any free lipid that can be seen in MRSI. Many of the lipid peaks, which are in the same region as the lactate, are subcutaneous lipids folded in from the skin on the skull. The only time that lipids are observed in brain tissue is when

the cells die and cell structures breakdown [80]. The overlap of these two peak regions cause problems in accurately interpreting the spectra; therefore, editing method can be employed to "subtract" out the lactate peak [81], which will be discussed later.

5.3 Spectroscopy Acquisition Methods

There are two basic spectroscopy approaches. The single voxel spectroscopy method excites and measures one volume of tissue and the multi-voxel method generally excites a region in space and uses phase encoding to allow multiple arrays of spectra to be collected. In this discussion, the multi-voxel technique will be briefly described due to its advantage in spatial coverage and spatial resolution.

5.3.1 PRESS

Point resolved spectroscopy (PRESS) is one of the most common spectral acquisition methods, in which spatial localization occurs in three dimensions and spectra are then obtained by phase encoding the PRESS selection [82, 83].

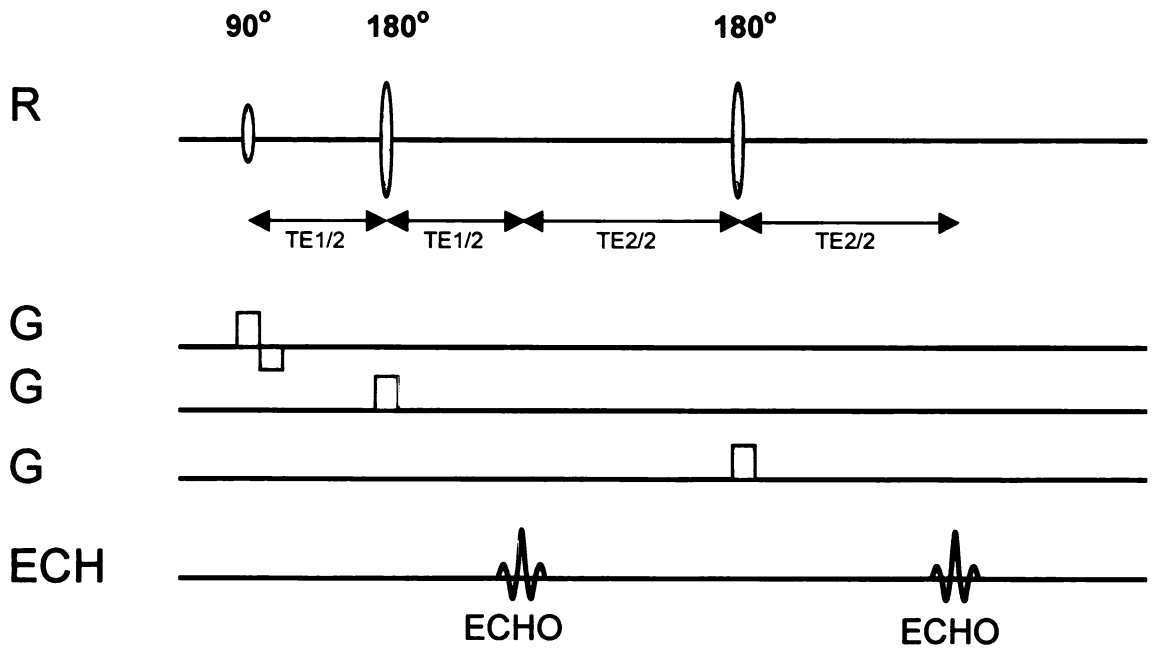

Figure 5.1. Pulse diagram for PRESS volume selection.
The intersection between the three spatial selective RF pulses is the PRESS box and only echo 2 is acquired.

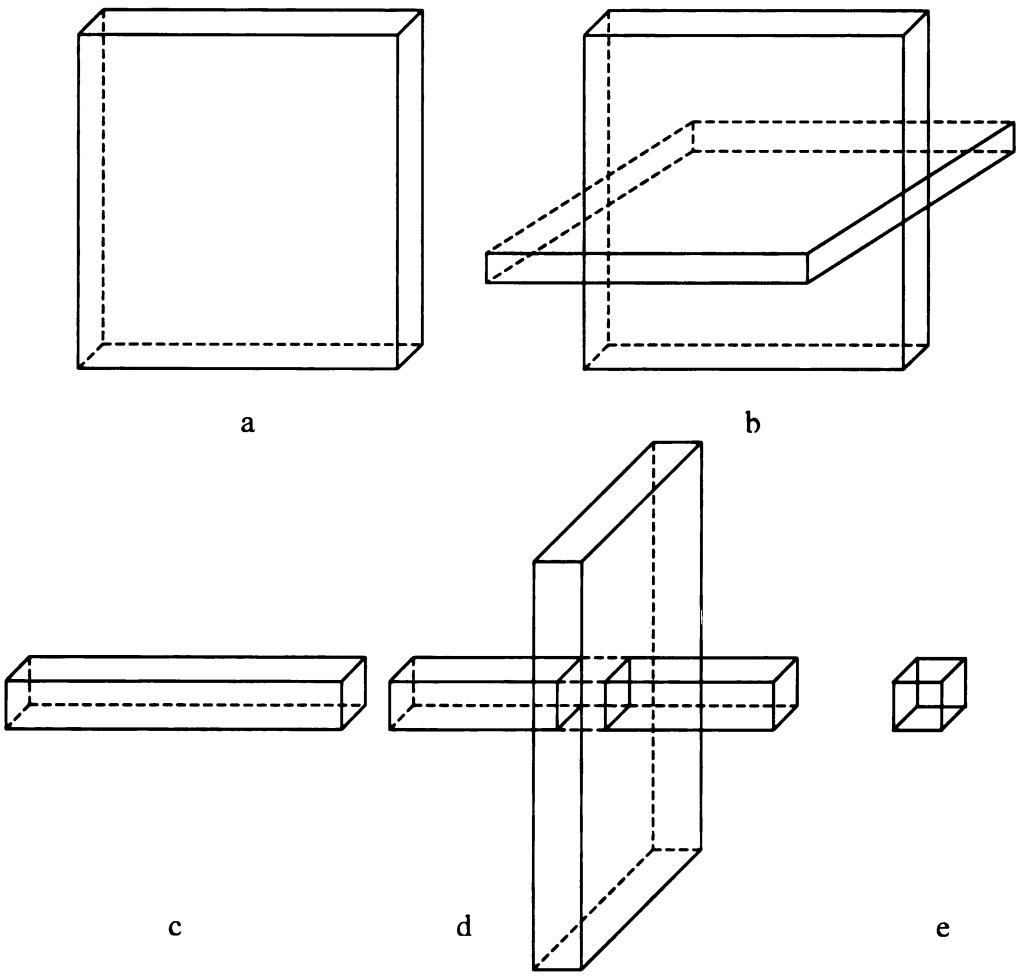

Figure 5.2. Volume selection using PRESS.
A slab is selected by 90 (a), the rectangular intersection of the 90 and 180 (b→c), final 180 intersecting with the previous volume (d), and the PRESS selected box (e).

As shown in the diagram, a slice is excited by the 90 pulse in the x-direction, and the FID is not sampled. An excitation of another slab by the 180 pulse in the y-direction at $TE_1/2$ will produce an echo; however, this echo will not be sampled. After the some time interval, the third excitation of 180 in the z-direction will complete the PRESS selection. Only the spins that are excited by all three pulses will produce an echo that will be

acquired. To maximize the signal, the $TE_1/2$ before the 1st 180 pulse is generally minimized and the TE_2 is adjusted to obtain the needed TE for the entire acquisition.

After the PRESS selection, each individual spectrum is obtained through phase encodes in all three dimension, which is also called 3D chemical shift imaging. The phase encoding method in 3D dictates the amount of time that is required for the experiment. The total imaging time would be $T_{imaging} = TR \cdot N_{acq} \cdot N_x \cdot N_y \cdot N_z$. The 3D although time consuming, it allows continuous spectra to be collected and offers some advantage over the 2D methods. One of such effect will be utilized in the later discussed experiment, in which Fourier properties of continuous acquisition in k-space allows "voxel shifting" to yield data in arbitrarily located regions.

5.3.2 STEAM, ISIS and Other methods

There are various other spectra collecting methods, which have been employed in MRS and have some disadvantages compared to PRESS.

The image selected in vivo spectroscopy (ISIS) technique uses subtraction method to determine the final selection volume [84]. The acquisition starts with a simple 90 slice selective acquisition arriving at the FID containing the entire volume. Then various 180 pulses are applied in front of the standard FID acquisition to yield a combination slice and out-of-volume signals. Through the combination of these signals, the final volume is selected. The following diagram demonstrates a slice selection in ISIS. The biggest disadvantage is that the subtraction error in the ISIS method is unavoidably large in 3D acquisitions and not used clinically.

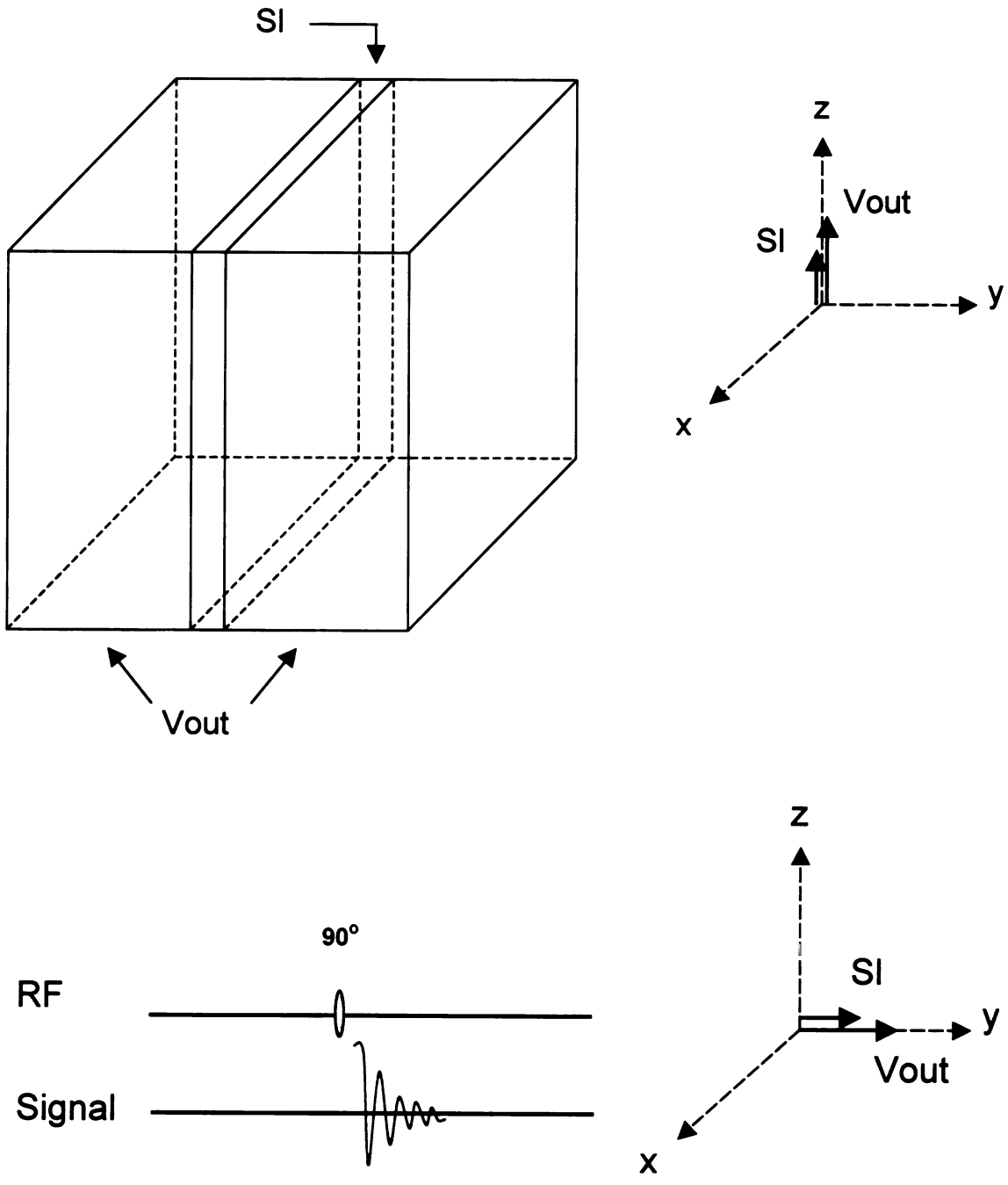

Measurement S1=Vout + SI

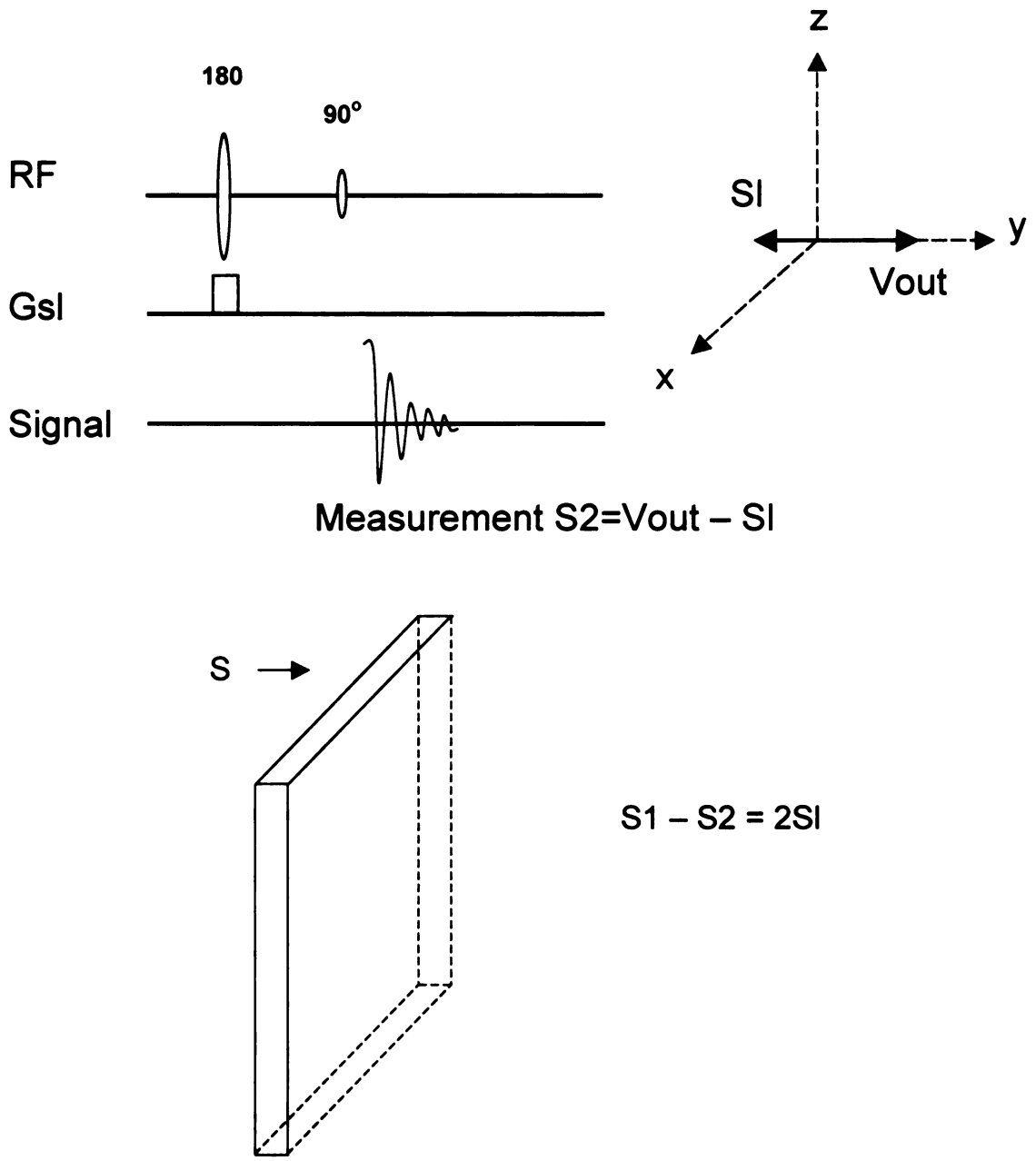

Figure 5.3. Volume selection using ISIS.
ISIS selection for one slice obtained from the subtraction of two acquisition of signals.

Stimulated echo acquisition (STEAM) [85] is a technique still utilized in certain specialized acquisitions. It is based on the same selection scheme as PRESS with the exception that the spatial selective RF pulses are all 90° pulses. There are multiple

echoes produced, but only the stimulated echo at the desired TE is optimized and sampled [86].

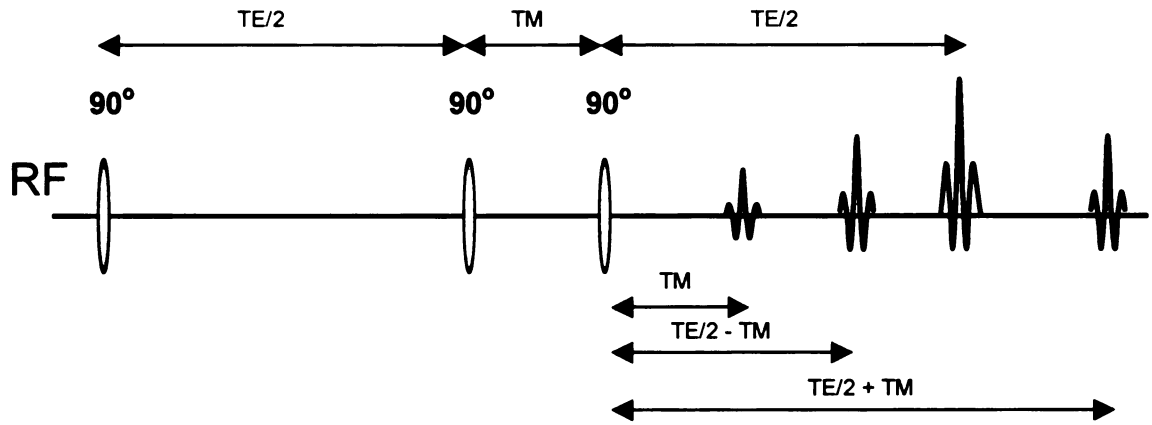

Figure 5.4. Pulse diagram for STEAM acquisition.
Multiple echoes are formed in this method, but the echo at TE/2 is the only one acquired and stored.

The largest advantage of STEAM over PRESS is that a shorter TE can be achieved with the 90° pulses, but at a cost of half of the SNR theoretically and also demonstrated in experiments [87, 88]. With the increasing investigation of utilizing higher fields, where the effective T2 of many of metabolites seem to be shorter, STEAM acquisition may again play an important role in the future.

5.3.3 Lactate Editing

Due to the overlapping resonances of lactate and lipid, editing techniques are required to fully assess the presence and quantity of lactate. The technique employed in one of the following studies uses the property of spin coupling to produce spectra that can be added and subtracted to yield lactate. [81]

Nuclear species share the electron clouds that have local "shielding" effects and thus change the behavior of the resonances. This is known as spin-spin or J coupling because

it happens between the spins of adjacent nuclei and is independent of external field strength.

Band selective inversion with gradient dephasing (BASING) uses two acquisition cycles per phase encode step to obtain lactate upright and inverted through the excitation of lactate's coupling partner at 4.1ppm. As demonstrated in the figure, in the first cycle, the coupling partner is in the passband and being excited leaving the lactate doublet at 1.33ppm inverted. In the second cycle, the pass band of the spectral excitation excludes the 4.1ppm partner, which causes the doublet to be upright. Through simple addition and subtraction, the spectra are combined to yield the various metabolite levels.

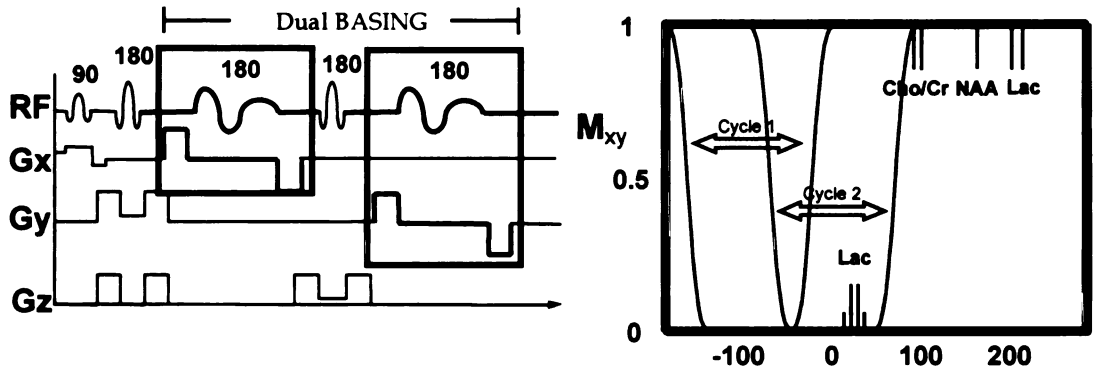

Figure 5.5. Pulse diagram for the dual BASING lactate editing scheme.
The J-coupling of lactate is exploited to produce accurate lactate measurements.

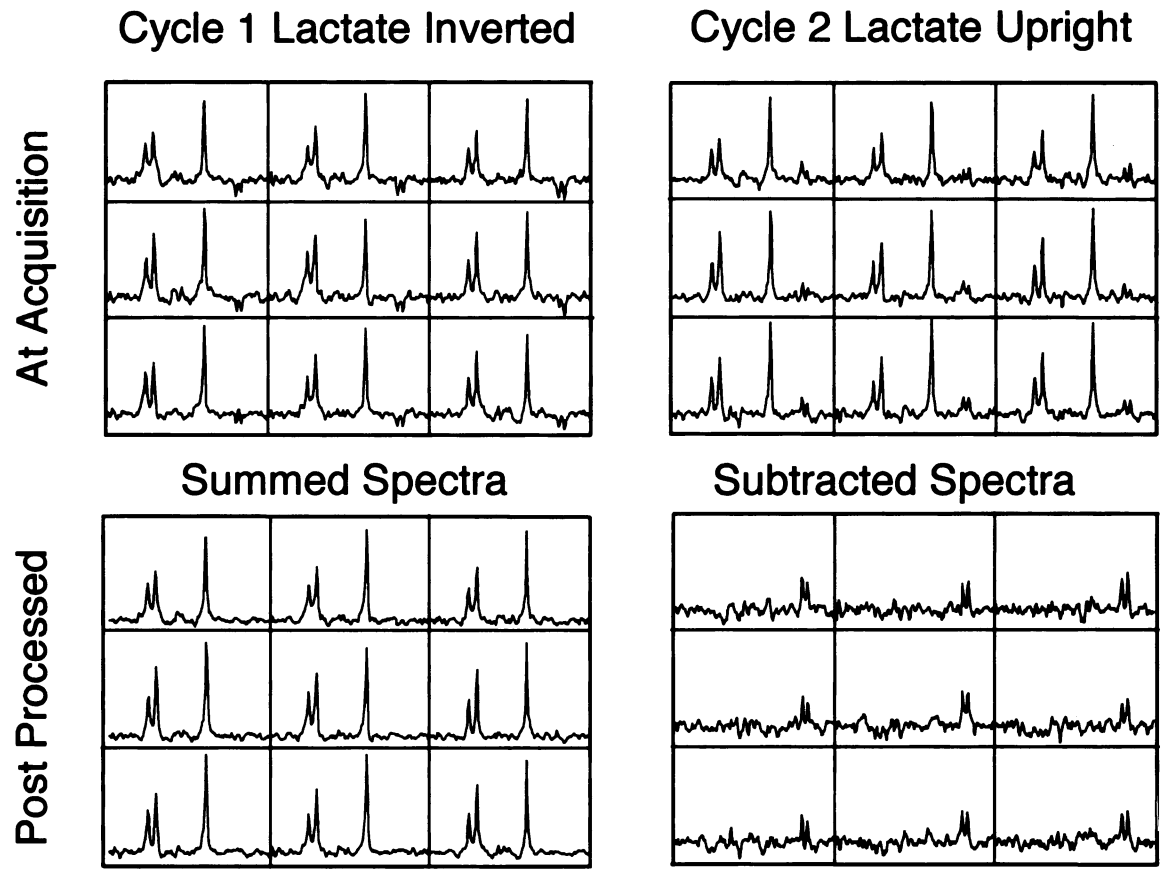

Figure 5.6. Lactate edited spectra.
Spectra acquired using the dual BASING scheme showing choline, creatine, NAA, and lactate in pre- and post-processing stages and demonstrates the sequence ability to produce clean lactate spectra with no lipid contamination.

5.4 Clinical Neonatal Spectroscopy in Birth Asphyxia Patients

Abstract

In term neonatal encephalopathy, increased brain lactate (LAC) levels and decreased N-acetylaspartate (NAA) levels, measured by proton MR spectroscopy in specific brain regions, are associated with adverse neurodevelopmental outcome. Lactate-edited 3D MRSI now allows the assessment of these metabolite levels throughout the newborn brain. In this study, new automated processing methods were developed to rapidly analyze the 1024 spectral arrays acquired in neonatal MRSI in order to better quantify the

presence and extent of abnormal metabolite levels. These methods were investigated in a preliminary study of term neonatal encephalopathy. The rapid post-processing methods allowed the analysis of all spectra in <0.5 hours and provided metabolite ratios for specific anatomic ROIs. In this study, LAC/NAA and LAC/choline (LAC/CHO) were increased and NAA/CHO decreased in widespread regions, in neonates with fatal outcome relative to those with normal neurodevelopmental outcome at 1 year of age.

Introduction

Recent studies have demonstrated the important diagnostic values provided by anatomic, diffusion, and spectroscopy MR imaging, especially in assessing neonates with injury [89-91]. It has long been determined that increased lactate level is directly related to birth asphyxia injuries and clinical outcome. The previous studies have typically applied single voxel MR spectroscopy (MRS) to provide in vivo lactate information in a small region. Technical difficulty of overlapping lactate and lipid peaks at 1.3ppm region further complicate the accurate determination of lactate levels. Although this is not an issue in the majority of the included patient cohort, however, the robustness of the spectral editing method increased the accuracy of lactate level assessment. In this study, a lactate editing method was employed together with 3D point-resolved spectroscopic imaging (PRESS-MRSI) to provide accurate measurements of metabolite levels throughout the neonatal brain [92]. Novel post-processing methods were developed to analyze the large volume of complex MRI/MRSI data with the goal of being minimally interactive, several orders of magnitude faster than manual methods, and less prone to human subjectivity.

Methods

Patients:

A total of 10 newborn patients were studied early after birth at a median post-partum age of 24 hours ± (range =24hrs-30.5hrs). The studies were performed in an MR compatible incubator with a specialized neonatal head coil to provide a temperature-controlled, well-monitored, safe environment and to improve image quality [42]. Motor outcome was assessed at 1 year of age using a neuromotor score (NMS) of 0-5 as previously defined [93]; cognitive outcome was measured using the mental development index (MDI) of the Bayley's Scales of Infant Development II. For this preliminary technical development study, we only included the newborns with normal neurological outcome (NMS=0; MDI>85) (N=4) and those who died in the neonatal period (N=6).

MRI/MRSI Acquisition:

A series of standard MR scans were performed for clinical assessment of the neonatal patient on 1.5 T GE Signa Echospeed scanner (GE Healthcare, Milwaukee, USA) that include 1) T1 weighted sagittal and axial spin-echo images with TR/TE of 500/11, 4mm thickness, 1 excitation, 192x256 encoding matrix; 2) T2 weighted axial dual echo, spin-echo with TR of 3sec, TE of 60 and 120ms, 192x256 encoding matrix, 4mm thickness. A multivoxel 3D MR spectroscopy scan was performed to obtain metabolite levels covering most of the brain using PRESS acquisition with the BASING lactate editing method [81, 92, 94]. The uniformity of the selected region was obtained by slightly overexcite the prescribed region and shaped with very selective saturation (VSS) pulses [95]. The

acquisition parameters are 144ms/1s TE/TR, 1cc, 8x8x8 array, and an acquisition time of 17 minutes.

Analysis Methods:

Seven regions of interest (ROI) were drawn on the T2 weighted images by an experienced pediatric neuroradiologist and then used to obtain metabolite levels in the MRS data. The graphical image viewer and ROI tools were custom developed using Interactive Data Language (IDL). The selected ROIs were basal ganglia (BG), thalamus (THAL), optic radiation (OR), calcarine gray matter (CGM), corticospinal tract (CST), posterior white matter (PWM), and frontal white matter (FWM).

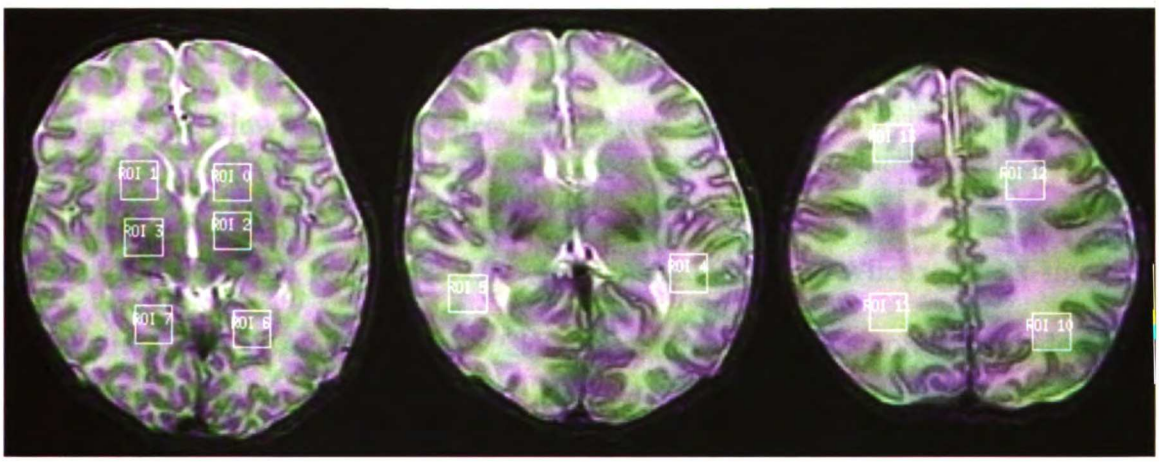

Figure 5.7. ROI locations for spectral analysis.
ROI locations drawn based on the T2 images that are analyzed in this study. 0,1-Basal Ganglia; 2,3-Thalamus; 4,5-Optic Radiation; 6,7-Calcarine Gray; 8,9-Corticospinal Tract; 10,11-Posterior White Matter

Custom software was developed to integrate and analyze the spectroscopy data according to a metabolite peak file. The reconstruction starts with an apodization of the k-space data and followed by a Fourier transform to produce the spectral arrays. Then, the spectra were corrected for phase and frequency variations. The resultant spectra are also

baseline corrected due to the incomplete water suppression [6, 96] and metabolite images were generated to depict the three-dimensional distribution of metabolite levels. An automated program was developed to zero-fill the MRSI data to 256x256 and select the center value corresponding to each ROI in the spatial domain. The program calculated the height of the metabolites in each ROI, and outputted the information into a comma delimited text file for automated statistical analysis.

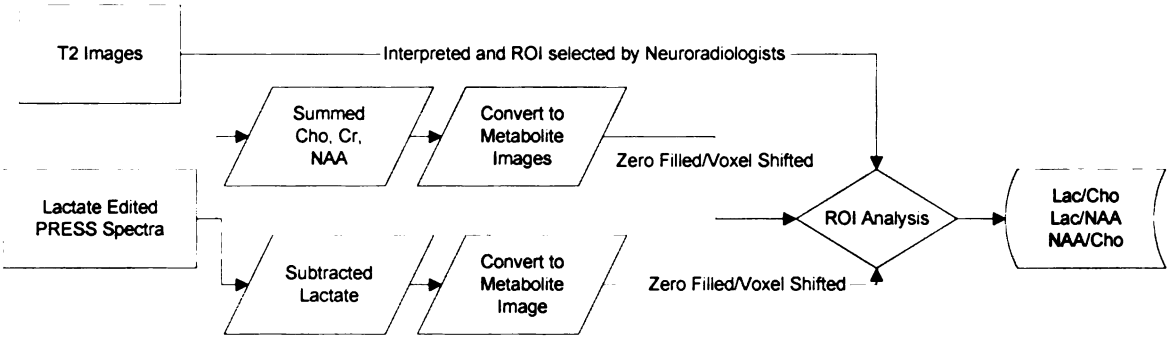

Figure 5.8. Flow chart of the processing steps.
A schematic of the automated spectral processing steps that requires minimal user interaction and large data throughput.

The left and right ROI for each region was compared using the Wilcoxon rank-sign test. Metabolite ratios (LAC/NAA, LAC/CHO, and NAA/CHO) of normal and deceased patients were compared in each ROI using Kruskal-Wallis rank-sign test in JMP (SAS, Cary, NC).

Results

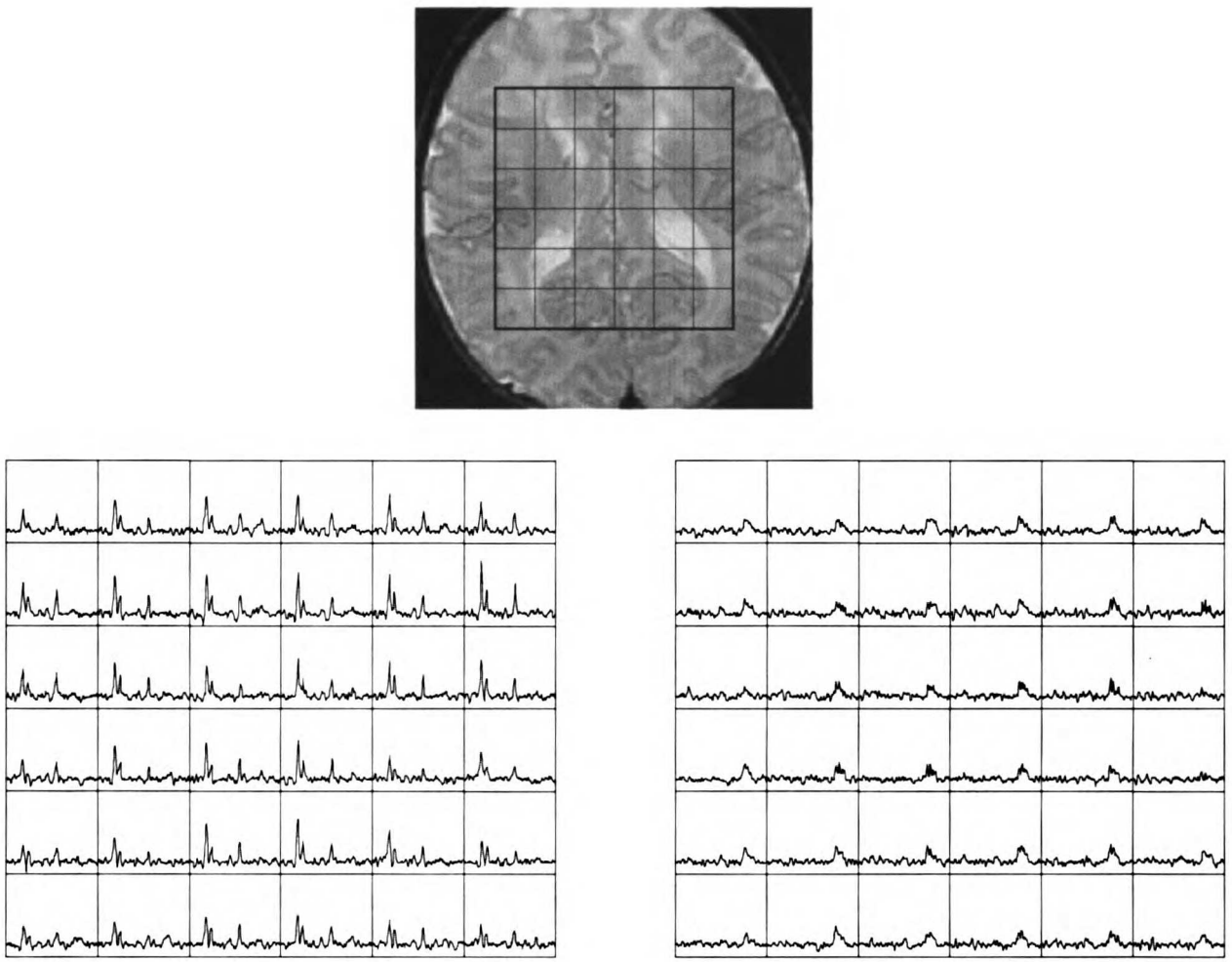

Figure 5.9. Array of spectra obtain from a neonate MRI/MRSI exam. A typical array of spectra obtained after post-processing showing choline, creatine, NAA on the left and lactate on the right. Note the large number of spectra in just this slice out of 4 slices covering the neonatal brain.

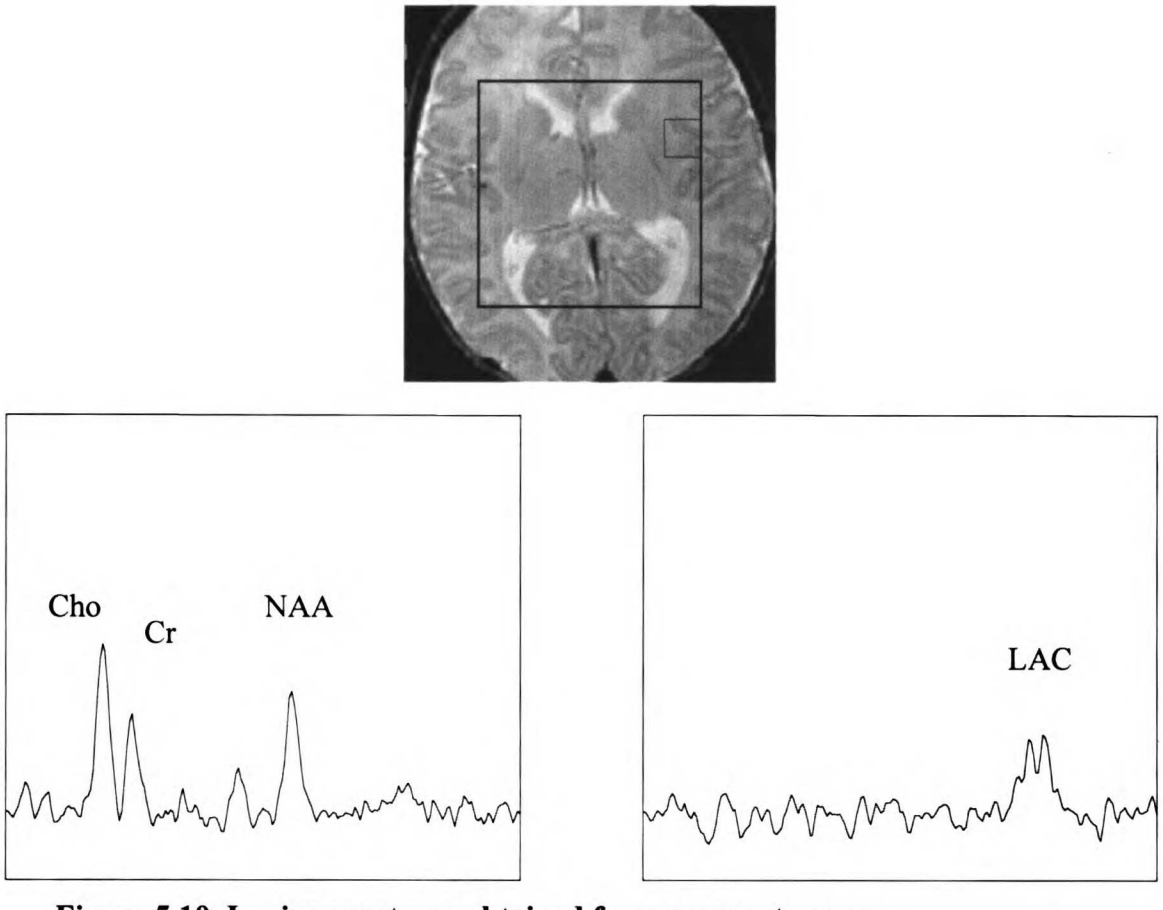

Figure 5.10. In vivo spectrum obtained from a neonate exam.
Zoomed in spectrum of one voxel showing choline, creatine, NAA on the left and lactate on the right. Note in neonates, the NAA level is much less than that of a mature adult and relative choline is also higher.

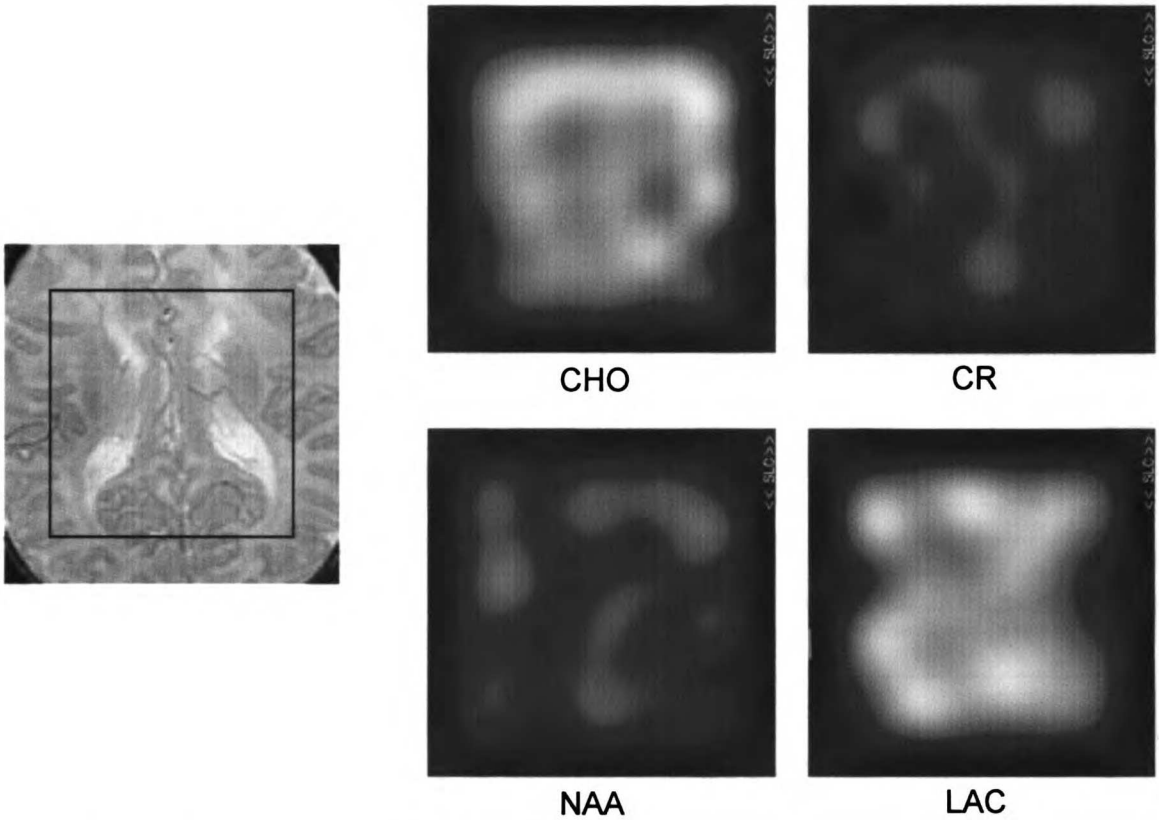

Figure 5.11. Metabolite maps.
After the initial spectral processing, metabolite peak heights are turned into images for quick, automated analysis of metabolite ratio in the listed ROIs.

The LAC/NAA, LAC/CHO were overall significantly higher in the deceased patient group compared to the NMS0 group, with $P<0.0001$. At the same time, the NAA/CHO for the NMS0 group is significantly higher with $P<0.0001$.

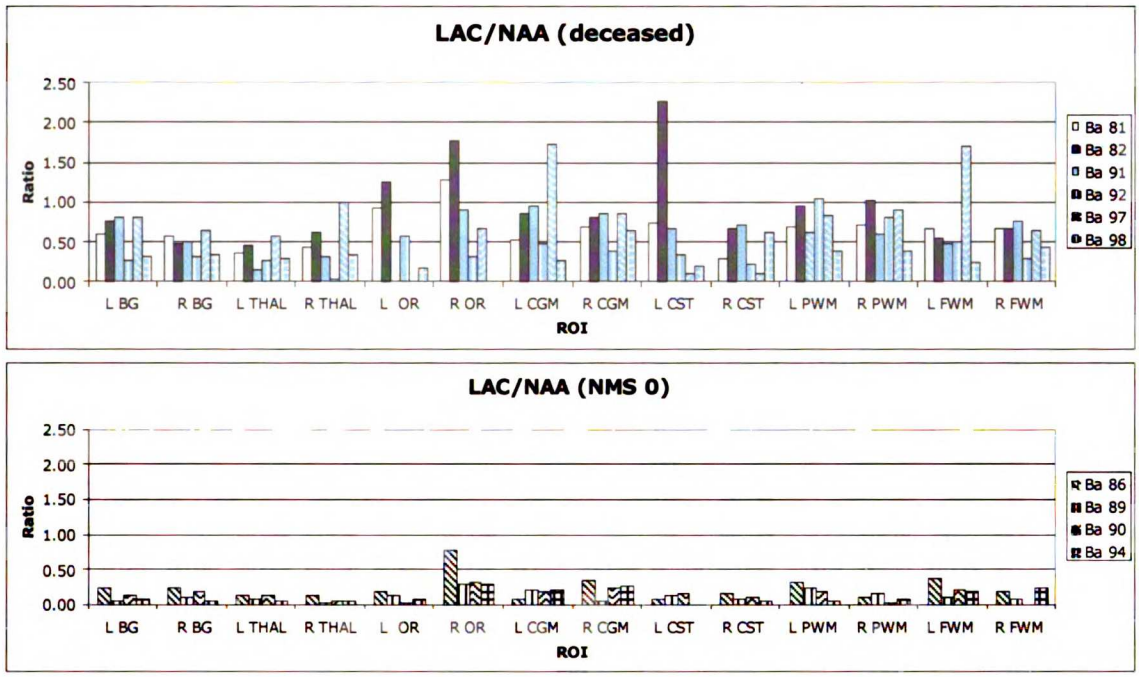

Figure 5.12. Lactate-NAA ratio comparison chart.
Lactate-NAA ratio comparison between the deceased and NMS0 patient groups. The deceased patients have significant higher LAC/NAA ratio.

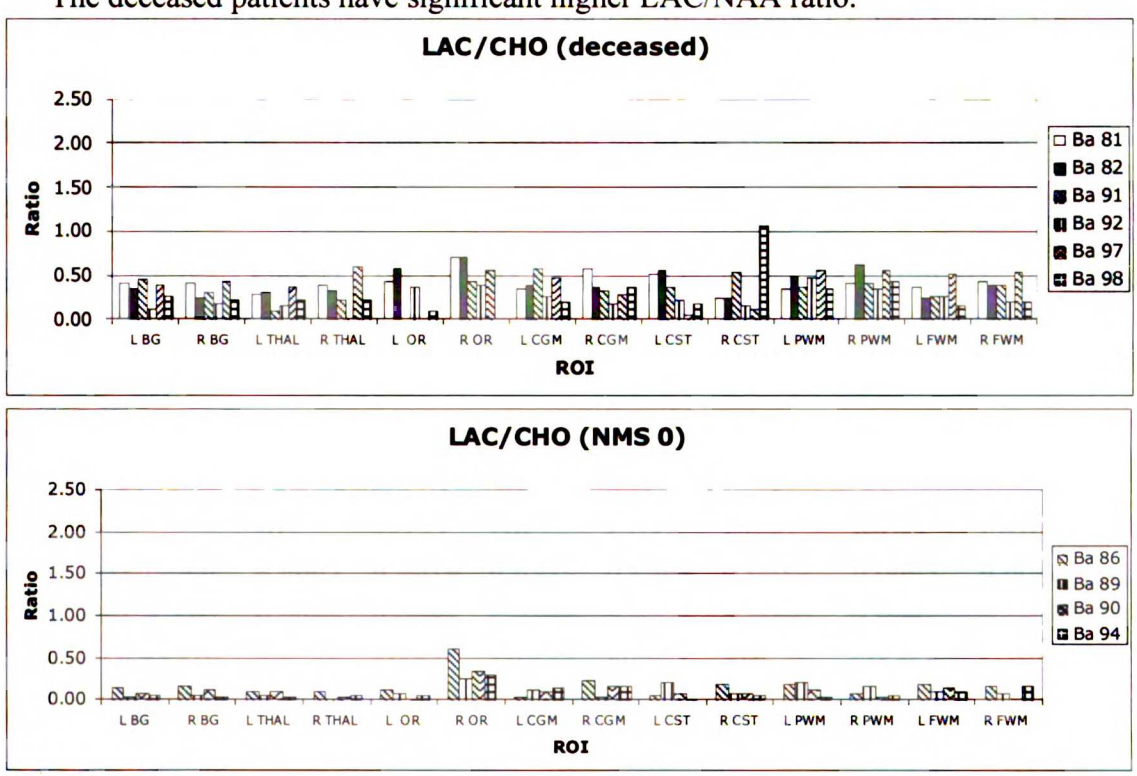

Figure 5.13. Lactate-Choline comparison chart.
Lactate-Choline comparison between the deceased and NMS0 patients. Again, the deceased patients had a significantly higher LAC/CHO ratio $P<0.05$.

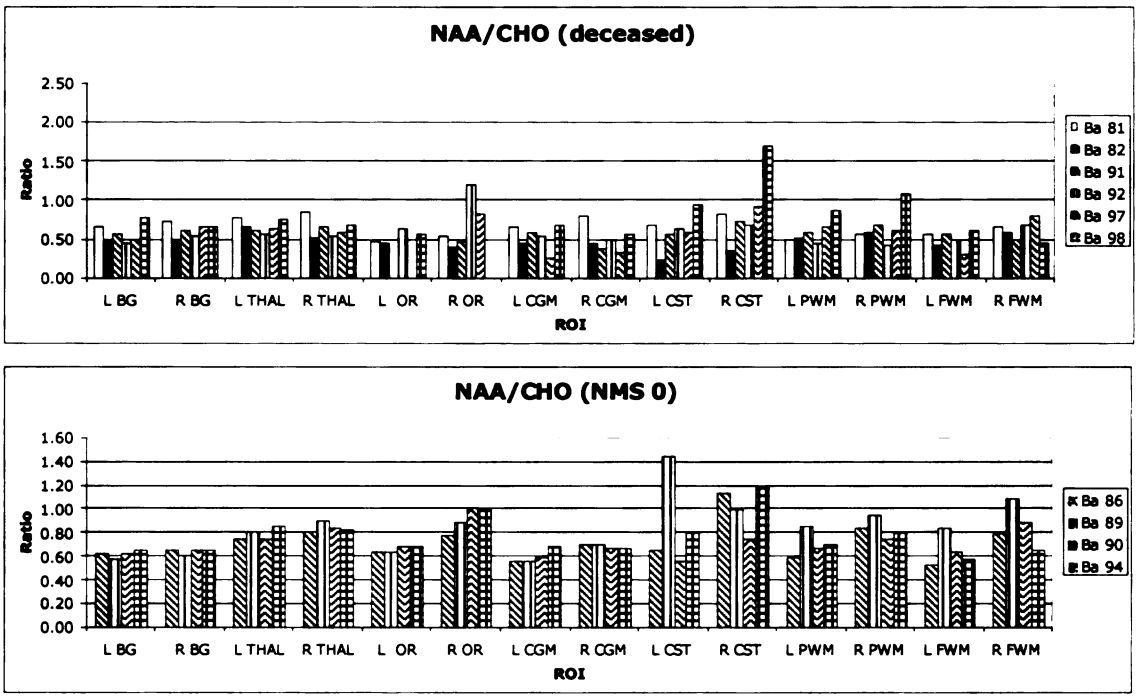

Figure 5.14. NAA-Choline ratio comparison.
NAA-Choline ratio comparison of deceased and NMS0 patients. Overall, the normative NSM0 patient group had a significantly higher NAA/CHO ratio. For specific ROI analysis, see the table.

In the analysis of the individual ROI regions, all of the regions had significantly higher LAC/NAA and LAC/CHO ratio in the deceased patients than the patients with NMS of zero. At the same time, the NAA/CHO ratios were higher in the NMS0 patients in most regions except BG, CGM, and CST regions compared to deceased patients. The corresponding P values are shown in Table 5.1, significant values are highlighted.

Table 5.1. DECEASED vs NMS0 comparison based on ROI

	BG	THAL	OR	CGM	CST	PWM	FWM
LAC/NAA	**0.0002**	**0.0018**	**0.0456**	**0.0003**	**0.0014**	**0.0002**	**0.0004**
LAC/CHO	**0.0004**	**0.0049**	**0.0184**	**0.0004**	**0.0048**	**0.0002**	**0.0008**
NAA/CHO	0.6713	**0.0049**	**0.0304**	0.0697	0.1535	**0.0491**	**0.0307**

Discussion

The use of MR spectroscopy has increasingly becoming an import diagnostic tool for evaluating neonates, providing various metabolite level changes corresponding with the

type of injury [97-99]. The use of MR compatible incubator and custom built MR coil enabled image and spectroscopy acquisition with relative high SNR, which allowed better quantitative measurements [42, 100]. This allowed relatively short scan time, in which most of the babies were not sedated. It also limited the need for repeat of problematic imaging series, which often occur when un-sedated patients move during the scan.

BASING, the lactate editing method allowed accurate quantitation of lactate without lipid contamination at 1.3ppm. Previously, many of the studies have been hampered by the inclusion of the lipid in the analysis [101]. In this study, two sets of spectra were generated—a spectra with only lactate, resulted from the subtraction of the acquisitions, and a spectra with NAA, CHO, and CR, obtained from the summation of the acquisitions. The resultant upright lactate peak spectra allowed easy interpretation of the data, in which the clinicians can quickly determine visually if abnormal amount of lactate existed and able to provide corresponding treatment quickly without the more intensive data processing. The more in-depth analysis of the metabolite ratios are used to provide more information and longer term treatment planning.

In this study, the automated processing scheme, which we developed, enabled large amount of data analysis with few human interactions with 0.5 hours. The peak height measurements were obtained using the already established methods published by Nelson [6, 96]. Further automated zero-filling and conversion to metabolite images, then alignment against the standard clinical T2 image enable the quick application of predetermined ROIs by neuroradiologists. Metabolite ratios were then automatically

obtained and easily analyzed using typical statistical programs. This method limited the subjective inputs by the users and applied the same analysis across all exams. The added benefit of the automated processing is that the analysis can be quickly applied to study other ROIs and using other metabolite quantitation methods.

As previously reported, significantly higher LAC levels were observed for all regions in the injured neonatal patients. Previously, most studies were done using the single voxel or 2D MRSI techniques, in which a limited number of regions were studied [102]. In this study, all of the regions had significant increase of lactate levels indicating that the asphyxia injuries occurred across the entire brain.

The findings in this study also support the hypothesis that an increase in lactate levels correlates with poor clinical outcome in birth perinatal asphyxia patients, as reported in various clinical reports [91, 103, 104]. NAA/CHO was lower in the deceased group in the THAL, OR, PWM, and FWM. In this preliminary study of term neonatal encephalopathy, the elevated lactate levels and lower NAA levels in deceased newborns relative to newborns with normal neurodevelopmental outcome, supports the validity of this approach, and suggests that metabolic abnormalities are widespread in severely affected newborns.

5.5 3.0T High Resolution Spectroscopy Technique Development

Introduction

In vivo proton magnetic resonance spectroscopic imaging (MRSI) has been used clinically to measure the metabolite levels in different tissues. Previous studies have

shown variations in metabolite concentrations associated with medical conditions. These studies have also noted that the fact that limited spatial and spectral resolution has hindered some of the in-depth analysis of the diseased state due to poor signal-to-noise ratio (SNR). With the FDA approval of 3 Tesla MR scanners, the doubling of SNR at the higher field strength has opened the door for more precise description of the anatomy, better metabolite characterization, and additional metabolite markers. The following work demonstrates 3D MRSI of adult brain as small 0.09cc resolution can be achieved using phased array coils at this higher field strength. Also, the use of low peak power, dual band spectral spatial pulses were investigated for their application to 3T MRSI of the brain using PA coils and body coil excitation.

Previous studies have shown that gray and white matter in the brain is metabolically different [105]. It has been shown that NAA and Cr have a higher concentration in the gray matter whereas Cho concentrations did not differ significantly [106-108]. The variability cited in the literature in the metabolite concentrations can be attributed to the partial volume of heterogeneous tissues. At 3T with PA coils, the partial volume effects can be greatly reduced and the characterization of the metabolite levels can be more accurately assessed. Previous studies have demonstrated a resolution of less than 5mm on a side of voxel was necessary to distinguish the gray and white matter of the brain [105]. This can be optimally achieved with surface PA coils with high SNR and high sensitivity at higher field [14]. However, due to the need to assess larger brain regions, the 8 channel PA head coil is able to provide increased SNR and larger coverage of the brain.

Method

8 Channel PA head coil and Quadrature head coil

A total of 6 normal volunteers aged 24-29 were imaged using a GE 3T Excite System. All the subjects had no known illness and normal appearing MR exams. Written consent was obtained from all volunteers approved by the Committee on Human Research at UCSF.

A 3 plane localizer were done, followed by standard T1 SPGR (TE minimal, TR 27 ms, flip angle of 40) for image and localization for 3D MRSI. For 8 channel head coil imaging, another 3D T1 inversion recovery fast SPGR (TE minimal, TR 7ms, TI 400ms, flip angle of 15) was done for better gray and white matter contrast. The 3D MRSI data were acquired in 9.5 minutes using a custom PRESS sequence with a TR=1.1s, TE=144ms, 1024 points, 2000 Hz bandwidth, 12x12x8 phase encoding, 1cc spatial resolution, and elliptical k-space sampling.

Due to body coil excitation when using the 8 channel head coil, the peak amplitude of the pulse was constrained to 20 uT. Dual band spectral spatial (SS) [109] pulses with decreased peak power and specific absorption rate (SAR) were specially designed for spatial selection and water/lipid suppression. The spectral passband was designed to encompass metabolites from choline to lactate, with a 288Hz passband (full width at 95% of maximum) and 66Hz transition regions. Each sub-pulse was 740 us in duration, giving 9.73 kHz bandwidth in the spatial dimension. (See Fig. 5.15)

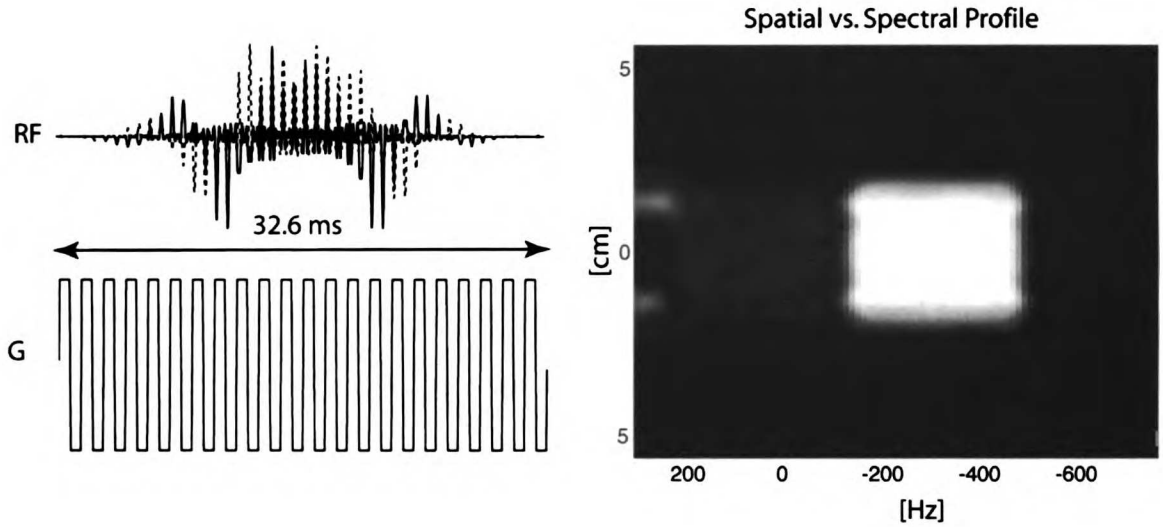

Figure 5.15. Custom designed spectral-spatial RF pulse.
Custom designed low peak power, low SAR dualband spectral-spatial pulse for brain spectroscopy. Image on the right demonstrates the relatively sharp edges of the PRESS selection.

Surface PA coil

A total of ten examinations were performed on ten normal volunteers ranging from the age of 25 to 42. All the subjects have no known illness and normal appearing MR exams. Written consent was obtained from all volunteers approved by the Committee on Human Research at UCSF.

High resolution T1 weighted 3D SPGR images were first obtained with the phased-array coils and image-intensity corrected for the inhomogeneous reception profile of the coils. An edge-filled lowpass filter was used. The 3D MRSI data was acquired in 17 minutes using a custom PRESS-MRSI sequence with a TR=2s, TE=40ms, 1024 pts, 2000Hz bandwidth, CHESS water suppression, 8x8x8 phase encoding with spatial resolutions as fine as $0.09cm^3$. High bandwidth, very selective saturation pulses were employed to

sharpen the volume selection profile and to reduce chemical shift misregistration effects. The signals from the different phased-array coil elements were combined using sum of squares method. The data presented below was processed with a 3Hz Lorentzian apodization and with baseline correction.

For peak characterization, the peak at 2.0ppm was labeled as N-acetyl aspartate (NAA), 3.0ppm as Creatine (Cr), 3.2ppm as Choline containing compounds (Cho). The contributions from other metabolites at those regions were deemed insignificant or inconsistent in the processing.

Results

The initial results of using the low power spectral-spatial pulses for long TE brain spectroscopy with 8 channel head coil and body coil RF excitation have proven to be feasible as demonstrated in Figure 5.16. The pulses offered excellent water and lipid suppression. There was no visible lipid contamination within the large array of MRSI acquired with long TE, offering spectra with a clean baseline.

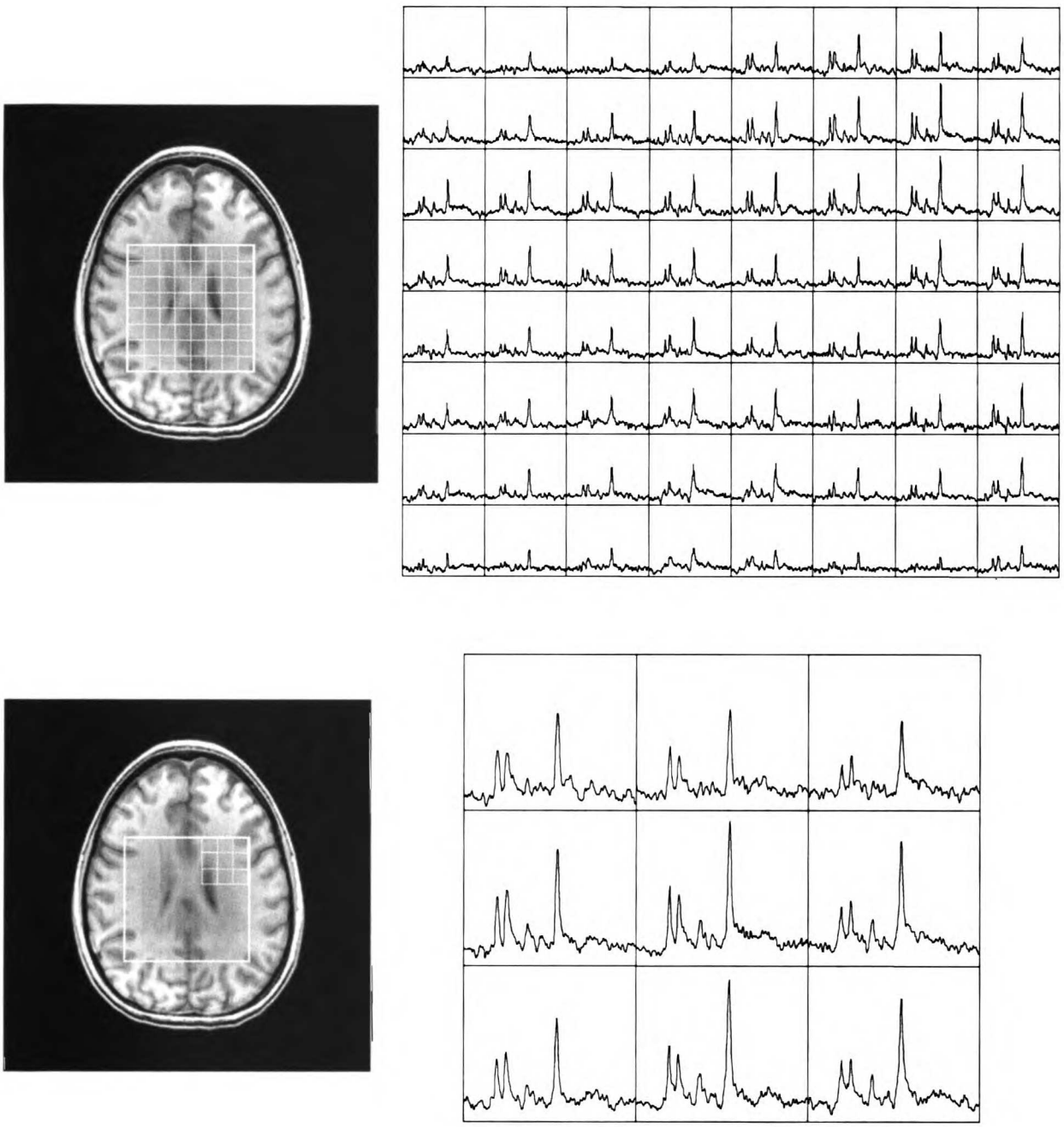

Figure 5.16. 1cc MRSI data.
1cc data from channel b (upper right corner). TE 144ms, TR 1sec, lower power spectral-spatial RF.

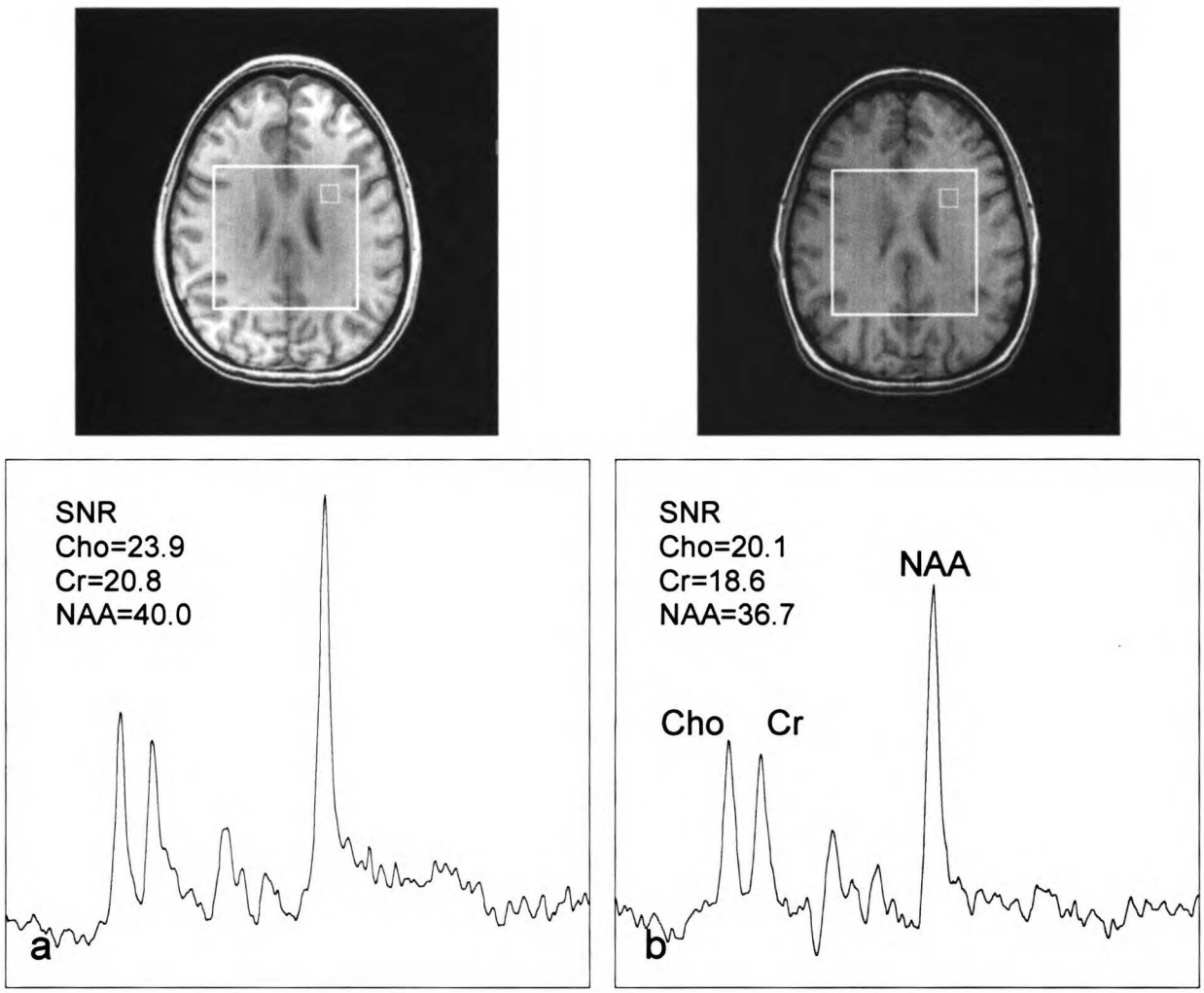

Figure 5.16b. SNR comparison between 8 channel and birdcage head coil. The 8-channel phased array coil has higher SNR while providing similar peak profile.

By using the 8 channel PA coil, even at a spatial resolution of 0.34cc (7mm sides), short TE spectra proved to be feasible. Cho, Cr, and NAA are clearly delineated and with excellent peak profile as demonstrated in Figure 5.17. Also, due to the short TE, additional metabolites such as myo-inositol (mI), glutamate and glutamine (Glx) can be detected and may be useful in assessment of various clinical conditions [110, 111].

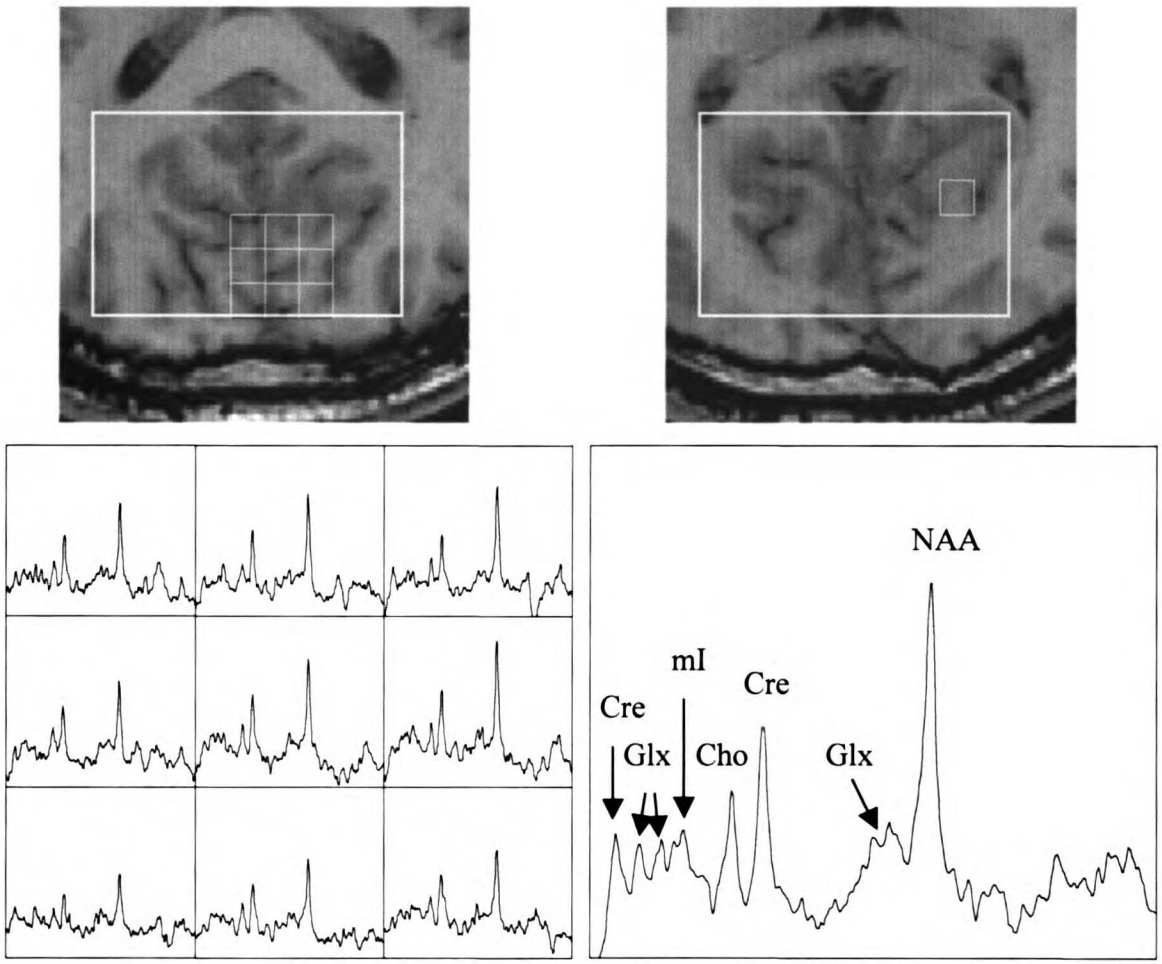

Figure 5.17. Short TE spectra.
Short TE 0.34cc spectra acquired using 8-channel phased array head coil with CHESS water suppression showing additional peaks can be acquired and examined.

Metabolite concentrations in various brain tissues are confirmed to be different as previous studies have reported. Figure 5.18 demonstrates that in predominately gray matter voxel, the Cho level is similar to that of white matter whereas the NAA and Cr levels are decreased.

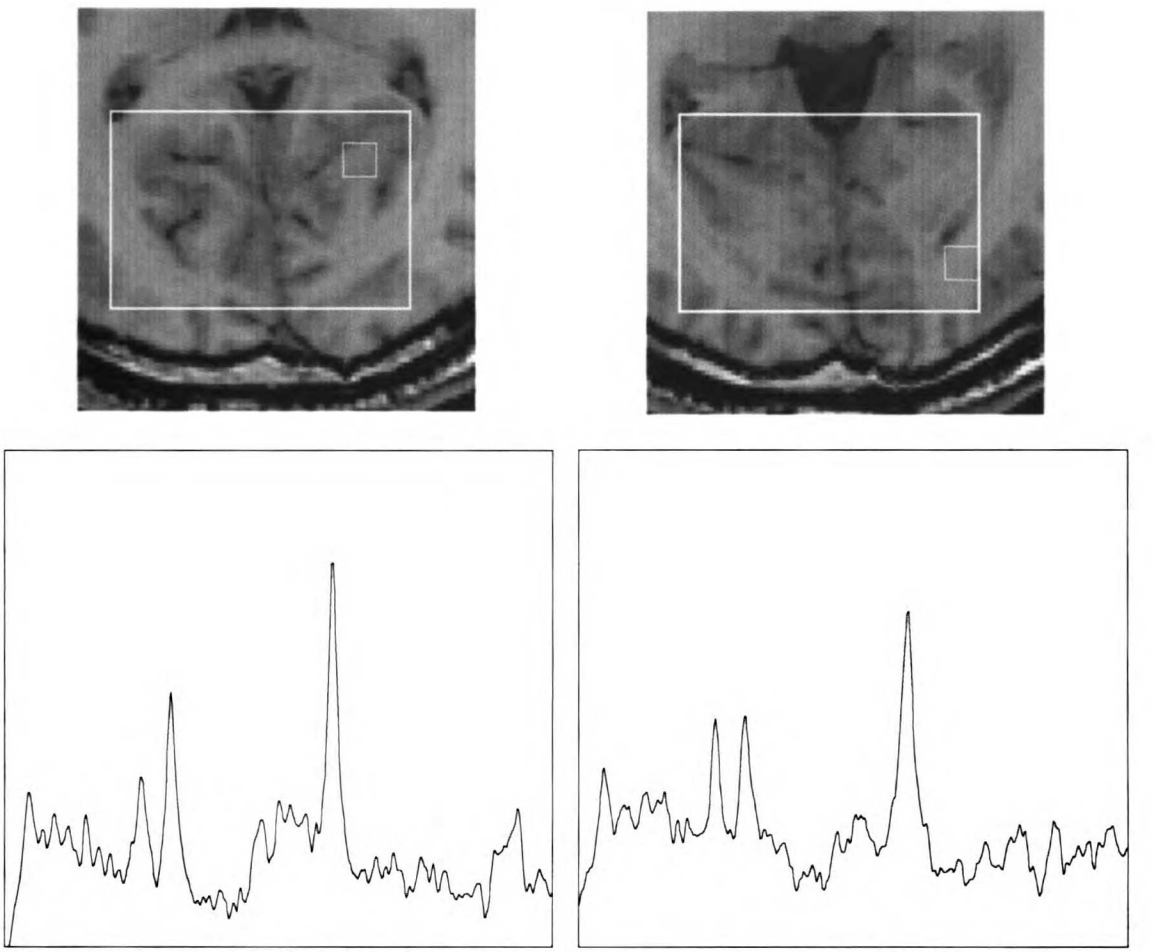

Figure 5.18. Spectral comparison between gray and white matter voxels. Metabolite concentrations are clearly different between gray and white matter voxel. At 0.34cc, predominately gray or white voxel can be obtained as demonstrated above.

Figures 5.19 (a) and (b) demonstrate that with the aide of smaller surface PA such as the NOVA TLA, resolution as small as 4.5mm side voxels (0.09cc) are obtainable. Water suppression can be done using both CHESS and spectral-spatial pulses. A quick SNR comparison of the metabolites is shown in Table 5.2.

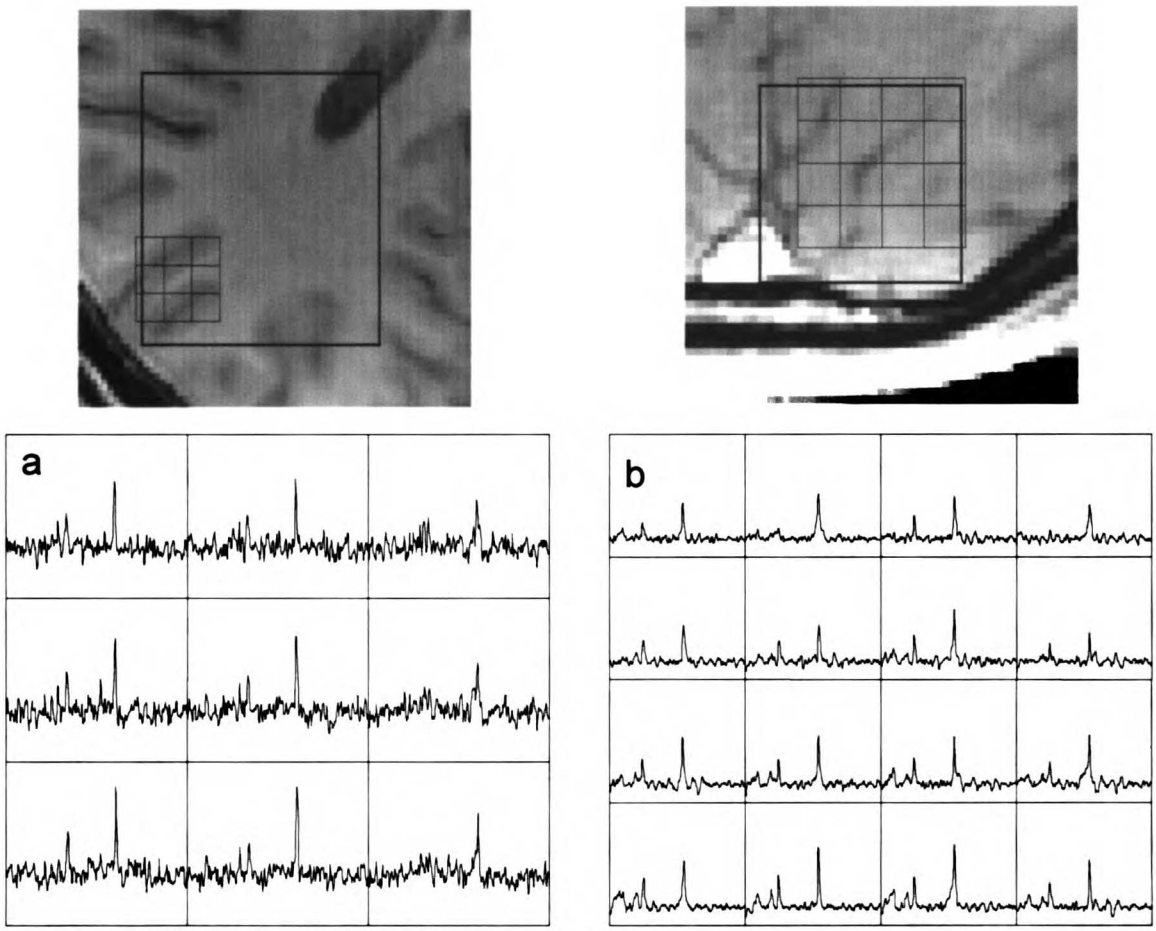

Figure 5.19. Ultra-high res. spectroscopy using spectral-spatial pulses 0.09cc. TE95ms (a) and 0.09cc spectra with CHESS, TE 40ms (b). Both acquired using the NOVA Bi-temporal phased array coil demonstrating the capability of using phased array coils to assess metabolites.

Metabolite	Coil	Peak	SNR Range	SNR Mean
NAA	PA	45	20-45	30
	HEAD	3.9	2.5-3.9	3.1
Cho	PA	14	2-14	7
	HEAD	2.1	0.9-2.1	1.4
Cr	PA	25	6-25	16
	HEAD	2.5	0.8-2.5	1.7

Table 5.2. SNR comparison of metabolite peak heights in PA and Quadrature Head coil.

Discussion

With the increase SNR and sensitivity of 3T scanners, RF power related issues have becoming increasing a problem in obtaining high quality spectroscopic imaging data.

The standard CHESS water suppression and PRESS techniques generally yield inconsistent water suppression and often large lipid contaminations especially when imaging close to the skull. Spectral-spatial pulses have solved these problems at 1.5T, however, at 3T, due to the power concerns, these pulses had to be re-designed and optimized.

The spectral-spatial pulses shown in Figure 5.15 were applied and successfully used to obtain 3D MRSI data with the 8 channel PA coil and body coil RF excitation. Figure 5.16 demonstrates spectra from only a single channel. Due to the coil profile of the 8 channel PA coil, the signal drop-off away from the coil is visible. However, it showed excellent SNR and peak profiles up to 6cm from the coil. At this time, several coil reception profiles correction algorithms are being considered such as using the water as reference, analytical coil profile map, and measured calibration map acquired during the exam.

The 8 channel phased array although does not offer as high SNR as the surface PA coils, but in a clinical setting, its ability to provide greater spatial coverage is important. The capability of imaging more structures with a little sacrifice of sensitivity is preferable due to the fact that often, both normal and abnormal brain tissue need to be imaged in order to make a correct diagnosis for that patient. As Figure 5.18 demonstrates, at 0.34cc, it is possible to detect gray and white matter metabolite level differences.

Another important advance is that elliptical reduced k-space sampling was employed in the MSRI data acquisitions. Due to Fourier properties and the roundedness shape of the human brain, sampling the middle portion of the k-space can save a great deal of imaging time and still yield excellent spectra. [112] All of the data shown in this section were acquired using an elliptical radius of 1.2, which provided a time saving of 50%.

Although 0.34cc MRSI data obtained in the 8 channel PA head coil was possible to distinguish most of gray and white matter, to have purely gray or white matter voxels, entire smaller resolution is needed. The 0.09cc data shown in Figures 5.16a and 5.16b offers unprecedented spatial resolution for in vivo human brain spectroscopic imaging. At this resolution, delineating metabolite concentration between the brain structures such as the gray and white matter can be easily achieved. Occipital metabolite ratios in the gray matter regions were NAA/Cho 3.47 + 1.49, NAA/Cr 1.92 + 0.36, and Cr/Cho 1.79 + 0.55. In white matter regions, the ratios were NAA/Cho 2.70 + 0.90, NAA/Cr 1.99 + 0.70, Cr/Cho 1.40 + 0.34. These ratios agreed with the previous values reported by Noworolski et al. [105]. It has been demonstrated that spectral-spatial pulses provide better water suppression than CHESS [113, 114]. But at 3T, due to the receive-only PA coils and using body coil for excitation, SAR remained an issue during data acquisition. The specially designed low power pulses provided excellent water suppression and remained under the SAR limit within an normal TR of 1.1 seconds.

Although surface PA coils intensity drops off as a function of distance away from the coil, the 7-10 times SNR gain at the cortex was significant and improved detection of

anatomy and metabolite levels of cortex in vivo. This great increase in SNR may also enable more accurate studies of GABA, Glx, mI metabolites, which will provide further insights into the human brain metabolism [67, 115, 116].

5.6 Summary

In this chapter, advanced spectroscopy techniques and a clinical application in assessing neonatal birth asphyxia patient were described. Through more improved hardware (namely phased array coils and specially designed coils) and acquisition methods (namely lactate editing, automated ROI analysis), a full metabolic workup of the injured patients was improved. The metabolic profile of the patient is complementary to the anatomic and diffusion data investigated in this dissertation.

6 Summary and Discussion

This dissertation research project was focused on developing new scanner hardware and software for improving MR data acquisition speed and resolution for anatomic and metabolic brain imaging. The project also included the development of novel image analysis methods for rapid automatic post-processing of MR spectroscopic image data. The overall goal was to provide an accurate assessment of the patient condition through the utilization of the various methods described above.

With the development of high SNR phased arrays, higher image and spectra resolution can be achieved. Although the reception profile of phased array coils intensity drops off as a function of distance away from the coil, the 7-10 times SNR gain at the cortex is significant and provides details of the function and anatomy of cortex in vivo. Spectroscopic data with 0.09cc spatial resolution can be obtained that offers unprecedented spatial resolution for in vivo human brain metabolic imaging. At this resolution, delineating metabolite concentration between the brain structures such as the gray and white matter can be reliably achieved. Now, it is possible to completely isolate the gray and white matter, and determine the differences between them. The development of this technique will allow further investigations of the finer anatomical details and pathology to be studied. In addition to the increased spatial and spectral resolution, the large gain in SNR enables more advanced techniques to measure metabolite levels previously lost in the noise. Shortening of TE together with spectral

editing techniques, metabolites such as GABA, glutamate and glutamine, myo-Inositol can be accurately quantified and used in clinical diagnosis.

In terms of developing new techniques for acquisition on the MR scanner, the investigation of using sequences with less artifacts such as the DTI-SSFSE prove to be useful even with sacrifices in terms of time and some SNR. Traditional clinical diffusion studies using EPI acquisitions demonstrate dramatic distortions on the resultant images due to magnetic susceptibility artifacts and alternating gradient switching. These susceptibility artifacts are especially pronounced in tumor masses and adversely affect the ability to provide accurate DTI parameter maps. SSFSE-DTI studies at 1.5T and 3.0T have demonstrated minimally distorted images and accurate diffusion parameter measurements, and therefore, enable the investigation of the diffusion parameters in the exact extent of the tumor, and may provide possible better assessment and treatment of patients. In the research described above in section 4.3, analysis of the deformation parameters in non-rigid registrations and the brain shape characteristics demonstrate significantly larger distortions in EPI-DTI than SSFSE-DTI in brain tumor patients while the ADC values are comparable in non-distorted regions. In the T2 hyperintense regions, the ADC is significantly higher than normal brain tissue as indicated in previous studies.

In the SSFSE diffusion study of the preterm brainstem to assess maturational changes for these values in premature infants with no evidence of brain injury over the range of 27-40 weeks estimated gestational age, the various regions of the brainstem showed significantly different DTI parameter values. Those patients with white matter injuries

did not show significant diffusion differences in the brainstem regions in the population studied. This study found that the neurons involved sensory pathway (dorsal) demonstrated lower diffusivity than that of motor pathway (ventral neurons), which corresponds to known maturation values. Also, deep gray nuclei, which mature earlier than the rest of the structures, demonstrated lower diffusivity values.

In this dissertation project, SSFSE-DTI was used for diffusion imaging of the brain and cervical regions, other studies are now in progress in utilizing the SSFSE-DTI sequence to study lumbar and thoracic spine, prostate, and liver.

With recent advances in parallel imaging, the SSFSE-DTI sequence was also modified to be compatible to use with phased array with accelerated image acquisition. This allowed more slices to be collected and enabled whole brain acquisitions within the limited time in a clinical setting. Furthermore, with the reduced echo train length of the acquisition, T2 decay effect is much less represented than the standard sequence. This yielded sharper contrast for the edges as the higher order of k-space is acquired later, which now have ample SNR and less T2 blurring. These improvements are necessary for the clinical application of SSFSE and allow for minimally distorted and quantitatively accurate measurements of water diffusion parameters.

Besides developments in hardware and software for image acquisition to improve image quality and usability, the other possible advancement area would be post-processing. In this work, an automated processing technique was developed to use ROI based analysis

with MR spectroscopy specifically applied to patients with suspected brain injury, which allowed for large quantity of data processing in a small amount of time.

This processing technique was applied to study patients with neonatal encephalopathy. Increased brain lactate (LAC) levels and decreased N-acetylaspartate (NAA) levels, were measured by proton MR spectroscopy in specific brain regions, are associated with adverse neurodevelopmental outcome. Lactate-edited 3D MRSI now allows the assessment of these metabolite levels throughout the newborn brain. The new automated processing methods were able to rapidly analyze the 1024 spectral arrays acquired in neonatal MRSI in order to better quantify the presence and extent of abnormal metabolite levels. These methods were investigated in a preliminary study of term neonatal encephalopathy. The rapid post-processing methods allowed the analysis of all spectra in <0.5 hours and provided metabolite ratios for specific anatomic ROIs. In this study, LAC/NAA and LAC/choline (LAC/CHO) were increased and NAA/CHO decreased in widespread regions, in neonates with fatal outcome relative to those with normal neurodevelopmental outcome at 1 year of age.

In this dissertation work, various aspects of MR imaging were considered—acquisition hardware and software and post-processing methods. As mentioned previously, considerations have to be made to combine all these aspects when performing a comprehensive exam of the subject to yield the most accurate results.

7 References

1. Bloch F., *Nuclear Induction.* Physical Review, 1946. **70**(7): p. 460-474.
2. Hahn E.L., *Spin Echoes.* Physical Review, 1950. **80**(4): p. 580-594.
3. Carr H.Y. and Purcell E.M., *Effects of Diffusion on Free Precession in Nuclear Magnetic Resonance Experiments.* Physical Review, 1954. **94**(3): p. 630-638.
4. Damadian R., *Tumor Detection by Nuclear Magnetic Resonance.* Science, 1971. **171**(3976): p. 1151-&.
5. Lauterbur P.C., *Image Formation by Induced Local Interactions - Examples Employing Nuclear Magnetic-Resonance.* Nature, 1973. **242**(5394): p. 190-191.
6. Nelson S.J., *Analysis of volume MRI and MR spectroscopic imaging data for the evaluation of patients with brain tumors.* Magn Reson Med, 2001. **46**(2): p. 228-39.
7. Shung K.K., Smith M.B., and Tsui B.M.W., *Fundamentals of Nuclear Magnetic Resonance*, in *Principles of medical imaging.* 1992, Academic Press: San Diego. p. 216.
8. Cho Z.-H., Jones J., and Singh M., *Physical Bases of NMR*, in *Foundations of Medical Imaging.* 1993, John Wiley & Sons, Inc: Irvine. p. 249.
9. Nishimura D., *Principles of Magnetic Resonance Imaging.* 1996.
10. Moyher S.E., Vigneron D.B., and Nelson S.J., *Surface coil MR imaging of the human brain with an analytic reception profile correction.* J Magn Reson Imaging, 1995. **5**(2): p. 139-44.
11. Leifer M.C., *Theory of the quadrature elliptic birdcage coil.* Magn Reson Med, 1997. **38**(5): p. 726-32.
12. Welker K.M., Tsuruda J.S., Hadley J.R., and Hayes C.E., *Radio-frequency coil selection for MR imaging of the brain and skull base.* Radiology, 2001. **221**(1): p. 11-25.
13. Shung K.K., Smith M.B., and Tsui B.M.W., *Imaging Methods*, in *Principles of medical imaging.* 1992, Academic Press: San Diego. p. 242.
14. Wald L.L., Moyher S.E., Day M.R., Nelson S.J., and Vigneron D.B., *Proton spectroscopic imaging of the human brain using phased array detectors.* Magn Reson Med, 1995. **34**(3): p. 440-5.
15. Blaimer M., Breuer F., Mueller M., Heidemann R.M., Griswold M.A., and Jakob P.M., *SMASH, SENSE, PILS, GRAPPA: how to choose the optimal method.* Top Magn Reson Imaging, 2004. **15**(4): p. 223-36.
16. Paschal C.B. and Morris H.D., *K-space in the clinic.* J Magn Reson Imaging, 2004. **19**(2): p. 145-59.
17. Einstein A., *Investigations on the theory of the Brownian movement.* 1926, New York: Dover.
18. Tanner J.E. and Stejskal E.O., *Restricted Self-Diffusion of Protons in Colloidal Systems by the Pulsed-Gradient, Spin-Echo Method.* J Chem Phys, 1968. **49**: p. 1968-1977.
19. Mattiello J., Basser P.J., and Lebihan D., *Analytical Expressions for the B-Matrix in Nmr Diffusion Imaging and Spectroscopy.* Journal of Magnetic Resonance Series A, 1994. **108**(2): p. 131-141.

20. Cooper R.L., Chang D.B., Young A.C., Martin C.J., and Ancker-Johnson D., *Restricted diffusion in biophysical systems. Experiment.* Biophys J, 1974. **14**(3): p. 161-77.
21. Le Bihan D. and Basser P.J., *Molecular Diffusion and NMR*, in *Diffusion and Perfusion Magnetic Resonance Imaging: Applications to Functional MRI*, D. Le Bihan, Editor. 1995, Raven Press, Ltd. p. 12.
22. Pipe J.G., Farthing V.G., and Forbes K.P., *Multishot diffusion-weighted FSE using PROPELLER MRI.* Magn Reson Med, 2002. **47**(1): p. 42-52.
23. Forbes K.P., Pipe J.G., Bird C.R., and Heiserman J.E., *PROPELLER MRI: clinical testing of a novel technique for quantification and compensation of head motion.* J Magn Reson Imaging, 2001. **14**(3): p. 215-22.
24. Hori M., Ichikawa T., Sou H., Tsukamoto T., Kitamura T., Okubo T., Araki T., Amemiya Y., Okamoto E., and Obara M., *[Improving diffusion-weighted imaging of liver with SENSE technique: a preliminary study].* Nippon Igaku Hoshasen Gakkai Zasshi, 2003. **63**(4): p. 177-9.
25. Bammer R., Auer M., Keeling S.L., Augustin M., Stables L.A., Prokesch R.W., Stollberger R., Moseley M.E., and Fazekas F., *Diffusion tensor imaging using single-shot SENSE-EPI.* Magn Reson Med, 2002. **48**(1): p. 128-36.
26. Sodickson D.K. and McKenzie C.A., *A generalized approach to parallel magnetic resonance imaging.* Medical Physics, 2001. **28**(8): p. 1629-1643.
27. Sodickson D.K. and Manning W.J., *Simultaneous acquisition of spatial harmonics (SMASH): Fast imaging with radiofrequency coil arrays.* Magnetic Resonance in Medicine, 1997. **38**(4): p. 591-603.
28. Pruessmann K.P., Weiger M., Scheidegger M.B., and Boesiger P., *SENSE: Sensitivity encoding for fast MRI.* Magnetic Resonance in Medicine, 1999. **42**(5): p. 952-962.
29. Xu D., Henry R.G., Mukherjee P., Carvajal L., Miller S.P., Barkovich A.J., and Vigneron D.B., *Single-shot fast spin-echo diffusion tensor imaging of the brain and spine with head and phased array coils at 1.5 T and 3.0 T.* Magn Reson Imaging, 2004. **22**(6): p. 751-9.
30. Rueckert D., Sonoda L.I., Hayes C., Hill D.L., Leach M.O., and Hawkes D.J., *Nonrigid registration using free-form deformations: application to breast MR images.* IEEE Trans Med Imaging, 1999. **18**(8): p. 712-21.
31. Puzicha J., Hofmann T., and Buhmann J., *Non-parametric similarity measures for unsupervised texture segmentation and image retrieval.* Proceedings of IEEE Conference on Computer Vision and Pattern Recognition, 1997: p. 267-72.
32. Moseley M., *Diffusion tensor imaging and aging - a review.* NMR Biomed, 2002. **15**(7-8): p. 553-60.
33. Sotak C.H., *The role of diffusion tensor imaging in the evaluation of ischemic brain injury - a review.* NMR Biomed, 2002. **15**(7-8): p. 561-9.
34. Horsfield M.A. and Jones D.K., *Applications of diffusion-weighted and diffusion tensor MRI to white matter diseases - a review.* NMR Biomed, 2002. **15**(7-8): p. 570-7.
35. Guo A.C., MacFall J.R., and Provenzale J.M., *Multiple sclerosis: diffusion tensor MR imaging for evaluation of normal-appearing white matter.* Radiology, 2002. **222**(3): p. 729-36.

36. Fujikawa A., Tsuchiya K., Koppera P., Aoki C., and Hachiya J., *Case report: spinal cord infarction demonstrated on diffusion-weighted MR imaging with a single-shot fast spin-echo sequence.* J Comput Assist Tomogr, 2003. **27**(3): p. 415-9.
37. Tsuchiya K., Katase S., Fujikawa A., Hachiya J., Kanazawa H., and Yodo K., *Diffusion-weighted MRI of the cervical spinal cord using a single-shot fast spin-echo technique: findings in normal subjects and in myelomalacia.* Neuroradiology, 2003. **45**(2): p. 90-4.
38. Bastin M.E. and Le Roux P., *On the application of a non-CPMG single-shot fast spin-echo sequence to diffusion tensor MRI of the human brain.* Magn Reson Med, 2002. **48**(1): p. 6-14.
39. Partridge S.C., McKinnon G.C., Henry R.G., and Hylton N.M., *Menstrual cycle variation of apparent diffusion coefficients measured in the normal breast using MRI.* J Magn Reson Imaging, 2001. **14**(4): p. 433-8.
40. Alsop D.C., *Phase insensitive preparation of single-shot RARE: application to diffusion imaging in humans.* Magn Reson Med, 1997. **38**(4): p. 527-33.
41. Basser P.J. and Pierpaoli C., *Microstructural and physiological features of tissues elucidated by quantitative-diffusion-tensor MRI.* J Magn Reson B, 1996. **111**(3): p. 209-19.
42. Dumoulin C.L., Rohling K.W., and Piel J.E., *Magnetic resonance imaging compatible neonate incubator.* Magnetic Resonance Engineering, 2002. **15**: p. 117-28.
43. Henry R.G., Fischbein N.J., Dillon W.P., Vigneron D.B., and Nelson S.J., *High-sensitivity coil array for head and neck imaging: technical note.* AJNR Am J Neuroradiol, 2001. **22**(10): p. 1881-6.
44. Pajevic S. and Pierpaoli C., *Color schemes to represent the orientation of anisotropic tissues from diffusion tensor data: application to white matter fiber tract mapping in the human brain.* Magn Reson Med, 1999. **42**(3): p. 526-40.
45. Thomsen C., Henriksen O., and Ring P., *In vivo measurement of water self diffusion in the human brain by magnetic resonance imaging.* Acta Radiol, 1987. **28**(3): p. 353-61.
46. Le Bihan D., Breton E., Lallemand D., Aubin M.L., Vignaud J., and Laval-Jeantet M., *Separation of diffusion and perfusion in intravoxel incoherent motion MR imaging.* Radiology, 1988. **168**(2): p. 497-505.
47. Hajnal J.V., Doran M., Hall A.S., Collins A.G., Oatridge A., Pennock J.M., Young I.R., and Bydder G.M., *MR imaging of anisotropically restricted diffusion of water in the nervous system: technical, anatomic, and pathologic considerations.* J Comput Assist Tomogr, 1991. **15**(1): p. 1-18.
48. Neil J., Miller J., Mukherjee P., and Huppi P.S., *Diffusion tensor imaging of normal and injured developing human brain - a technical review.* NMR Biomed, 2002. **15**(7-8): p. 543-52.
49. Bammer R., Fazekas F., Augustin M., Simbrunner J., Strasser-Fuchs S., Seifert T., Stollberger R., and Hartung H.P., *Diffusion-weighted MR imaging of the spinal cord.* AJNR Am J Neuroradiol, 2000. **21**(3): p. 587-91.

50. Butts K., Pauly J., de Crespigny A., and Moseley M., *Isotropic diffusion-weighted and spiral-navigated interleaved EPI for routine imaging of acute stroke.* Magn Reson Med, 1997. **38**(5): p. 741-9.
51. Gudbjartsson H., Maier S.E., Mulkern R.V., Morocz I.A., Patz S., and Jolesz F.A., *Line scan diffusion imaging.* Magn Reson Med, 1996. **36**(4): p. 509-19.
52. Bastin M.E., Armitage P.A., and Marshall I., *A theoretical study of the effect of experimental noise on the measurement of anisotropy in diffusion imaging.* Magn Reson Imaging, 1998. **16**(7): p. 773-85.
53. Mukherjee P., Miller J.H., Shimony J.S., Philip J.V., Nehra D., Snyder A.Z., Conturo T.E., Neil J.J., and McKinstry R.C., *Diffusion-tensor MR imaging of gray and white matter development during normal human brain maturation.* AJNR Am J Neuroradiol, 2002. **23**(9): p. 1445-56.
54. Bammer R., Augustin M., and Simbrunner J., *Interleaved EPI and turbo SE DWI of the human cervical spinal cord.* Proceedings of Eighth Annual Meeting of International Society of Magnetic Resonance in Medicine, 2000. **vol1**: p. P477.
55. Grant P.E., Vigneron D.B., and Barkovich A.J., *High-resolution imaging of the brain.* Magn Reson Imaging Clin N Am, 1998. **6**(1): p. 139-54.
56. Holder C.A., Muthupillai R., Mukundan S., Jr., Eastwood J.D., and Hudgins P.A., *Diffusion-weighted MR imaging of the normal human spinal cord in vivo.* AJNR Am J Neuroradiol, 2000. **21**(10): p. 1799-806.
57. Clark C.A., Barker G.J., and Tofts P.S., *Magnetic resonance diffusion imaging of the human cervical spinal cord in vivo.* Magn Reson Med, 1999. **41**(6): p. 1269-73.
58. Barker G.J., *Diffusion-weighted imaging of the spinal cord and optic nerve.* J Neurol Sci, 2001. **186 Suppl 1**: p. S45-9.
59. Hsu E.W. and Setton L.A., *Diffusion tensor microscopy of the intervertebral disc anulus fibrosus.* Magn Reson Med, 1999. **41**(5): p. 992-9.
60. Mamata H., Mamata Y., Westin C.F., Shenton M.E., Kikinis R., Jolesz F.A., and Maier S.E., *High-resolution line scan diffusion tensor MR imaging of white matter fiber tract anatomy.* AJNR Am J Neuroradiol, 2002. **23**(1): p. 67-75.
61. Wittsack H.J., Ritzl A., Fink G.R., Wenserski F., Siebler M., Seitz R.J., Modder U., and Freund H.J., *MR Imaging in acute stroke: Diffusion-weighted and perfusion imaging parameters for predicting infarct size.* Radiology, 2002. **222**(2): p. 397-403.
62. Helenius J., Soinne L., Salonen O., Kaste M., and Tatlisumak T., *Leukoaraiosis, ischemic stroke, and normal white matter on diffusion-weighted MRI.* Stroke, 2002. **33**(1): p. 45-50.
63. Pierpaoli C., Jezzard P., Basser P.J., Barnett A., and DiChiro G., *Diffusion tensor MR imaging of the human brain.* Radiology, 1996. **201**(3): p. 637-648.
64. Miller S.P., Vigneron D.B., Henry R.G., Bohland M.A., Ceppi-Cozzio C., Hoffman C., Newton N., Partridge J.C., Ferriero D.M., and Barkovich A.J., *Serial quantitative diffusion tensor MRI of the premature brain: Development in newborns with and without injury.* Journal of Magnetic Resonance Imaging, 2002. **16**(6): p. 621-632.

65. Woods R.P., Grafton S.T., Holmes C.J., Cherry S.R., and Mazziotta J.C., *Automated image registration: I. General methods and intrasubject, intramodality validation.* J Comput Assist Tomogr, 1998. **22**(1): p. 139-52.
66. Nagata M., Maeda M., Tsukahara H., Maier S.E., and Takeda K., *Brain stem hypertensive encephalopathy evaluated by line scan diffusion-weighted imaging.* AJNR Am J Neuroradiol, 2004. **25**(5): p. 803-6.
67. Barkovich A.J., *Normal Development*, in *Pediatric neuroimaging*. 2000, Lippincott Williams & Wilkins: Philadelphia. p. 13-69.
68. Zhang L., Thomas K.M., Davidson M.C., Casey B.J., Heier L.A., and Ulug A.M., *MR Quantitation of Volume and Diffusion Changes in the Developing Brain.* AJNR Am J Neuroradiol, 2005. **26**(1): p. 45-9.
69. Burt A.M., *Organization and Development of the Nervous System*, in *Textbook of Neuroanatomy*. 1993, W. B. Saunders Company: Philadelphia. p. 15.
70. Salibi N. and Brown M., *Time-Independent Interactions*, in *Concepts of Magnetic Resonance Spectroscopy*. 1998, John Wiley & Sons, Inc.: New York. p. 22.
71. Ross B. and Michaelis T., *Clinical-Applications of Magnetic-Resonance Spectroscopy.* Magnetic Resonance Quarterly, 1994. **10**(4): p. 191-247.
72. Howe F.A., Barton S.J., Cudlip S.A., Stubbs M., Saunders D.E., Murphy M., Wilkins P., Opstad K.S., Doyle V.L., McLean M.A., et al., *Metabolic profiles of human brain tumors using quantitative in vivo H-1 magnetic resonance spectroscopy.* Magnetic Resonance in Medicine, 2003. **49**(2): p. 223-232.
73. Murphy M., Loosemore A., Clifton A.G., Howe F.A., Tate A.R., Cudlip S.A., Wilkins P.R., Griffiths J.R., and Bell B.A., *The contribution of proton magnetic resonance spectroscopy ((HMRS)-H-1) to clinical brain tumour diagnosis.* British Journal of Neurosurgery, 2002. **16**(4): p. 329-334.
74. Kugel H., Heindel W., Ernestus R.I., Bunke J., Dumesnil R., and Friedmann G., *Human Brain-Tumors - Spectral Patterns Detected with Localized H-1 Mr Spectroscopy.* Radiology, 1992. **183**(3): p. 701-709.
75. Herminghaus S., Pilatus U., Moller-Hartmann W., Raab P., Lanfermann H., Schlote W., and Zanella F.E., *Increased choline levels coincide with enhanced proliferative activity of human neuroepithelial brain tumors.* Nmr in Biomedicine, 2002. **15**(6): p. 385-392.
76. Saks V.A., Rosenshtraukh L.V., Smirnov V.N., and Chazov E.I., *Role of Creatine-Phosphokinase in Cellular Function and Metabolism.* Canadian Journal of Physiology and Pharmacology, 1978. **56**(5): p. 691-706.
77. Baslow M.H., *Evidence supporting a role for N-acetyl-L-aspartate as a molecular water pump in myelinated neurons in the central nervous system. An analytical review.* Neurochem Int, 2002. **40**(4): p. 295-300.
78. Chakraborty G., Mekala P., Yahya D., Wu G., and Ledeen R.W., *Intraneuronal N-acetylaspartate supplies acetyl groups for myelin lipid synthesis: evidence for myelin-associated aspartoacylase.* J Neurochem, 2001. **78**(4): p. 736-45.
79. Stubbs M., Veech R.L., and Griffiths J.R., *Tumor Metabolism - the Lessons of Magnetic-Resonance Spectroscopy.* Advances in Enzyme Regulation, Vol 35, 1995. **35**: p. 101-115.

80. Auer D.P., Gossl C., Schirmer T., and Czisch M., *Improved analysis of H-1-MR spectra in the presence of mobile lipids.* Magnetic Resonance in Medicine, 2001. **46**(3): p. 615-618.
81. Star-Lack J., Nelson S.J., Kurhanewicz J., Huang L.R., and Vigneron D.B., *Improved water and lipid suppression for 3D PRESS CSI using RF band selective inversion with gradient dephasing (BASING).* Magn Reson Med, 1997. **38**(2): p. 311-21.
82. Bottomley P.A., *Spatial localization in NMR spectroscopy in vivo.* Ann N Y Acad Sci, 1987. **508**: p. 333-48.
83. Ordidge R.J., Mansfield P., Lohman J.A., and Prime S.B., *Volume selection using gradients and selective pulses.* Ann N Y Acad Sci, 1987. **508**: p. 376-85.
84. Ordidge R.J., Bowley R.M., and McHale G., *A general approach to selection of multiple cubic volume elements using the ISIS technique.* Magn Reson Med, 1988. **8**(3): p. 323-31.
85. Frahm J., Bruhn H., Gyngell M.L., Merboldt K.D., Hanicke W., and Sauter R., *Localized high-resolution proton NMR spectroscopy using stimulated echoes: initial applications to human brain in vivo.* Magn Reson Med, 1989. **9**(1): p. 79-93.
86. Riddle W.R., Gibbs S.J., and Willcott M.R., *Dissecting and implementing STEAM spectroscopy.* Magn Reson Med, 1993. **29**(3): p. 378-80.
87. Moonen C.T., von Kienlin M., van Zijl P.C., Cohen J., Gillen J., Daly P., and Wolf G., *Comparison of single-shot localization methods (STEAM and PRESS) for in vivo proton NMR spectroscopy.* NMR Biomed, 1989. **2**(5-6): p. 201-8.
88. Yongbi N.M., Payne G.S., Collins D.J., and Leach M.O., *Quantification of signal selection efficiency, extra volume suppression and contamination for ISIS, STEAM and PRESS localized 1H NMR spectroscopy using an EEC localization test object.* Phys Med Biol, 1995. **40**(7): p. 1293-303.
89. Barkovich A.J., Westmark K., Partridge C., Sola A., and Ferriero D.M., *Perinatal asphyxia: MR findings in the first 10 days.* AJNR Am J Neuroradiol, 1995. **16**(3): p. 427-38.
90. Barkovich A.J. and Hallam D., *Neuroimaging in perinatal hypoxic-ischemic injury.* Mental Retardation and Developmental Disabilities Research Reviews, 1997. **3**(1): p. 28-41.
91. Barkovich A.J., Westmark K.D., Bedi H.S., Partridge J.C., Ferriero D.M., and Vigneron D.B., *Proton spectroscopy and diffusion imaging on the first day of life after perinatal asphyxia: preliminary report.* AJNR Am J Neuroradiol, 2001. **22**(9): p. 1786-94.
92. Vigneron D.B., Miller S.P., Henry R.G., Ferriero D.M., Bohland M.A., Lu Y., Newton N., Glenn O.A., Chun T., Partridge J.C., et al., *3D MRSI and Diffusion Tensor Imaging of the Neonatal Brain following Birth Asphyxia.* Proceedings of Tenth Annual Meeting of International Society of Magnetic Resonance in Medicine, 2002: p. 800.
93. Hajnal B.L., Sahebkar-Moghaddam F., Barnwell A.J., Barkovich A.J., and Ferriero D.M., *Early prediction of neurologic outcome after perinatal depression.* Pediatr Neurol, 1999. **21**(5): p. 788-93.

94. Luyten P.R., Marien A.J., and den Hollander J.A., *Acquisition and quantitation in proton spectroscopy.* NMR Biomed, 1991. **4**(2): p. 64-9.
95. Tran T.K., Vigneron D.B., Sailasuta N., Tropp J., Le Roux P., Kurhanewicz J., Nelson S., and Hurd R., *Very selective suppression pulses for clinical MRSI studies of brain and prostate cancer.* Magn Reson Med, 2000. **43**(1): p. 23-33.
96. Nelson S.J., *Multivoxel magnetic resonance spectroscopy of brain tumors.* Mol Cancer Ther, 2003. **2**(5): p. 497-507.
97. Moore G.J., *Proton magnetic resonance spectroscopy in pediatric neuroradiology.* Pediatr Radiol, 1998. **28**(11): p. 805-14.
98. Zimmerman R.A. and Wang Z.J., *The value of proton MR spectroscopy in pediatric metabolic brain disease.* AJNR Am J Neuroradiol, 1997. **18**(10): p. 1872-9.
99. Scarabino T., Popolizio T., Bertolino A., and Salvolini U., *Proton magnetic resonance spectroscopy of the brain in pediatric patients.* Eur J Radiol, 1999. **30**(2): p. 142-53.
100. Vigneron D.B., Barkovich A.J., Noworolski S.M., von dem Bussche M., Henry R.G., Lu Y., Partridge J.C., Gregory G., and Ferriero D.M., *Three-dimensional proton MR spectroscopic imaging of premature and term neonates.* AJNR Am J Neuroradiol, 2001. **22**(7): p. 1424-33.
101. Fan G., Wu Z., Chen L., Guo Q., Ye B., and Mao J., *Hypoxia-ischemic encephalopathy in full-term neonate: correlation proton MR spectroscopy with MR imaging.* Eur J Radiol, 2003. **45**(2): p. 91-8.
102. Zarifi M.K., Astrakas L.G., Poussaint T.Y., Plessis Ad A., Zurakowski D., and Tzika A.A., *Prediction of adverse outcome with cerebral lactate level and apparent diffusion coefficient in infants with perinatal asphyxia.* Radiology, 2002. **225**(3): p. 859-70.
103. Shah S., Tracy M., and Smyth J., *Postnatal lactate as an early predictor of short-term outcome after intrapartum asphyxia.* J Perinatol, 2004. **24**(1): p. 16-20.
104. Miller S.P., Weiss J., Barnwell A., Ferriero D.M., Latal-Hajnal B., Ferrer-Rogers A., Newton N., Partridge J.C., Glidden D.V., Vigneron D.B., et al., *Seizure-associated brain injury in term newborns with perinatal asphyxia.* Neurology, 2002. **58**(4): p. 542-8.
105. Noworolski S.M., Nelson S.J., Henry R.G., Day M.R., Wald L.L., Star-Lack J., and Vigneron D.B., *High spatial resolution 1H-MRSI and segmented MRI of cortical gray matter and subcortical white matter in three regions of the human brain.* Magn Reson Med, 1999. **41**(1): p. 21-9.
106. Florian C.L., Williams S.R., Bhakoo K.K., and Noble M.D., *Regional and developmental variations in metabolite concentration in the rat brain and eye: a study using 1H NMR spectroscopy and high performance liquid chromatography.* Neurochem Res, 1996. **21**(9): p. 1065-74.
107. Koller K.J., Zaczek R., and Coyle J.T., *N-acetyl-aspartyl-glutamate: regional levels in rat brain and the effects of brain lesions as determined by a new HPLC method.* J Neurochem, 1984. **43**(4): p. 1136-42.
108. Urenjak J., Williams S.R., Gadian D.G., and Noble M., *Proton nuclear magnetic resonance spectroscopy unambiguously identifies different neural cell types.* J Neurosci, 1993. **13**(3): p. 981-9.

109. Schricker A.A., Pauly J.M., Kurhanewicz J., Swanson M.G., and Vigneron D.B., *Dualband spectral-spatial RF pulses for prostate MR spectroscopic imaging.* Magn Reson Med, 2001. **46**(6): p. 1079-87.
110. Srinivasan R., Vigneron D., Sailasuta N., Hurd R., and Nelson S., *A comparative study of myo-inositol quantification using LCmodel at 1.5 T and 3.0 T with 3 D H-1 proton spectroscopic imaging of the human brain.* Magnetic Resonance Imaging, 2004. **22**(4): p. 523-528.
111. Hurd R., Sailasuta N., Srinivasan R., Vigneron D.B., Pelletier D., and Nelson S.J., *Measurement of brain glutamate using TE-averaged PRESS at 3T.* Magnetic Resonance in Medicine, 2004. **51**(3): p. 435-440.
112. Maudsley A.A., Matson G.B., Hugg J.W., and Weiner M.W., *Reduced phase encoding in spectroscopic imaging.* Magn Reson Med, 1994. **31**(6): p. 645-51.
113. Males R.G., Vigneron D.B., Star-Lack J., Falbo S.C., Nelson S.J., Hricak H., and Kurhanewicz J., *Clinical application of BASING and spectral/spatial water and lipid suppression pulses for prostate cancer staging and localization by in vivo 3D 1H magnetic resonance spectroscopic imaging.* Magn Reson Med, 2000. **43**(1): p. 17-22.
114. Cunningham C.H., Vigneron D.B., Chen A.P., Xu D., Hurd R.E., Sailasuta N., and Pauly J.M., *Design of symmetric-sweep spectral-spatial RF pulses for spectral editing.* Magn Reson Med, 2004. **52**(1): p. 147-53.
115. Chang L., Cloak C.C., and Ernst T., *Magnetic resonance spectroscopy studies of GABA in neuropsychiatric disorders.* J Clin Psychiatry, 2003. **64 Suppl 3**: p. 7-14.
116. Ure J.A. and Perassolo M., *Update on the pathophysiology of the epilepsies.* J Neurol Sci, 2000. **177**(1): p. 1-17.